

12-1-2016

## Synthesis and Analysis of Carbon-transition Metal Oxide Composites

Binod Manandhar  
*University of Wisconsin-Milwaukee*

Follow this and additional works at: <https://dc.uwm.edu/etd>



Part of the [Condensed Matter Physics Commons](#)

---

### Recommended Citation

Manandhar, Binod, "Synthesis and Analysis of Carbon-transition Metal Oxide Composites" (2016). *Theses and Dissertations*. 1388.

<https://dc.uwm.edu/etd/1388>

This Dissertation is brought to you for free and open access by UWM Digital Commons. It has been accepted for inclusion in Theses and Dissertations by an authorized administrator of UWM Digital Commons. For more information, please contact [open-access@uwm.edu](mailto:open-access@uwm.edu).

SYNTHESIS AND ANALYSIS OF CARBON-TRANSITION METAL OXIDE COMPOSITES

by

Binod Manandhar

A Dissertation Submitted in

Partial Fulfillment of the

Requirements for the Degree of

Doctor of Philosophy

in Physics

at

The University of Wisconsin-Milwaukee

December 2016

## ABSTRACT

### SYNTHESIS AND ANALYSIS OF CARBON-TRANSITION METAL OXIDE COMPOSITES

by

Binod Manandhar

The University of Wisconsin-Milwaukee, 2016  
Under the Supervision of Professor Carol J. Hirschmugl

Graphene, a two-dimensional honeycomb structure of carbon due to its high electrical and thermal conductivity, and high specific surface area, is an excellent candidate for nano-electronics and energy storage. However, it is very difficult and expensive to produce a single layered graphene by the traditional method of mechanical exfoliation of highly oriented pyrolytic graphite (HOPG). It is mainly manufactured by chemical vapor deposition (CVD) or more economically by chemical exfoliation of graphite by Hummer's modified method. But there is a major disadvantage in using the chemical exfoliation, instead of forming single layer of pure graphene, a non-stoichiometric and insulating graphene oxide (GO) is formed. GO further needs to be reduced into graphene by either chemical or thermal method. In our work, we have synthesized and evaluated several compositions of transition metal oxides and carbon based materials. The structure and composition of materials are determined from diffraction and absorption experimental results. The diffraction techniques applied for characterization of carbon transitional metal oxides nanocomposites are selected area electron diffraction and powder x-ray diffraction. Absorption experiments used during experiments are Infrared absorption

spectroscopy, UV-Vis absorption spectroscopy and X-ray absorption spectroscopy (including X-ray absorption near edge structure and Extended X-ray absorption fine structure).

## TABLE OF CONTENTS

Chapter 1 Background and Introduction.....	1
1.1 Organization of the Dissertation .....	1
1.2 Crystalline Allotropic forms of carbon .....	1
1.2.1 Diamond.....	2
1.2.2 Graphite.....	3
1.2.3 Graphene .....	3
1.3 Graphene oxide (GO).....	8
1.4 Graphene monoxide .....	12
1.4.1 Structure.....	12
1.4.2 Future applications:.....	13
1.5 Molybdenum and its oxides .....	14
1.5.1 Molybdenum.....	14
1.5.2 Molybdenum(VI) oxide .....	15

1.5.3	Molybdenum(IV) oxide .....	19
1.6	Lithium Ion Batteries (LIBs):.....	20
1.7	Objective of Dissertation:.....	26
Chapter 2 Methods and instrumentations .....		28
2.1	Crystallography .....	28
2.2	X-ray diffraction.....	32
2.2.1	Introduction.....	32
2.2.2	Experimental setup: .....	35
2.3	Electron Microscopy .....	37
2.3.1	Introduction.....	37
2.3.2	Diffraction mode:.....	40
2.3.3	Image mode:.....	41
2.3.4	Energy-dispersive x-ray spectroscopy (EDX): .....	42
2.4	Infrared Spectroscopy .....	45
2.4.1	Introduction.....	45

2.4.2	Sources:.....	48
2.4.3	Detectors: .....	48
2.5	X-ray Absorption Spectroscopy(XAS) .....	50
2.5.1	Principles of XAS: .....	50
2.5.2	Theory for EXAFS:.....	54
2.5.3	Experimental setup: .....	57
2.6	UV-Vis Spectroscopy.....	63
2.6.1	Introduction.....	63
2.6.2	UV vis band structure: .....	68
2.6.3	Experimental procedure for UV-vis measurement of Mo blue solution: .....	69
2.6.4	Application of UV-vis spectroscopy:.....	70
Chapter 3 Characterization of GO used for experiments:.....		71
3.1	Introduction .....	71
3.2	Result and Discussion: .....	72
3.3	Conclusion:.....	75

Chapter 4 Characterization of Molybdenum blue solution:.....	76
4.1 Introduction .....	76
4.2 Preparation of Mo blue solution:.....	77
4.3 Experimental method: .....	77
4.4 Results and discussions:.....	78
4.4.1 IR measurement: .....	79
4.4.2 UV-Vis measurement: .....	79
4.4.3 XANES: .....	80
4.5 Conclusion:.....	83
Chapter 5 Forming graphene and graphene monoxide from amorphous lacey carbon .....	84
5.1 Introduction .....	84
5.2 Sample preparation.....	85
5.3 Results .....	87
5.4 Discussion: .....	93
5.5 Conclusion:.....	95



Chapter 6 : Catalytic synthesis and structural characterization of Graphene Monoxide.....	97
6.1 Introduction:.....	97
6.2 Experimental methods.....	99
6.2.1 Molybdenum blue solution preparation.....	99
6.2.2 Nanogram scale: Reduction of GO/Mo blue deposited on Ni TEM grid:.....	99
6.2.3 Milligram scale: Reduction of GO and Mo blue solution.....	100
6.3 Results and discussions:.....	106
6.3.1 TEM measurement:.....	106
6.3.2 XRD Measurement:.....	107
XAS measurement:.....	108
6.3.3 IR measurement:.....	109
6.3.4 Conclusion:.....	109
6.3.5 Acknowledgements.....	110
Chapter 7 : Formation of graphene monoxide by electron bombardment and <i>in situ</i> heating mixture of graphene oxide and chromium trioxide.....	111
7.1 Introduction.....	111

7.2	Experimental: .....	112
7.3	Results: .....	112
7.4	Discussion: .....	114
7.5	Conclusion:.....	115
Chapter 8 : Synthesis of Molybdenum dioxide/reduced GO nano-composite .....		116
8.1	Introduction: .....	116
8.2	Experimental methods.....	118
8.2.1	Nanogram scale: Reduction of GO deposited on Mo TEM grid: .....	118
8.2.2	Milligram scale: Reduction of GO and Mo blue solution.....	119
8.3	Results: .....	121
8.3.1	Nanogram scale: Reduction of GO deposited on Mo TEM grid: .....	121
8.3.2	Milligram scale: Reduction of GO and Mo blue solution.....	122
8.4	Discussion: .....	128
8.4.1	Nanogram scale:.....	128
8.4.2	Milligram scale: .....	129

8.5	Conclusion:.....	130
8.6	Acknowledgements .....	131
Chapter 9	Concluding remarks .....	132
References	.....	134
CURRICULUM VITAE	.....	149

## LIST OF FIGURES

Figure 1: Unit cell of diamond. Each carbon atom bonded with 4 neighboring carbon atoms with $sp^3$ hybridization. ....	2
Figure 2: Crystalline graphite structure with AB stacking. Each carbon in plane bonded with another three carbons with $sp^2$ hybridization.....	3
Figure 3: Honeycomb structure of graphene. Each carbon atom bonded with another 3 carbon atoms with $sp^2$ hybridization.....	5
Figure 4: C60 fullerene molecules, carbon nanotubes, and graphite can all be thought of as being formed from graphene sheets, i.e. single layers of carbon atoms arranged in a honeycomb lattice. [4].....	6
Figure 5: The energy, E, for the excitations in graphene as a function of the wave numbers, $k_x$ and $k_y$ , in the x and y directions. The black line represents the Fermi energy for an undoped graphene crystal. Close to this Fermi level the energy spectrum is characterized by six double cones where the dispersion relation (energy versus momentum, $\hbar k$ ) is linear. This corresponds to massless excitations [11].....	8
Figure 6: Model of GO structure by Lerf-Kilwonowski [20].....	10
Figure 7: (a) Top view of GMO with unit cell and parameters. Green and black spheres represent oxygen and carbon atoms respectively. (b) Perspective view of GMO. [27].....	12
Figure 8: Body centered crystal structure of Molybdenum .....	14
Figure 9: Crystal structure of orthorhombic Molybdenum trioxide .....	15
Figure 10: Molybdenum metal powder production [International Molybdenum Association]....	17
Figure 11 Carbothermal reduction of $MoO_3$ at different stages .....	18
Figure 12: Structure of monoclinic Molybdenum dioxide. ....	19
Figure 13 (a) Energy diagram of electrode potentials and electrolyte gaps in LIBs; (b) Schematic diagram of lithium intercalation and de-intercalation reaction mechanism in secondary LIBs with cathode connected to Cu connector and anode connected to Al connector .....	23
Figure 14: Ewald sphere constructed having radius $ k $ in direction of incident beam and terminating at Origin O and passing through point B and F in reciprocal space. As the reflecting plane is perpendicular to G, the diffracting plane for scattered wave AB contains plane AE. perpendicular to the plane of paper.....	31

Figure 15: Bragg's law. The incident X-ray beams are incident at glancing angle $\theta$ are reflected by $e^-$ cloud of atoms at different parallel planes separated by the distance 'd'. The lower incident X-ray beam has to travel $2d \sin\theta$ more distance than upper incident X-ray.....	33
Figure 16 (a) Diffraction pattern of single oriented crystal (b) Diffraction pattern of four crystals at different orientations with respect to the incident beam (c) Diffraction rings formed by randomly oriented powdered crystals (d) Integrated intensity of diffraction rings of polycrystalline sample. ....	34
Figure 17: 2D raw diffraction pattern of graphite with beam stopper blocking direct X-ray beam. To obtain larger Debye-Scherrer rings, the direct beam is not at the center of the detector.....	36
Figure 18: 1D integrated line intensity profile obtained from fig (17 ). ....	37
Figure 19: Different kind of electron scattering from thin specimen [51].....	39
Figure 20: Parallel beam of electron formed by condenser lenses [51].....	40
Figure 21: fig on left is DP mode and on right is image mode [51]. ....	42
Figure 22 Schematic representation of (a) the ionization process, (b) x-ray emission, and (c) Auger-electron emission. [52] .....	44
Figure 23: Basic components of FTIR spectrometer .....	47
Figure 24: The photo electric effect, in which x-ray is absorbed and a core level electron is promoted out of the atom.....	52
Figure 25: XAS experimental setup. IC1, IC2 and IC3 are ion chamber detectors used to detect intensity of X-ray photon incident on sample, transmitted from sample (or incident on reference sample) and transmitted from reference sample respectively. A double crystal monochromator is used. "Detector" is the detector for measuring fluorescence .....	58
Figure 26: Raw data of X-ray absorption coefficient (times thickness) vs Energy showing decrease in absorption coefficient with increase in X-ray energy but at Mo K -edge there is drastic increase in coefficient and it oscillates after that resulting XANES and EXAFS region .	59
Figure 27: $\mu(E)$ vs Energy graph for $Mo_2C$ . Pre-edge and post-edge fitting linear and cubical lines are drawn respectively for normalization. ....	60
Figure 28: $\mu(E)$ vs Energy graph of $Mo_2C$ after normalization. ....	61
Figure 29: $\chi(k)$ weighted by $k^2$ of $Mo_2C$ obtained from normalized $\mu(E)$ from figure 28 using equation 45.....	62

Figure 30: Fourier transform of $k^2 \cdot \chi(k)$ of $\text{Mo}_2\text{C}$ from figure 29 .....	63
Figure 31: The electromagnetic spectrum [60].....	64
Figure 32: The excitation process .....	65
Figure 33: Electronic levels and transitions.....	66
Figure 34: Splitting of d orbitals of $\text{Cu}^{2+}$ ion in presence of water as ligand. ....	67
Figure 35: XRD for GO provided by ACS Material for single layered GO. Diffraction peak at 7.34 Å and 3.39 Å are due to interplaner spacing between adjacent GO layers and precursor graphite layers (002) respectively .....	71
Figure 36:(a) SAED of GO before heating and (b) SAED of GO at 659°C.....	73
Figure 37: Comparison of XRD and SAED (before and after in situ vacuum annealing) of as purchased single layered GO Diffraction curves are stacked over another for better comparison	73
Figure 38: IR spectra of GO before and after heating .....	74
Figure 39: Visible image of GO sample in TEM grid for IR measurement. IR spectra were taken from the region between the crossbar. (a) Sample before heating in transmission mode (b) Sample before heating in reflection mode (c) Sample after heating in transmission mode (d) Sample after heating in reflection mode. ....	75
Figure 40: IR spectrum of Mo blue on diamond window compared with its precursor $\text{MoO}_3$ ....	81
Figure 41: UV Vis measurement of Mo blue and its precursor $\text{MoO}_3$ solution. Sharp absorption observed around 580 and 655 nm are due to characteristic emission peak of source and are irrelevant to the absorption by sample. ....	81
Figure 42: Mo K-edge XANES of Mo oxides [65].....	82
Figure 43: XANES of Mo blue along with $\text{MoO}_2$ and $\text{MoO}_3$ . Pre-edge peaks are present in both Mo blue and $\text{MoO}_3$ where as it is absent in $\text{MoO}_2$ . Also the features of XANES are quite similar for Mo blue and $\text{MoO}_3$ .....	82
Figure 44: Bright field TEM images of lacey carbon film with Mo blue solution before heating (a) and after in-situ heating at 762°C (b). Diffraction and spectroscopy data is taken from areas, like A1, that are initially amorphous and become ordered upon heating. Holes in the film are denoted as H1-H5. ....	88
Figure 45: (a) Bright field TEM images of lacey carbon film (after in-situ heating at 762°C) with Mo blue solution at region A2 with very small dark spots (b) Dark field image of same region	

after in-situ heating at 762°C showing bright spots which look dark in bright field image. Spots are formed because these nano particles have different contrast than that of amorphous lacey carbon..... 88

Figure 46: EDX at region A1 before heating showing the presence of carbon, oxygen and molybdenum in sample. Presence of sharp peak of Nickel is due to Ni grid. .... 89

Figure 47: EDX at region A1 after heating showing similar presence of carbon, oxygen, molybdenum and nickel from grid..... 90

Figure 48: SAED pattern of lacey carbon film with Mo blue solution (Region A1) before heating (a) and after in-situ heating (b) ..... 90

Figure 49: a) Intensity profiles of SAED of lacey C film exposed to Mo blue solution shows two broad peaks at room temperature (blue line) that are replaced by four diffraction peaks after heating (black line); b) Normalized intensity profiles of SAED of unheated lacey C with (blue line) and without (red line) Mo blue show great similarity in level of initial disorder..... 91

Figure 50: SAED of region A2 in lacey carbon with molybdenum blue after heating ..... 91

Figure 51: Integrated line profile of SAED from region A2 in sample (fig 50 ) compared with XRD line profile of standard MoO<sub>2</sub>..... 92

Figure 52: IR spectrum of Mo blue solution dried on diamond window compared with MoO<sub>3</sub> solution also dried on diamond window ..... 93

Figure 53:(a) Unit cell of two dimensional GMO (top view) with lattice vectors **a** and **b** equal to 3Å and angle between them equal to 122.64°C. (b) Model of 3D GMO in which GMO layers are in AB stacking (side view) similar to graphite having separation of 7.3 Å between alternate layers. .... 102

Figure 54: (a) SAED of nanogram scale GO/GMO composite after in-situ heating GO and Mo blue mixture in Ni TEM grid. Ring I and II are diffraction rings due to graphene (2.13 Å and 1.23 Å due to graphene planes (100) and (110) respectively). Rings III and IV are GMO rings which starts to form after 550°C during in-situ heating (2.68 Å due to (100) and (1-10) GMO planes and 1.54 Å due to GMO (110)). (b) Bright field image of GO/GMO composite from where SAED pattern was obtained. .... 102

Figure 55: Milligram scale: (a) SAED of milligram scale GO/ GMO composite showing rings similar to that in nanogram scale, (b) bright field image and (c) dark field image ..... 103

Figure 56: XRD and SAED diffraction integrated line profile of r-GO/GMO nanocomposite (milligram scale) in reciprocal distance compared with r-GO/GMO nanocomposite (nanogram scale) and simulated AB stacked GMO using X-ray powder diffraction ..... 103

Figure 57: Comparison of XANES of r-GO/GMO sample (milligram scale) with standard Mo<sub>2</sub>C, Mo metal powder, MoO<sub>3</sub> and MoO<sub>2</sub> powder. All of the XANES plots are stacked along vertical axis. .... 104

Figure 58: Milligram scale: (From bottom) Fourier transform of  $\chi(k)$  of milligram scale GMO and standard MoO<sub>2</sub>. The first peak at 1.5 Å is due to back scattering of photoelectron wave from nearest 6 oxygen atoms of the reference Mo atom. The second, third and fourth peaks from left are mainly due to scattering of the wave from first (1 Mo atom), second (1 Mo atom) and third (8 Mo atoms) nearest Mo neighbors respectively. The EXAFS shows very much similar structure of MoO<sub>2</sub> and Milligram scale r-GO/GMO, but in short range. Also simulated EXAFS of MoO<sub>3</sub> and EXAFS of experimental Mo<sub>2</sub>C are presented for comparison. .... 105

Figure 59: IR spectrum of (From bottom) GO, mixture of GO and Mo blue solution, nanogram scale r-GO/GMO, milligram scale r-GO/GMO and nanogram scale r-GO. .... 105

Figure 60: (a) SAED of Sample1, right after exposure to electron beam, showing diffraction rings due to Graphene (Rings I and II) and GMO (Rings III and IV) (b) SAED at another region at temperature 659°C also showing diffraction rings due to Graphene and GMO ..... 113

Figure 61: SAED of Sample2 (a) SAED at region 1 before heating showing ring I and II (b) SAED at region 1 at 601°C showing bright ring I and II and faint ring III and IV. (c) SAED at region 2 showing brighter rings I, II, III and IV. (d) SAED at region 3 with sample2 tilted at 15° resulting in blurring of diffraction rings at top and bottom compared to sides. .... 114

Figure 62: Nanogram scale: (a) Bright field image of GO with 3D nano-crystals embedded on it after heating it up to at 837 °C (b) dark field image from the same region (c) SAED pattern of GO, nearby Mo grid showing non-uniform diffraction rings formed due to polycrystalline 3D nanocrystals. .... 123

Figure 64: Nanogram scale: Integrated line profile of SAED of GO in Mo grid heated at 837 °C (Top) and integrated line profile of XRD of standard MoO<sub>2</sub> at room temperature (bottom) ..... 123

Figure 64: Nanogram scale: High resolution image of MoO<sub>2</sub>/r-GO nanocomposite showing crystallites of MoO<sub>2</sub> embedded inside reduced graphene oxide. 0.34 nm and 0.24 nm are the spacing consistent to the spacing of lattice planes of MoO<sub>2</sub>. .... 124

Figure 65: Milligram scale: (a), Bright field image of MoO<sub>2</sub>/r-GO composite transferred to Ni grid with lacey carbon showing dark spots due to formation of monoclinic MoO<sub>2</sub> on r-GO film lying over lacey carbon at region one. (b) Dark field image of the region one with bright spots of MoO<sub>2</sub>, and (c) SAED taken around the region one, displaying almost uniform diffraction rings having spacing due to MoO<sub>2</sub> crystals. .... 125

Figure 66: Milligram scale: (a) Bright field image of the sample at region two and (b) SAED at the region two showing the region is a single crystal of hexagonal graphene. (c) Bright field image at region three and (d) SAED at the region three shows the formation of graphite (e) At



region four, homogeneous distribution of tiny MoO<sub>2</sub> crystallites in thin film of GO held on lacey Carbon of Ni TEM grid and (f) SAED from the region four showing diffraction due to graphene (Ring I and II) along with diffraction rings due to MoO<sub>2</sub>..... 125

Figure 67: Milligram scale: Comparison of diffraction patterns of different forms of MoO<sub>2</sub>/r-GO nanocomposite with XRD of MoO<sub>2</sub> standard. From top: XRD of milligram scale MoO<sub>2</sub>/r-GO nanocomposite, XRD of GO before heating, SAED of milligram scale MoO<sub>2</sub>/r-GO nanocomposite, and XRD of Standard MoO<sub>2</sub>. Peak G<sub>c</sub> (3.65 Å) is due to diffraction from interplaner spacing between graphene sheets, G I and G II are diffraction from graphene planes with spacing of 2.13 Å (100) and 1.23 Å (110) respectively..... 126

Figure 68: Milligram scale: Weighted Fourier transform of  $\chi(k)$  of Standard MoO<sub>2</sub> and milligram scale MoO<sub>2</sub>/r-GO nanocomposite showing similar peak in short range with small difference in position of peaks due to presence of GO in nanocomposite. Also there is absence of long range ordering in the nanocomposite. The first peak at 1.56 Å is due to scattering of photo electron wave by the 6 nearest neighbor oxygen in monoclinic MoO<sub>2</sub>, the second peak at 2.2 Å is mainly due to scattering of the wave from first Mo neighbor and the third peak at 2.7 Å is mainly due to the scattering of the wave from the second nearest Mo atom and the peak at 3.2 Å is due to 8 third nearest Mo atoms at 3.694 Å..... 126

Figure 69: Milligram scale: Normalized XANES of milligram scale MoO<sub>2</sub> showing similar features to that of MoO<sub>2</sub> standard. Normalized absorption of Mo<sub>2</sub>C, Mo, MoO<sub>3</sub>, MoO<sub>2</sub> and Milligram scale MoO<sub>2</sub>/GO from top to bottom. The plots are stacked along vertical axis. .... 127

Figure 70: Milligram scale: Absorbance IR spectrum of ex-situ heated Mo blue/GO in vacuum showing presence of epoxide group (1200 cm<sup>-1</sup>) and carbon- carbon double bond stretching vibration (1560 cm<sup>-1</sup>). ..... 127

## LIST OF TABLES

Table 1: Comparison of spacing of diffraction rings formed in Lacey carbon and GO .....	95
Table 2: Pre-edge and Edge peak energies of Mo, Mo <sub>2</sub> C and Mo-oxides with milligram scale GO-GMO .....	104

## ACKNOWLEDGEMENTS

I want to thank my advisor Prof. Carol J. Hirschmugl for her guidance, consistent support and encouragement. I like to express my gratitude to Prof. Marija Gazdardziska-Josifovska for her valuable instruction during my study and research.

I would also acknowledge my PhD committee members Prof. Michael Weinert, Prof. Junhong Chen and Associate Prof. Peter Schwander for their priceless guidance and encouragement extended to me.

I wish to thank Prof. Paul Lyman, Dr. Marvin Schoefield, Dr. Eric Mattson and Mr. Donald P. Robertson for their help and support.

## **Chapter 1 Background and Introduction**

### **1.1 Organization of the Dissertation**

Chapter 1 discusses about literature review or work that had been performed before I started my research, brief introduction of materials used in the experiment and motivations for my research work. Chapter 2 focuses on different instrumentations and methods used in research with some theory. Chapter 3 and 4 discusses about the characterization of two precursor material that were used in experiment. Chapter 5 is on formation of graphene and graphene monoxide on amorphous lacey carbon. Chapter 6 discusses about the formation and characterization of nanocomposite of reduced graphene oxide and graphene monoxide in milligram scale. Chapter 7 discusses formation of nanocomposite of molybdenum dioxide and reduced graphene in milligram scale. At the end, in chapter 8, I have discussed about *in situ* formation of graphene monoxide from mixture chromium dioxide and graphene oxide by electron bombardment.

### **1.2 Crystalline Allotropic forms of carbon**

Carbon is one of the most abundantly found element in the earth, both in free state and in compound state with oxygen and hydrogen etc. It is non-metallic element with atomic number 6. Its position in periodic table is IVA which is also the group of elements like silicon (Si) and germanium (Ge). Semiconductors made from Si and Ge are of great importance in modern electronics. Due to its small size and 4 valence electrons having similar energies, their wavefunctions mix easily, facilitating hybridization of their orbitals. This unique ability to

hybridize sets apart from other elements and allows carbon to form 0D, 1D, 2D and 3D structures (Saito, Dresselhaus et al. 1998)

### 1.2.1 Diamond

Diamond (similar to Si and Ge) is face centered cubic ( $Fd\bar{3}m$ ) space group. The primitive basis of diamond has two identical atoms at coordinates (000) and  $(\frac{1}{4}, \frac{1}{4}, \frac{1}{4})$ . As conventional unit cube of fcc lattice contains 4 lattice points, the conventional unit cube of diamond structure contains  $2 \times 4 = 8$  atoms [1]. Strong covalent bond formed due to  $sp^3$  hybridization of orbitals of carbon atoms make it the hardest crystal in the earth. Due to its hardness it is mostly used as cutting material and due to its high refractive index it is used as gemstone. Though it has structure similar to that of Si and Ge, a pure diamond is insulator as it's bandgap is 5.5 eV. However, it's one of the best conductors of heat due to its strong covalent bond and low phonon scattering (5 times higher than copper) [2].

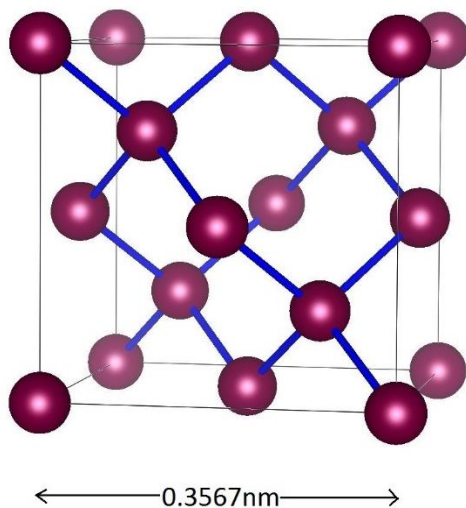


Figure 1: Unit cell of diamond. Each carbon atom bonded with 4 neighboring carbon atoms with  $sp^3$  hybridization.

### 1.2.2 Graphite

It is layers of hexagonal carbon sheets that are stacked on top of each other. Each carbon in hexagonal sheet are  $sp^2$  bonded with separation of  $1.42 \text{ \AA}$  and each layers are separated by a distance of  $3.35 \text{ \AA}$ . Each carbon atom in the plane is covalently bonded with another 3 carbons also in plane by  $sp^2$  hybridization of orbitals. Hence out of 4 valence electron of carbon, the fourth electron is free which makes graphite electrically conductive. The bonding between layers of carbon is weak van der Waals, which allows layers of graphite to slide over each other and also makes layers to exfoliate easily. However,  $sp^2$  bonding in between atoms in the same layer of graphite are even more stronger than  $sp^3$  bonding in diamond. Graphite is used as lubricant and electrodes.

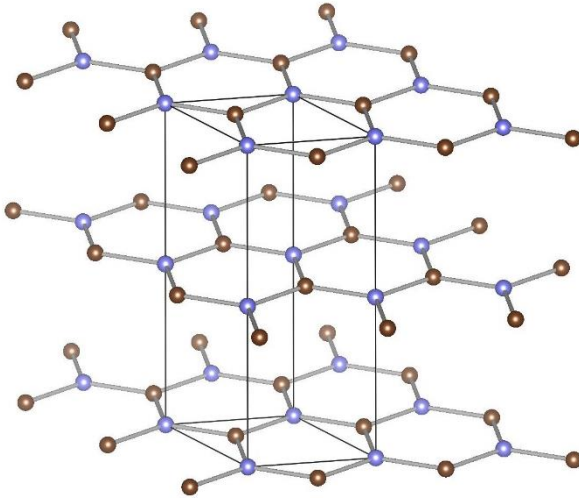


Figure 2: Crystalline graphite structure with AB stacking. Each carbon in plane bonded with another three carbons with  $sp^2$  hybridization

### 1.2.3 Graphene

In 2004, Konstantin Novoselov, Andre Geim and their collaborators, mechanically exfoliated a

single layer of graphite, transferred to substrate and did electrical measurement. This single layer of honeycomb structure of carbon in which each carbon atom is bonded with 3 another carbon atom in a plane with strong  $\sigma$ -bond is called graphene.

### 1.2.3.1 Structure of graphene

Graphene is a two dimensional, a single atomic layer of  $sp^2$ -bonded carbon atoms in which each carbon atoms are separated from another by 1.42 Å and a unit cell of graphene has lattice vectors of 2.46 Å ( $\mathbf{a}=\mathbf{b}= 2.46 \text{ Å}$ ) and angle between them equal to  $120^\circ$ (or  $60^\circ$ ). Stability of graphene can be attributed to tightly packed carbon atoms with the  $\sigma$ -bonding (strongest bond know so far between any two atoms) between them or  $sp^2$  hybridization.  $sp^2$  hybridization ( $\sigma$  bonding) is due to combination of s,  $p_x$  and  $p_y$  orbitals of carbon atoms. The final  $p_z$  electron makes up the  $\pi$ -bond. The  $\pi$ -bond hybridize together to form the  $\pi$ -band and  $\pi^*$ - bands. These bands are responsible for most of graphene's notable electronic properties, vis the half filed band that permits free-moving electrons [3].

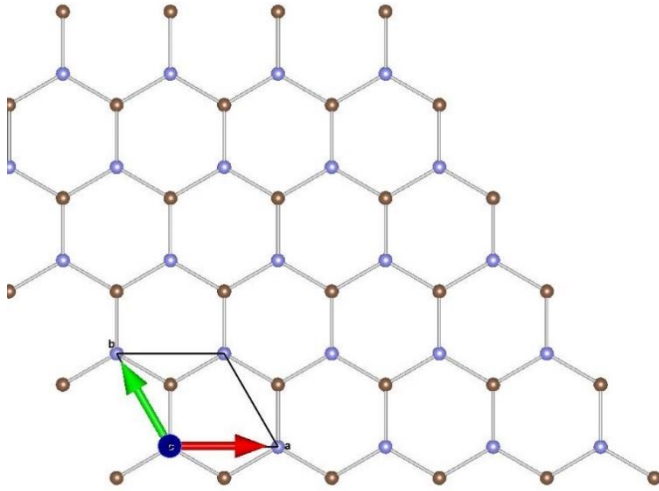


Figure 3: Honeycomb structure of graphene. Each carbon atom bonded with another 3 carbon atoms with  $sp^2$  hybridization.

### 1.2.3.2 Properties of graphene

It is ultra-light yet immensely tough, 200 times stronger than steel but incredibly flexible, thinnest material, transparent and very good conductor of heat and electricity but it acts as a perfect barrier for any molecule to pass through it.



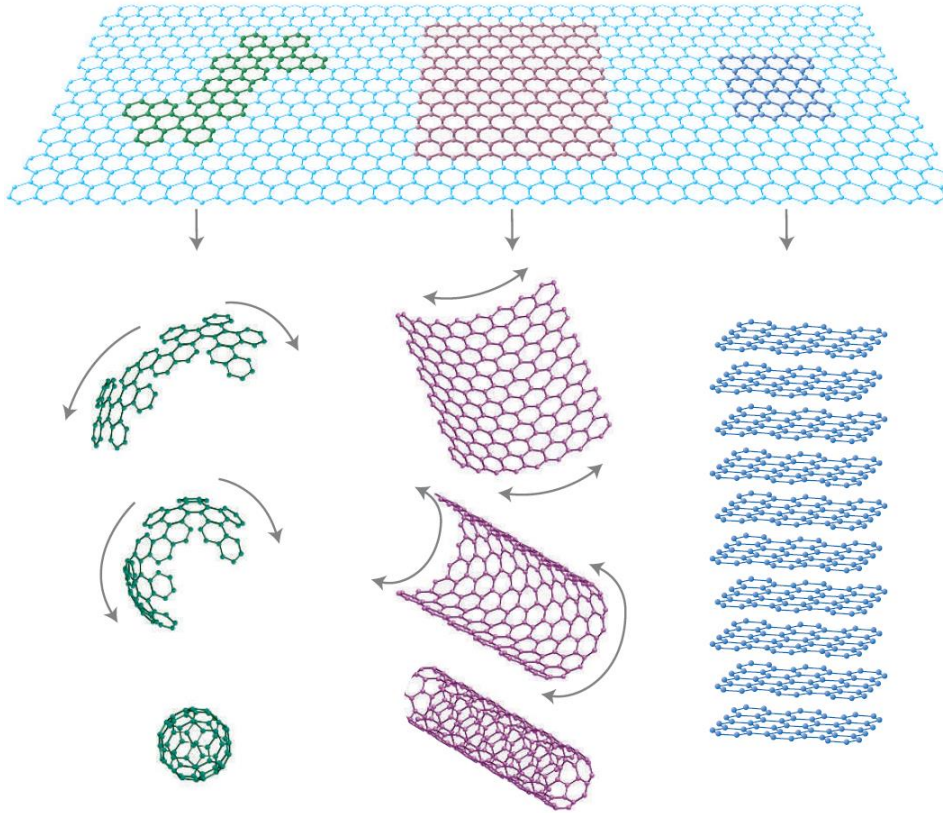


Figure 4: C60 fullerene molecules, carbon nanotubes, and graphite can all be thought of as being formed from graphene sheets, i.e. single layers of carbon atoms arranged in a honeycomb lattice. [4]

3D Graphite can be considered as a stacking of graphene sheets in fig (2), stacked together by much weaker van der Waals force compared to covalent force which binds together C-atoms in graphene plane. In 1985 Robert Curl, Harold Kroto and Richard Smalley discovered 0D graphitic allotrope C<sub>60</sub> (fullerenes) [5], in which a graphene sheet is crumpled forming a sphere of a graphene similar to a football, with 60 vertices and 32 faces, 12 of which are pentagonal and 20 hexagonal. And when single or multilayer of graphene rolled up, a single-wall or multi-wall carbon nanotube is formed with diameter of several nm [6].

Electronic structure and the linear dispersion relation in graphene were predicted by P.R. Wallace in 1947 [7]. But it was presumed that a single atomic layer of crystal is thermodynamically unstable at any finite temperature and there were doubt that a single layer of graphene can ever exist. In 2004, Geim and Novoselov, micro-mechanically exfoliated HOPG and showed 2D crystal of graphene were found to exhibit in high crystal quality where charge carriers can travel thousands of interatomic distances without scattering [8] [9] [10].

### 1.2.3.3 Electronic structure of graphene

Fermi surface of graphene is characterized by six double cones as shown in fig 5). In intrinsic graphene Fermi level is situated at the connection points of these cones. Since density of states of the material is zero at that point, the electrical conductivity of intrinsic graphene is quite low and is of the order of the conductance quantum  $\sigma \sim e^2/h$ . However, the Fermi energy can be changed by an electric field so that the material becomes either n-doped (with electrons) or p-doped (with holes) depending on the polarity of the applied field [11]. It can also be doped by adsorbing on its surface (for example water or ammonia) [11]. The electrical conductivity of doped graphene is potentially quite higher than even copper at room temperature [11]. The zero bandgap of graphene limits its use in field-effect transistors in nanoelectronics, so the p-type semiconducting reduced graphene oxide (r-GO) is an alternating route [12].

Close to the Fermi level the dispersion relation for electrons and holes is linear. Since the effective masses are given by the curvature of the energy bands, this corresponds to zero effective mass. The equation describing the excitations in graphene is formally identical to the Dirac equation for massless fermions which travel at a constant speed. The connection between

points of the cones are therefore called Dirac points.

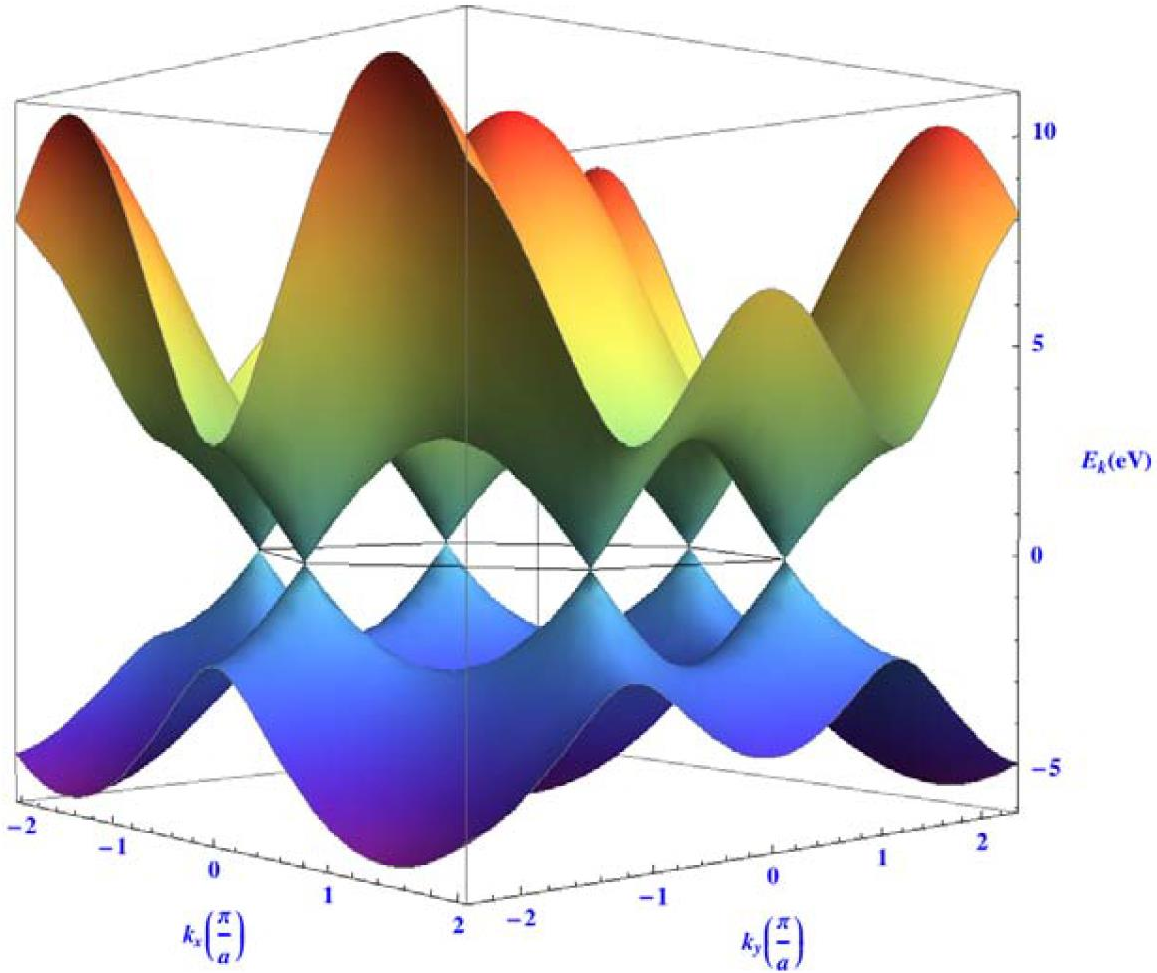


Figure 5: The energy,  $E$ , for the excitations in graphene as a function of the wave numbers,  $k_x$  and  $k_y$ , in the  $x$  and  $y$  directions. The black line represents the Fermi energy for an undoped graphene crystal. Close to this Fermi level the energy spectrum is characterized by six double cones where the dispersion relation (energy versus momentum,  $\hbar k$ ) is linear. This corresponds to massless excitations [11].

### 1.3 Graphene oxide (GO)

Well before the discovery of graphene in 2004, in an attempt to determine atomic weight of graphite, Brodie (1859) used potassium chlorate and fuming nitric acid as oxidizing agents to prepare multilayered graphene oxide sheets called graphite oxide [13]. In 1958 Hummers and

Offeman developed a rapid, relatively safe and efficient method of preparation of graphite oxide by oxidizing graphene (in layers of graphite) with concentrated sulphuric acid, potassium permanganate, sodium nitrate and obtained C:O atomic ratio of 2.25 [14]. The level of oxidation depends a lot on the method of oxidation, reaction environment and the precursor graphite [15]. Although, the Graphite oxide was first prepared more than 150 years ago, the chemical structure of it is yet to be determined. Graphite oxide consists of large number of functional groups including alcohols and epoxides, but it has stacking of layer GOs similar to graphite but with wider spacing (6-12 Å) with intercalation of water molecules between the layers [16]. Recent studies show that [17] [18], GO is an oxidized graphene sheet having a basal plane decorated mainly with epoxide and hydroxyl groups, and carbonyl and carboxyl groups located presumably at the edges (Lerf-Klinowski model). Fourier transform infrared spectra (FTIR) on GO also confirms existence of epoxy group (-O-) at 1050 cm<sup>-1</sup>, ketone group (-C=O) at 1680 cm<sup>-1</sup>, C-O vibrational mode at 1380 cm<sup>-1</sup>, C-OH stretching vibration at 3470 cm<sup>-1</sup> [19].

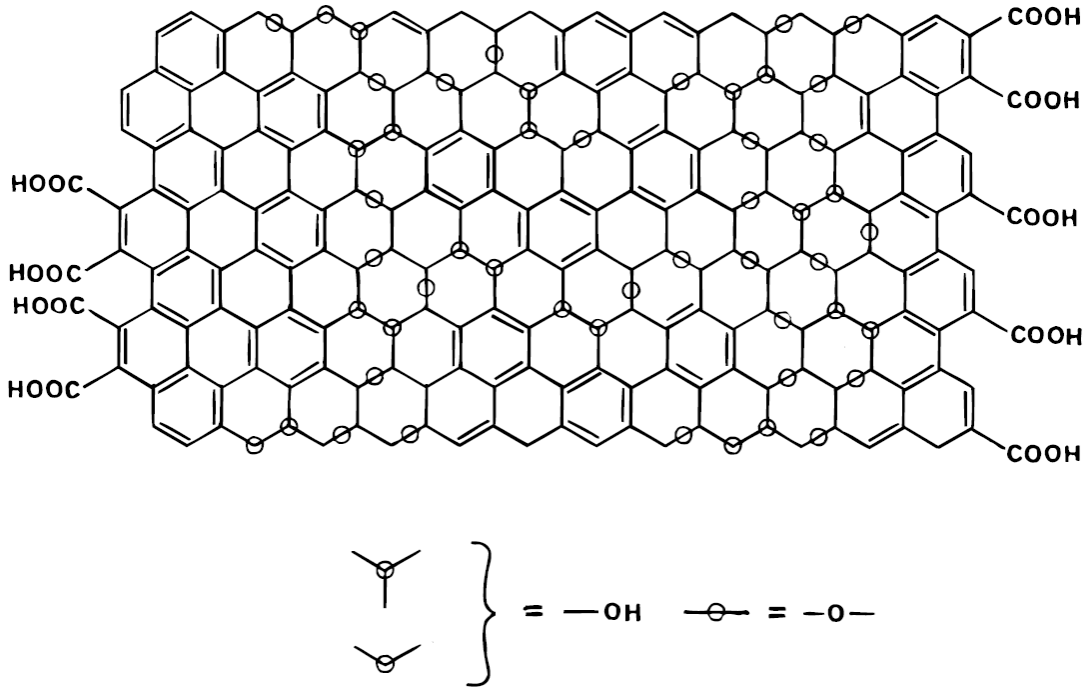


Figure 6: Model of GO structure by Lerf-Kilwonowski [20]

GO is electrically insulating materials due to disrupted  $sp^2$  bonding, however it can be made conductive by restoring  $\pi$ -network by its reduction [21]. Thus formed graphite oxide can be easily exfoliated by sonication to produce homogenous colloidal suspensions of GO sheets in aqueous [22] and various organic solvents. The thickness measurement done on GO sheet deposited on mica substrate using AFM (Atomic force microscopy) has shown that GO are typically single sheet (1 nm thickness on mica) [15]. The surface charge (zeta potential) of GO shows these sheets possess negative charge when dispersed in water [23]. This electrostatic repulsion together with hydrophilicity, enable them to form stable colloids in water. The exponential upsurge of interest in GO is due to its ability of cheap production for graphene like material. However, as mentioned earlier GO is insulator and thermally unstable, so it isn't useful

for most of the practical applications. However, its property can be greatly improved through reduction. The reduction can be done either chemically or thermally. Hydrazine [22] and sodium borohydride [24] are the most popular reducing agent used for the reduction. The reduced GO formed by treating GO with chemicals are called chemically reduced graphene oxide (CRGO) and by thermal treatment is called thermally reduced graphene oxide (TRGO). Both CRGO and TRGO get great enhancement in electrical conductivity but still they are inferior than pure graphene. CRGO still doesn't have C:O ratio not much higher than 6:1. While reducing GO with hydrazine in water, the brown coloured suspension turns black, aggregates and finally precipitates [25], which is presumably due to the removal of oxygens, turning hydrophilic GO into hydrophobic CRGO.

Nanoporous graphene and multilayered GO exhibits unlimited potential to be used as membranes for desalination with 100% salt rejection [26].

## 1.4 Graphene monoxide

### 1.4.1 Structure

GMO is a graphene based 2D structure having quasi-hexagonal/centered-rectangular unit cell with two carbon atoms bridged by a double-epoxide pair. It has very high 1:1 C:O ratio [27]. Experimentally, it is prepared by *in situ* thermal reduction of multilayered GO in presence of Mo metal between 550-700°C at high vacuum ( $10^{-7}$  torr) [27]. Unlike graphene which is semi-metallic and has zero bandgap, the GMO is reported to have calculated tunable bandgap which can be switched between direct and indirect, over a large range (0-1.35 eV) for accessible strains [28]. Recent study using DFT theory also predict bandgap engineering of GMO can also be performed by creating vacancy or defect in GMO crystal structure [29]. Structure of GMO:

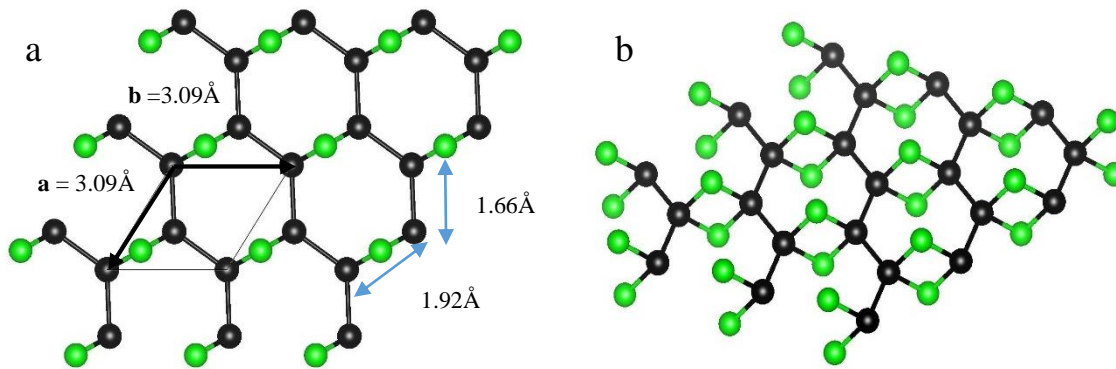


Figure 7: (a) Top view of GMO with unit cell and parameters. Green and black spheres represent oxygen and carbon atoms respectively. (b) Perspective view of GMO. [27]

Fig (7) shows 2D crystalline structure of GMO similar to graphene. Two of its carbon atoms are bridged by double-epoxy oxygen atoms. Due to bridging oxygen the overall area of unit cell is increased by 20% compared to graphene, lattice vectors  $a$  and  $b$  are increased to  $3.09 \text{ \AA}$  (from  $2.46 \text{ \AA}$ ) and angle between them increased to  $124^\circ$  (from  $120^\circ$ ). Also the C-C distance increased

to 1.66Å from 1.42Å. GMO structure has no of 3-fold symmetry as in graphene but has  $D_{2h}$  symmetry.

$sp^2$  hybridized bonding ( $\sigma$ ) between carbon atoms in graphene is the strongest bonding which gives graphene stiff regular hexagonal structure. But due to presence of double-epoxy oxygen between carbon atoms, the first-principles calculations has shown the structure of GMO is mechanically soft and its bond length and lattice parameters can be easily changed by applying small stress which eventually leads to GMO to have tunable bandgap [28]. Due its flexibility different groups have proposed slightly different parameters for its structure, mainly in the angle between its lattice vectors from 124-130°C.

#### **1.4.2 Future applications:**

Most of the theoretical studies have shown single layer GMO is thermodynamically stable and its tunable bandgap make it a good candidate for fabricating nano-devices such as sensors, transistors and nano-electronics [30]. Furthermore, Woo et.al. [31] has shown lowering of bandgap using calculation for bi-layered GMO with different orientations (0.418-0.448 eV) compared to mono-layered GMO of similar structure (0.536 eV) and also theoretically demonstrated semiconductor to metal transition by applying very small electric field of  $E_c = 0.22 - 0.3V/\text{Å}$  perpendicular to the basal plane of GMO. This lowering of bandgap for bi-layered GMO by applying electric field makes it useful in developing nano-scale field effect transistor in future.



## 1.5 Molybdenum and its oxides

### 1.5.1 Molybdenum

Molybdenum is a group VIB element, transition metal (d-block element) in periodic table. Due to its high melting point and as it forms hard and stable carbide forming in alloys, it is used in making hard steel alloys. It has a body centered cubic structure with lattice parameter  $a = 3.147 \text{ \AA}$ , with space group number: 229 and space group  $Im-3m$ . High melting point, low thermal expansion coefficient and high thermal/electrical conductivity make Mo a potential material for making power semiconductor components, glass-melting electrodes, and high temperature structure parts [32]. Molybdenum compounds are used as organic as well as inorganic catalysts. Molybdenum (IV) oxide ( $MoO_2$ ) and Molybdenum (VI) oxides ( $MoO_3$ ) are the most stable oxides. Other oxides found in literature are  $Mo_4O_{11}$ ,  $Mo_8O_{23}$ ,  $Mo_9O_{26}$ ,  $Mo_{13}O_{38}$ ,  $Mo_{17}O_{47}$ .

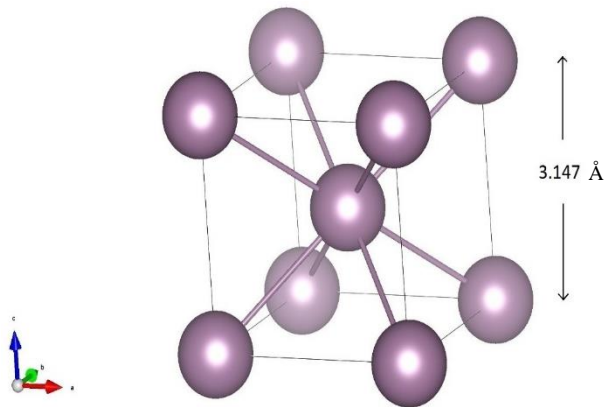


Figure 8: Body centered crystal structure of Molybdenum

## 1.5.2 Molybdenum(VI) oxide

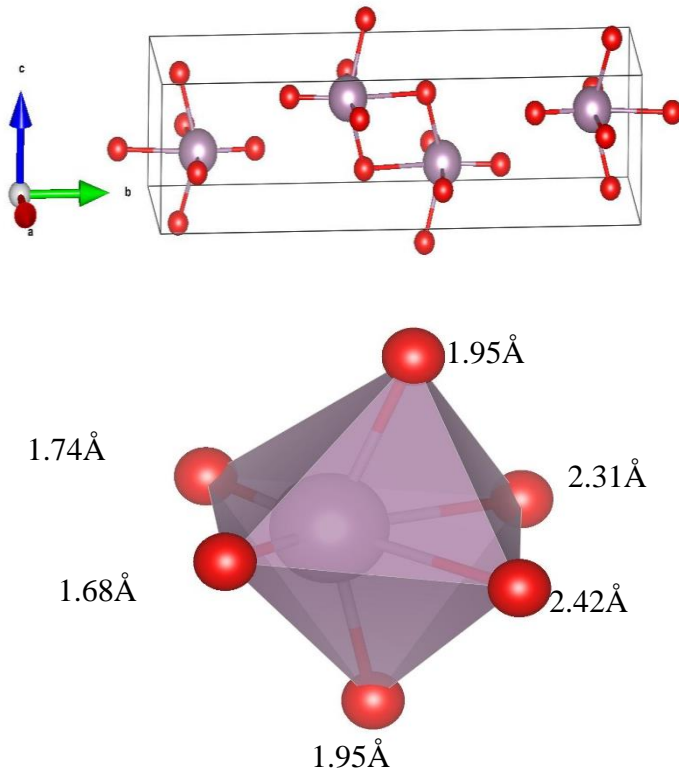
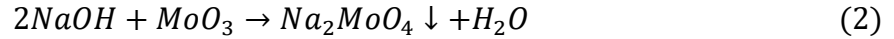
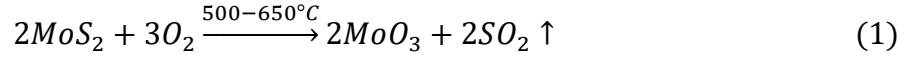


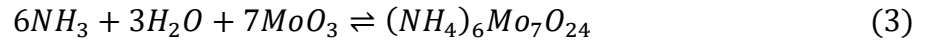
Figure 9: Crystal structure of orthorhombic Molybdenum trioxide

Molybdenum trioxide (MoO<sub>3</sub>) is the most stable oxide of molybdenum under oxidizing environment. This yellow or light blue solid is composed of layers of distorted octahedra in an orthorhombic crystal which lattice parameters  $a=3.9628 \text{ \AA}$ ,  $b=13.855$  and  $c=3.6964$ , space number 62 and space group (pnma) [33]. MoO<sub>3</sub> is the precursor compound for the most of the Mo compounds. However, molybdenite (MoS<sub>2</sub>) is the primary ore of Mo. After its purification, concentrated MoS<sub>2</sub> ore is roasted in air at 500-600 °C to get impure MoO<sub>3</sub> [34]. This impure MoO<sub>3</sub> is treated with

- (i) sodium hydroxide (NaOH) to obtain sodium molybdate (Na<sub>2</sub>MoO<sub>4</sub>) precipitate, which is used as a fertilizer and also used as a precursor for many Mo products in lab [34]

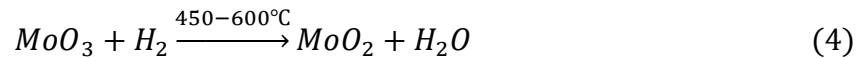


- (ii) Aqueous ammonia (NH<sub>3</sub>) to obtain Ammonium heptamolybdate ((NH<sub>4</sub>)<sub>6</sub>Mo<sub>7</sub>O<sub>24</sub>) in solution. This product is of great importance as the soluble product can be used for purification of MoO<sub>3</sub> and it is also used as a precursor of different oxides of Mo including MoO<sub>3</sub> in chemical synthesis [34].

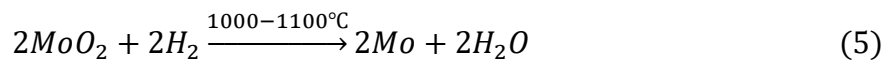


MoO<sub>3</sub> has high bandgap because all of the valence electron of Mo atom is bonded to neighbouring oxygen atoms [35].

According to international molybdenum association, Mo metal is manufactured by heating MoO<sub>3</sub> or (NH<sub>4</sub>)<sub>2</sub>Mo<sub>7</sub>O<sub>24</sub> in reducing H<sub>2</sub> atmosphere in two stages because conversion directly to metal releases heat that inhibits the process. In the first stage MoO<sub>2</sub> is produced



In the second stage, MoO<sub>2</sub> is reduced to molybdenum metal flowing H<sub>2</sub> at temperature 1000-1100°C.



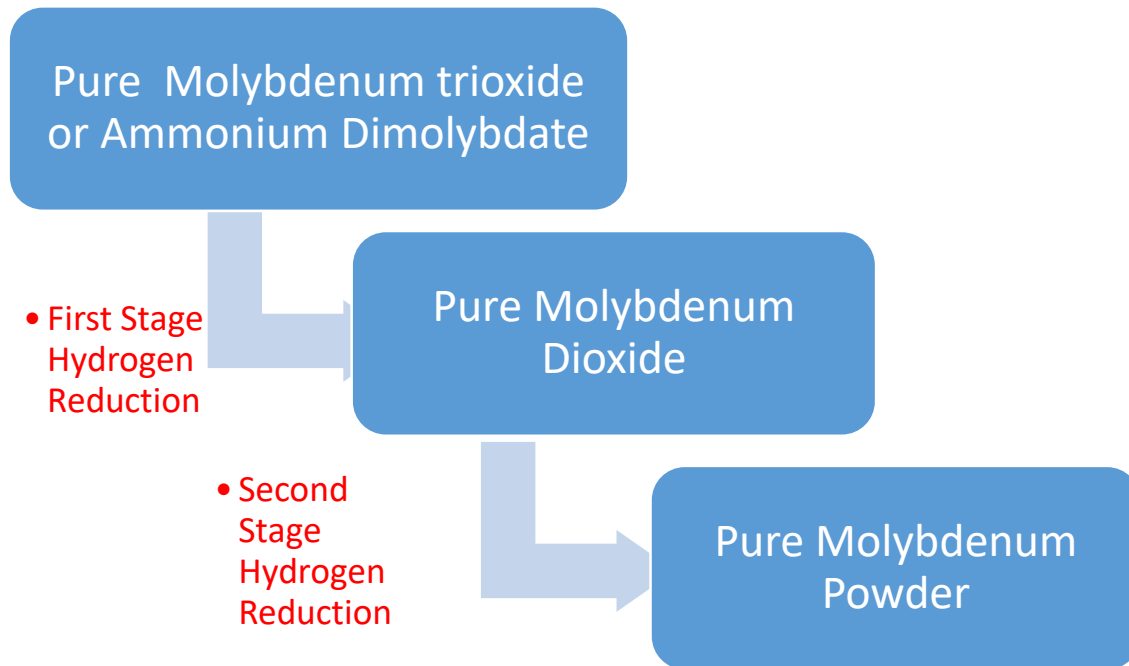
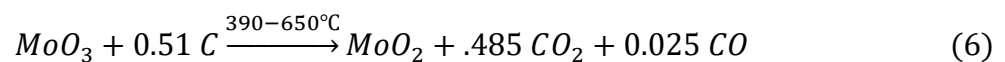
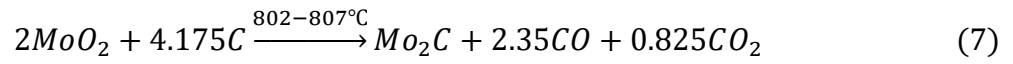


Figure 10: Molybdenum metal powder production [International Molybdenum Association]

An alternative for production of Mo is by carbothermic reduction of  $\text{MoO}_3$ . The detail mechanism of the reduction of  $\text{MoO}_3$  is described by Chaudhury et al. [36] and Hegedus et al. [37]. Carbothermic reduction include following steps. Based on the evolved gas composition and TGA, the reaction can be represented by the following chemical equation.



Not any molybdenum suboxide or others are formed as intermediated during this first stage of reaction. In second stage between 802 and 807°C  $\text{MoO}_2$  is converted into  $\text{Mo}_2\text{C}$  but Mo metal is formed during heating as an intermediate stage.



Finally, at 1000°C Mo metal is formed [37].

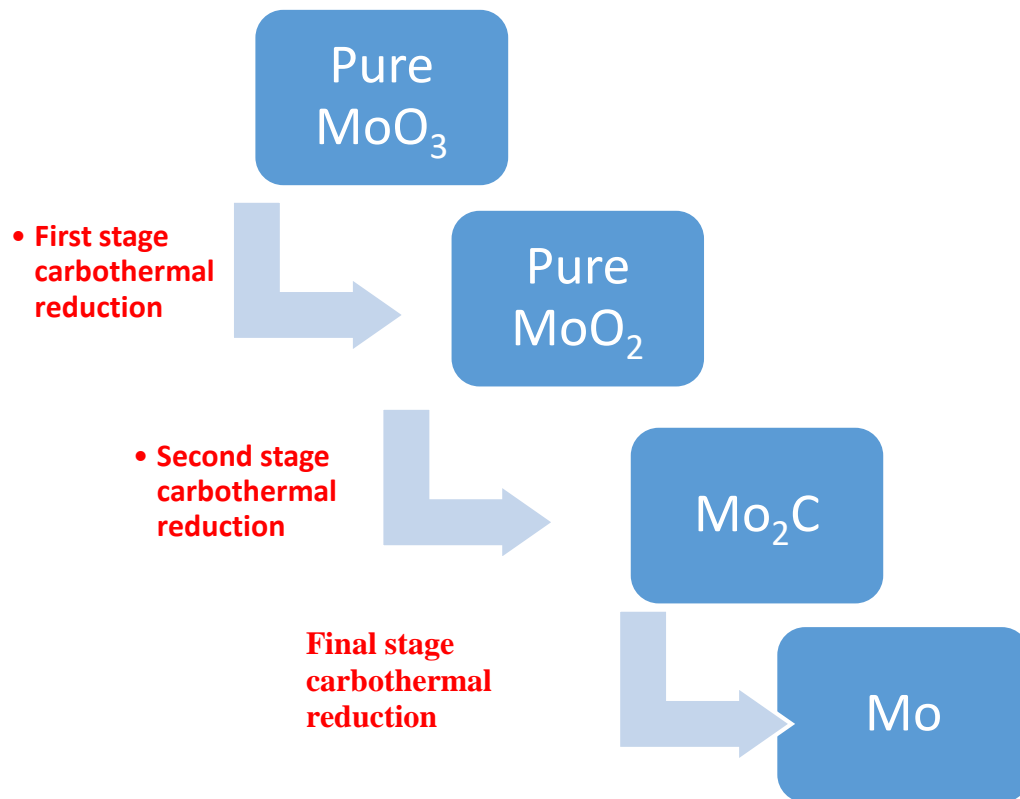


Figure 11 Carbothermal reduction of MoO<sub>3</sub> at different stages

### 1.5.3 Molybdenum(IV) oxide

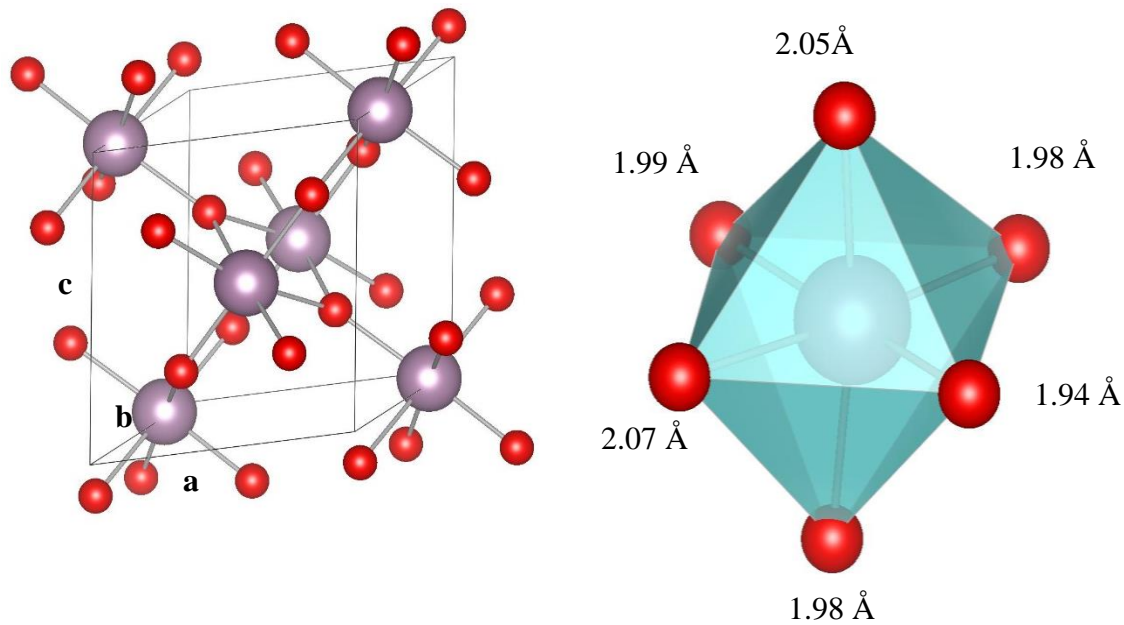


Figure 12: Structure of monoclinic Molybdenum dioxide.

Molybdenum dioxide ( $\text{MoO}_2$ ) is the most stable oxide of molybdenum under reducing environment. It is violet-coloured, monoclinic crystal having distorted rutile structure. Due to its distorted structure, the Mo atoms in crystal are off-centered, leading to alternating short and long Mo-Mo bonding. As this complex bonding is formed due to delocalization of some of the Mo electrons in conduction band, it possesses metallic conductivity. Nanoscale  $\text{MoO}_2$  is of great interest due to its importance in technical applications as a catalyst for partial oxidation of hydrocarbons, solid oxide fuel cell anodes and high-capacity reversible lithium ion battery anodes [34].  $\text{MoO}_2$  supported on porous carbon catalyst is reported to have improved oxidative desulfurization of thiophene present in crude oil and this improved desulphurization can be attributed to the more number of free electrons and smaller steric hindrance in  $\text{MoO}_2$  [35].

MoO<sub>2</sub> decorated on reduced graphene due to its good chemical stability, high metallic conductivity, high surface area and high theoretical capacity of energy storage (838 mA h g<sup>-1</sup>) shows an enhanced electro-catalytic hydrogen evolution reaction with a low potential [38]. Hydroisomerization of alkanes (C<sub>4</sub>-C<sub>6</sub>) has a commercial importance in oil industry, since this process is used to increase the gasoline octane. Bulk MoO<sub>2</sub> as prepared by H<sub>2</sub> reduction (of MoO<sub>3</sub>, equation 4) has shown good selective isomerization reaction of alkanes [39] [40].

### **1.6 Lithium Ion Batteries (LIBs):**

With the industrial development and improve in living standard, the demand for energy is also growing continuously. So far fossil fuel is the major contributor for energy supply. But due to over exploitation of coal and petroleum there is sharp rocketing in their prices. Fossil fuels are also responsible for pollution and one of the major contributor in emission of greenhouse gas (CO<sub>2</sub>). Wind, solar and hydro-electricity can be a good alternative for the traditional fossil fuel as they are renewable and environment friendly. But these alternative sources are unreliable. They are not available when it is necessary. Sun energy can be harnessed only during sunny day, wind blows only for few hours during day and most of the hydro-electricity project are run off the river type. Energy form these alternative sources are wasted when it is not necessary and they are not available when it is necessary. So, it is necessary to develop a device which can store these energies when there is excessive production and utilize them when there is scarcity. The most popular device which can store energy is lead acid cell, which stores electrical energy in the form of chemical energy during charging and it can be discharged easily when it is necessary. It is cheap and easily available but energy storing capacity is very poor, need high maintenance and it uses highly toxic lead and sulphuric acid as active material. The battery which has the highest

volumetric energy density and specific energy density currently available in the market is Lithium ion battery (LIB). The major advantage of LIBs are light, portable, availability in any shapes and sizes, high energy density, low memory effect<sup>1</sup>, can be recharged for about (400-1200) cycles and low self-discharge rate (8% at 20°C per month). This rechargeable battery is used in most of the electronic devices such as smartphones, laptops, cameras, and also used in electric vehicles, electric drills etc.

The active material in LIB are two electrodes, positive electrode (Cathode) and negative electrode (Anode) separated by a Separator, a permeable membrane soaked with non-aqueous electrolyte (Li-salt) mixed in organic solvent which provide a conductive medium for Li<sup>+</sup> ions to move between electrodes. The choice of electrodes depends upon their electrochemical potential values ( $\mu_A$  and  $\mu_C$  for anode and cathode respectively) as well as their position relative to HOMO-LUMO<sup>2</sup> energy gap ( $E_g$ ) of the electrolyte [41]. For a stable cell,  $\mu_A$  should be lower in energy than the LUMO of the electrolyte, otherwise the electrolyte will be reduced, and  $\mu_C$  should be higher in energy than the HOMO of the electrolyte to inhibit the oxidation of the electrolyte [41]. LIB rely on reversible insertion (or intercalation) of Li<sup>+</sup> ions between cathode and anode materials respectively. For an example cathode can be layered structure of metal oxide

---

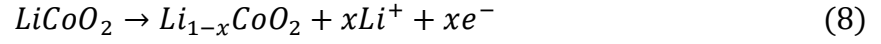
<sup>1</sup> Need to be discharged completely (to 25% in NiCd battery) before recharging, otherwise loses maximum energy capacity

<sup>2</sup> Highest occupied molecular orbital-Lowest unoccupied molecular orbital



(lithium cobalt oxide,  $\text{LiCoO}_2$ ) and anodes are made of layered carbon materials (graphite,  $\text{C}_6$ ) metal oxide and carbon respectively. During charging

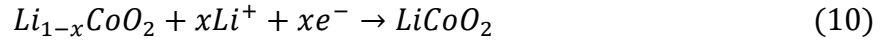
At Cathode:



At Anode:



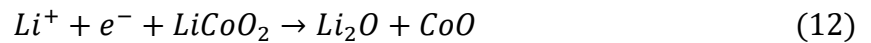
During discharging, at Cathode:



At Anode:



These reactions are reversible. However, over discharge of LIB saturates  $\text{LiCoO}_2$  and dissociates into  $\text{Li}_2\text{O}$  and  $\text{CoO}$  irreversibly at cathode [42].



Also overcharging up to 5.2 volts decomposes  $\text{LiCoO}_2$  into  $\text{CoO}_2$  irreversibly [43].



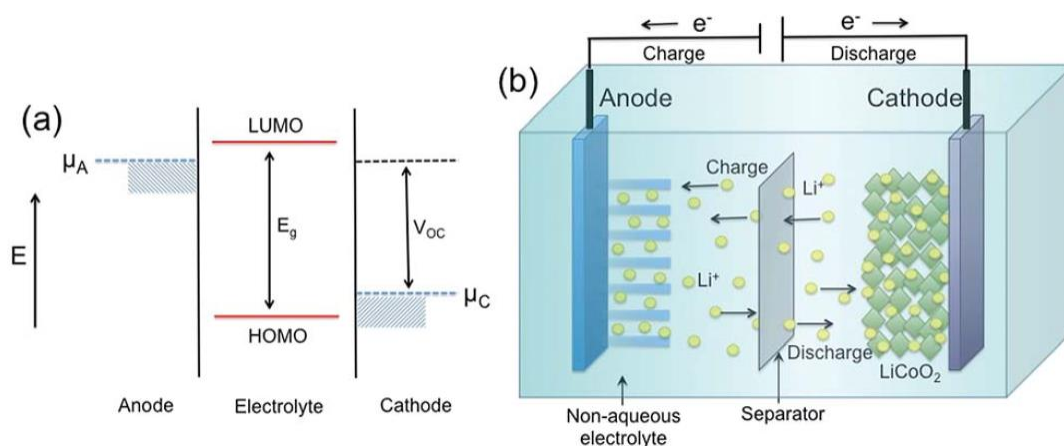


Figure 13 (a) Energy diagram of electrode potentials and electrolyte gaps in LIBs; (b) Schematic diagram of lithium intercalation and de-intercalation reaction mechanism in secondary LIBs with cathode connected to Cu connector and anode connected to Al connector

Above equations show that during charging oxidation state of Co in  $\text{Li}_{1-x}\text{CoO}_2$  changes from +3 to +4, and back to +3 during discharging. This reaction is reversible only if  $x < 0.5$ . This means LIB with can't be discharged completely.

The other commercially available LIB have lithium iron phosphate (polyanion) or lithium manganese oxide (spinel) or their derivatives as cathode. Typically, electrolyte  $\text{LiPF}_6$  salt is mixed with hydrocarbon based mixture (ethylene carbonate, dimethyl, diethyl and ethylmethyl carbonates) including multiple additives [44].

The most commercial LIBs use graphite which is conducting and expands only modestly as anode material. But its theoretical specific capacity is only 374 mAh/g. Graphite can be replaced by metal oxides such as iron oxide, cobalt oxide, nickel oxide and molybdenum oxides to get higher specific capacity. 6 atoms of carbons are necessary for insertion of 1 lithium ion but 6 and 4 ions of Li can be inserted per molecule of  $\text{MoO}_3$  and  $\text{MoO}_2$ , so theoretical specific charge capacity of them is 1175 mAh/g and 840 mAh/g respectively. Also their high density enables them to store more energy per volume. But diffusion kinetics in metal oxides restrict their

capacities. Also huge volume variation of metal oxides during charging and discharging causes detachment of active material from the current collector [45] and pulverization of electrode material results into rapid decline in capacity after few cycles [46]. Also, silicon is 10 time more capable of storing Li ions but it swells enormously during charging, causing disconnection between contacts. So researcher trying to bind silicon and carbon together with flexible polymer binder to maintain conductivity with anode. But unfortunately, repeated swelling and shrinking of silicon during lithiation and delithiation of silicon push away carbon particles [47] Since bulk metal oxides have problem due to volume variation, their nanostructure can be used for making anode of LIB since they have better accommodation of strains resulting from Li-insertion and extraction. Nano particles of molybdenum oxides in different shapes such as 1D nanorods, mesopores or 3D flower like rods have been reported. Though  $\text{MoO}_3$  (bandgap 3.1 eV) has higher specific capacity than  $\text{MoO}_2$ , latter one is preferred for making anode due to its metal like electrical conductivity as well as its high thermal and chemical stability [48]. A lot of efforts are being made to make nanocomposite of  $\text{MoO}_2$  or  $\text{MoO}_3$  with bulk carbon, carbon nanotubes (CNTs) and graphene.  $\text{MoO}_2$ -Carbon nanocomposite composed of inter-connected  $\text{MoO}_2$  nanocrystals with carbon nanocoating on the surface synthesized by a facile one-pot hydrothermal method followed by thermal annealing in nitrogen flow has exhibited high specific capacity (high discharge capacity of  $629 \text{ mAhg}^{-1}$  retained when cycled at  $200 \text{ mAg}^{-1}$  for 50 cycles) anode material [49].  $\text{MoO}_2$ /multiwalled carbon nanotube hybrid composed of spherical flower like nanostructures of  $\text{MoO}_2$  interconnected by MWCNTs prepared by one step hydrothermal route shows high reversible electrochemical lithium storage capacity of  $1025.2 \text{ mAhg}^{-1}$  at current density of  $100 \text{ mAg}^{-1}$  after 160 cycles, which can be attributed to inherent electron conducting nature of MWCNTs interconnecting  $\text{MoO}_2$  nanostructures [45]. Due

to high mobility, large surface area, excellent electrical and thermal conductivity of graphene make it competitive material for making anode for LIB. Graphene layers prevents both volume changes and aggregation of metal oxide nanoparticles during charge/discharge processes as oxide nanoparticles are sandwiched between graphene sheets and therefore can't agglomerate. Furthermore, the attachment of metal oxide or any other inorganic moiety on graphene effectively inhibits the restacking of graphene layers. Graphene can be made in large scale by reducing GO. Thus prepared r-GO have interplaner spacing higher than that of graphite which enable r-GO to intercalate more Li ions without much swelling.

## 1.7 Objective of Dissertation:

Experimentally, GMO has been prepared by *in situ* thermal reduction of GO in Mo TEM grid (in nanoscale) with regions of GMO in mixture with graphene and graphene oxide [27]. GMO so formed has 2D structure, so it showed uniform two dimensional diffraction rings during SAED. However, during annealing experiment, 3D nanocrystals were also observed in bright and dark field imaging and those were identified as nano monoclinic crystals of MoO<sub>2</sub> by high resolution imaging and selected area electron diffraction. In addition, EELS measurement done by Prof. Marija Gajdardziska-Josifovska at Arizona, also showed the presence of oxide of Molybdenum in the region of GMO/GO nano-composite. The choice of using Mo as a TEM grid for *in situ* thermal annealing of GO [27] is because of its high melting point and chemical stability at high temperature in vacuum. Due to thermal and chemical stability, Mo has been very much popular in making high quality steel. But the experiments have shown Mo from TEM grid move to the sample during heating and Mo is not chemically stable at higher temperature in presence of GO.

On further annealing experiments of GO in Ni, Au, Pt and Cu grid under exactly similar condition as described in [27] have shown that GMO can't be formed without catalyst (Molybdenum metal). MoO<sub>2</sub>/reduced GO was not initially a desired outcome from the thermal reduction experiment, but literatures have shown that MoO<sub>2</sub> along with reduced GO as a nano-composite has great potential in making LIBs.

So, the main objective of my PhD dissertation is to

1. understand the role of Mo catalyst in making GMO

2. Find out the bi-products of Mo formed along with GMO and reduced GO
3. Manufacture GMO/GO nano-composite in large scale
4. Solve the structure of GMO using other techniques such as powdered XRD and XAS and compare the results with compounds of Mo.
5. Make GMO or graphene from sources other than GO
6. Prepare MoO<sub>2</sub>-reduced GO nanocomposite in larger scale and use it in making energy storage device.
7. Find out elements or compounds other than that of Mo for making GMO.

## Chapter 2 Methods and instrumentations

### 2.1 Crystallography

An ideal crystal is formed by infinite repetition of identical structural units in space. In crystal group of atoms identical in composition, arrangement and orientation (basis) is repeatedly attached to regular periodic array of points in space (lattice).

$$\text{Crystal Structure} = \text{Lattice} + \text{Basis} \quad (14)$$

Mathematically, lattice is defined in term of three non-coplanar, fundamental translation vectors  $\vec{a}_1$ ,  $\vec{a}_2$  and  $\vec{a}_3$ , such that the atomic arrangement in crystal look identical when viewed from the point  $\vec{r}$  and  $\vec{r}'$ . Where

$$\vec{r}' = \vec{r} + \vec{T} \quad (15)$$

And 
$$\vec{T} = u_1\vec{a}_1 + u_2\vec{a}_2 + u_3\vec{a}_3 \quad (16)$$

$\vec{T}$  is called translational vector and  $u_1$ ,  $u_2$  and  $u_3$  are arbitrary integers.

Any lattice which looks identical from two arbitrary point  $\vec{r}$  and  $\vec{r}'$  and satisfy equations (15) and (16) are called primitive lattice and corresponding vectors are called primitive vectors. The parallelepiped formed by primitive axes  $\vec{a}_1$ ,  $\vec{a}_2$  and  $\vec{a}_3$  is called primitive lattice cell. It is a unit cell with minimum volume and has only one lattice point per cell. The basis attached with primitive cell is called primitive basis and the primitive basis has minimum number of atoms.

As basis consists of one or many number of atoms. The position of  $j^{\text{th}}$  atom in basis corresponding to lattice point of that basis taken as origin is given by

$$r_j = x_j \vec{a}_1 + y_j \vec{a}_2 + z_j \vec{a}_3 \quad (17)$$

Where  $0 \leq x_j, y_j, z_j \leq 1$ .

### Reciprocal lattice:

For primitive real lattice vectors  $\vec{a}_1, \vec{a}_2$  and  $\vec{a}_3$  the corresponding primitive reciprocal lattice vectors  $\vec{b}_1, \vec{b}_2$  and  $\vec{b}_3$  are defined as

$$\vec{b}_i = \frac{2\pi(\vec{a}_j \times \vec{a}_k)}{[\vec{a}_i \cdot (\vec{a}_j \times \vec{a}_k)]} \quad (18)$$

where, i, j and k =1,2 or 3

Analogous to real space, reciprocal lattice vector is

$$\vec{G} = v_1 \vec{b}_1 + v_2 \vec{b}_2 + v_3 \vec{b}_3 \quad (19)$$

Where  $v_1, v_2$  and  $v_3$  are integers and  $(v_1, v_2, v_3)$  are points in reciprocal-space.  $\vec{G}$  is a vector from origin in reciprocal to the reciprocal lattice point  $(v_1, v_2, v_3)$ . Each point  $(v_1, v_2, v_3)$  in reciprocal space completely describes the crystal and represents the orientation and spacing of that set of Miller planes in real space. The  $\vec{G}$  can be shown always perpendicular to the Miller plane  $(v_1, v_2, v_3)$  and the distance between the Miller plane is given by

$$d_{v_1 v_2 v_3} = \frac{1}{|\vec{G}_{v_1 v_2 v_3}|} \quad (20)$$

Clearly from Eqn (18) the scalar product of primitive lattice vectors of real and reciprocal spaces are



$$\vec{a}_i \cdot \vec{b}_j = 2\pi\delta_{ij} \quad (21)$$

Vectors in real space have dimensions of [length] and vectors in reciprocal lattice have the dimensions of [1/length] or reciprocal lattice is Fourier space associated with the crystal.

Diffraction condition: As wavelength of X-rays (or electron, neutron waves) and interplaner spacing of crystal planes are of same order, when X-ray (or electron, neutron waves) passes through crystal, diffraction may occur. Diffraction of X-ray, can occur if X-ray is elastically scattered by electron density surrounding atoms. X-rays are scattered by electron charge density of atom surrounding its nucleus, whereas electron are scattered by both the electron charge density as well as nucleus and neutron don't have charge, so they are only scattered by the nucleus of atom. During elastic scattering, the wave vector  $\vec{k}$  changes its direction and becomes  $\vec{k}'$ . However, the magnitude doesn't change during elastic scattering. For diffraction to occur, it can be shown that the change in wave vector

$$\vec{k}' - \vec{k} = \Delta\vec{k} = \vec{G} \quad (22)$$

Taking scalar product on both sides with primitive lattice vectors gives

$$\vec{a}_1 \cdot \Delta\vec{k} = 2\pi\nu_1, \quad \vec{a}_2 \cdot \Delta\vec{k} = 2\pi\nu_2, \quad \vec{a}_3 \cdot \Delta\vec{k} = 2\pi\nu_3 \quad (23)$$

This equation (23) are called Laue Equations and the condition (22) is called Laue condition.

Ewald's sphere:

Ewald's sphere is a useful construction for visualizing diffraction in reciprocal lattice. The wavevector  $\vec{k}$  is drawn in a direction of incident X-ray beam (monochromatic) from point A terminating at origin in reciprocal space. As diffraction is an elastic scattering of X-ray (or electron or neutron), the length of incident wavevector ( $\vec{k}$ ) and scattered wavevector ( $\vec{k}'$  and  $\vec{k}''$ ) in fig (14) are equal. So, a sphere is drawn with the radius equal to length of  $\vec{k}$ . The Laue condition (22) is satisfied by all the reciprocal points passing through the surface of sphere and diffraction due to corresponding Miller planes can be observed in detector.

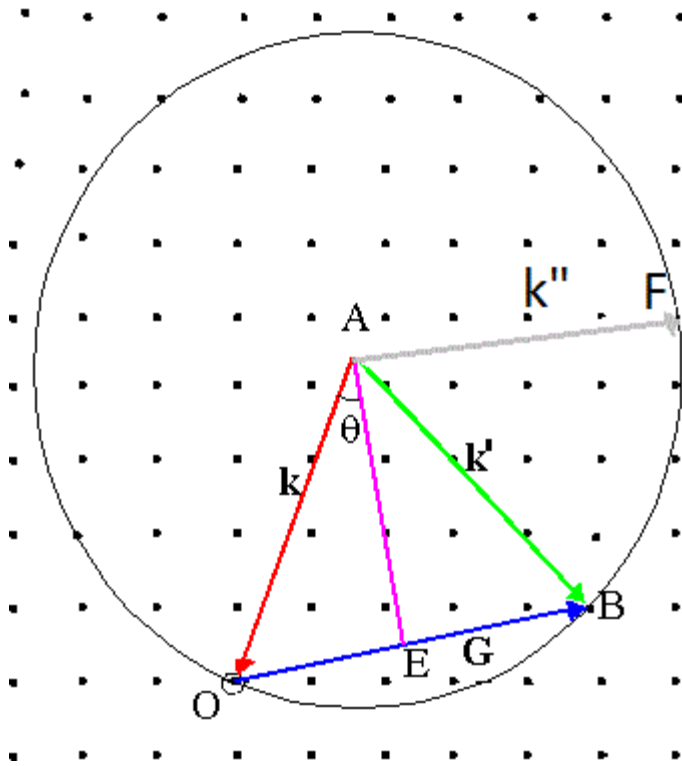


Figure 14: Ewald sphere constructed having radius  $|\vec{k}|$  in direction of incident beam and terminating at Origin O and passing through point B and F in reciprocal space. As the reflecting plane is perpendicular to  $\vec{G}$ , the diffracting plane for scattered wave AB contains plane AE. perpendicular to the plane of paper

The major difference between X-ray and electron diffraction is the radius of Ewald's sphere.

The wavelength of X-ray is much longer than electron, so wavevector for electron is much larger

than X-ray so that for electron waves Ewald's sphere looks almost flat and include more points in reciprocal lattice. The wavevector of 19.95 keV X-ray and 300 keV electrons are 10.1 and  $318.94 \text{ \AA}^{-1}$  respectively.

## 2.2 X-ray diffraction

### 2.2.1 Introduction

X-rays are a form of electromagnetic radiation having very short wavelength ranging from 0.01 to 10 nm, are produced by accelerating  $e^{-s}$ . The first systematic study of X-rays was done by Wilhelm Rontgen in 1895. Max von Laue, in 1912 demonstrated crystalline substances act as three dimensional diffraction gratings for X-ray as the wavelength of X-rays are of same order of spacing between planes of crystals. His experiment on copper sulphate crystals not only showed wave nature of X-rays but also showed that matter (crystals) are formed by periodic repetition of similar atoms or group of atoms. William Lawrence Bragg and William Henry Bragg used X-ray diffraction pattern of NaCl, KCl, ZnS and diamond to find out their crystal structure. William Lawrence Bragg explained his result by modelling crystal as a sets of parallel planes of atoms with constant separation 'd'. According to his theory, a constructive interference of scattering X-ray waves due to a set of parallel planes appears and forms a diffraction peak if the path difference in the reflection of X-ray radiation due to each sets of plane is equal to the integer number multiple of wavelength of incident X-ray, otherwise scattered waves destructively interfere and scattered intensity is minimum. The Bragg's law is

$$2d\sin\theta = n\lambda \quad (24)$$

where  $\theta$  is the glancing angle and  $\lambda$  is wavelength of incident X-ray. Bragg's law holds equally for electron or neutron diffraction. Experimentally, it is the angle between incident ray and reflected ray ( $2\theta$ ) which is measured. As the value of  $\sin\theta$  should be less or equal to unity, the wavelength of X-ray beam should be less than twice the separation between the plane ( $2d$ ).

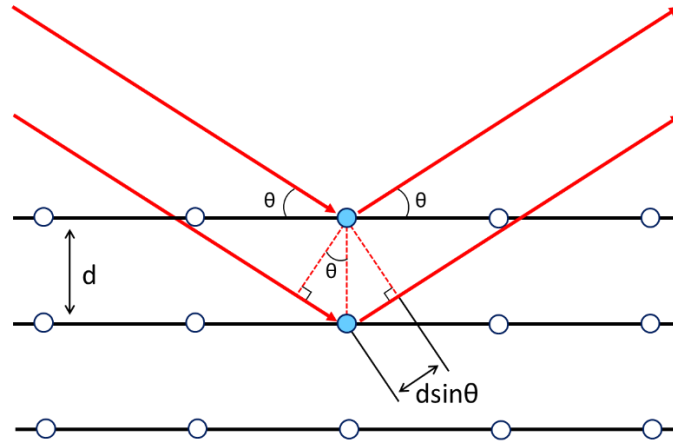


Figure 15: Bragg's law. The incident X-ray beams are incident at glancing angle  $\theta$  are reflected by  $e^-$  cloud of atoms at different parallel planes separated by the distance 'd'. The lower incident X-ray beam has to travel  $2d \sin\theta$  more distance than upper incident X-ray.

When a beam of X-ray is incident on a thin sample, most of the X-ray beam doesn't interact and travel in a straight line without any deflection and is called direct beam. The remaining part will scatter elastically or in-elastically. Inelastic scattering of X-ray beam will be discussed in X-ray absorption spectroscopy section. The elastically scattered X-ray beam follow Bragg's law, have same energy, wavelength but with different direction as of incident X-rays. For a single crystal and monochromatic X-ray these elastically scattered X-rays forms a dark diffraction spot (also called Bragg's spot) in photographic place, surrounding central dark spot due to direct X-ray beam, corresponding to reflecting plane. However, if the sample is polycrystalline or randomly oriented powder, diffracted waves that satisfy Bragg's condition lie on a cone at an angle  $2\theta$  with

incident beam, so instead of a diffraction spot a diffraction ring is observed in photographic plate or detector. The two dimensional diffraction pattern formed in detector can be reduced into one dimensional intensity profile by integrating intensity of each diffraction rings with respect to diffraction angle ( $2\theta$ ) as shown in fig (16).

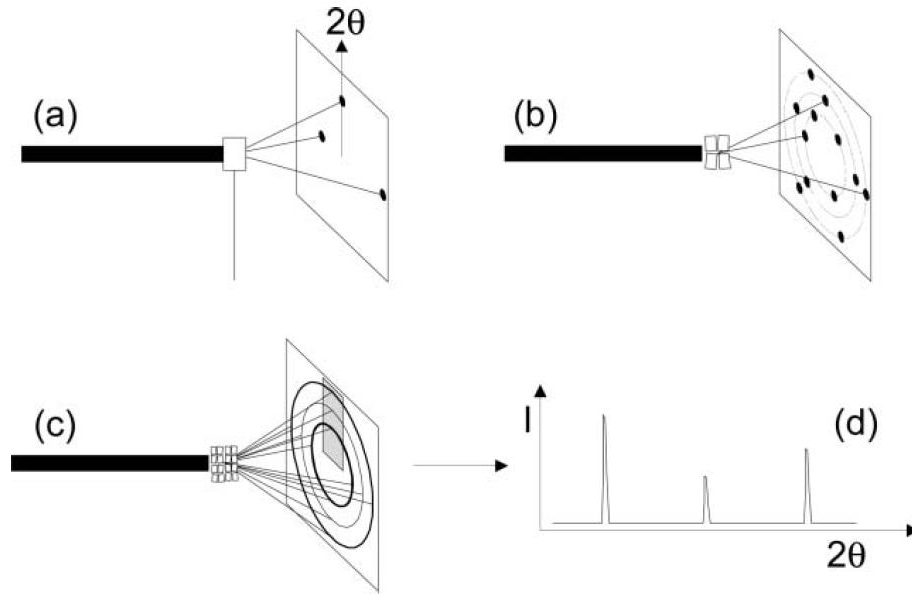


Figure 16 (a) Diffraction pattern of single oriented crystal (b) Diffraction pattern of four crystals at different orientations with respect to the incident beam (c) Diffraction rings formed by randomly oriented powdered crystals (d) Integrated intensity of diffraction rings of polycrystalline sample.

Currently, X-ray diffraction (XRD) is the primary analytical technique used for phase identification of a crystalline material and is used to obtain lattice cell parameter of crystals. Its use is not only limited to crystals; this technique is also used in amorphous material as well as in biological protein crystals.

### 2.2.2 Experimental setup:

In the most widely used X-ray diffraction setup, a X-ray tube source coupled with image plate detector are used. In X-ray tube thermally generated electrons are accelerated with about 50 keV and Cu is used as target. X-rays are produced when electrons are retarded by Cu target during collision. At 50 keV, some incident electrons have enough energy to knock out K-shell electrons of Cu atom, resulting transition of electrons from higher orbit to occupy vacant K-shell with emission of characteristic X-rays,  $K_{\alpha}$  and  $K_{\beta}$  lines. In most of the diffraction experiments,  $K_{\alpha}$  and  $K_{\beta}$  line of Cu are selected using monochromator. Our experiments were performed at Advanced Photon Source at Argonne national lab. Synchrotron based X-ray beam nearby Mo-K edge (19.95 keV, 19.999 keV and 20.0 keV) were used as incident X-ray beam on sample. Two single crystal of Si were used as monochromator and the beam was passed through the slit of 0.5-micron square. Samples were XRD experiments were prepared by crushing at mortar using pestle. Amorphous glass of 10 cm length and 1 mm internal diameter were filled with sample for measurements. Pilatus 100k Detector was used as a plane detector. Four different scans were taken for a measurement with the given energy. The first scan was scanning of background (empty glass capillary tube) with X-ray beam shutter closed, this is also called background dark scan. The second scan was again of background (empty glass capillary tube) with the X-ray shutter opened, this is also called background scan. The shutter is closed for a while so that current in detector dies. Then sample is allowed between X-ray beam and detector with X-ray beam shutter closed. This scan is called sample dark scan. Later shutter is opened and diffraction pattern is obtained in detector. In all 4 scans, a heavy metal beam stopper is used between sample and detector to stop central beam which is highly intense and can damage detector. For analysis,

background dark scan is subtracted from background scan to obtain net background scan, and sample dark scan is subtracted from sample scan to obtain net sample scan. Finally, net background scan is subtracted from net sample scan. The whole analysis is done using Nika macro in Igor Pro software. An example of Debye-Scherer ring diffraction pattern formed after processing is shown in fig (17) and its 1D reduced pattern is shown in fig (18). This whole set of scans are repeated 12 times. Each 2D data (Debye-Scherer ring diffraction pattern) data is reduced into 1D by sectorial line integration of intensity of diffraction rings again using Nika package [50]. Finally, average was taken from twelve 1D data. The width of peaks was measured using Multipeak Fitting 2 package of igorpro software.

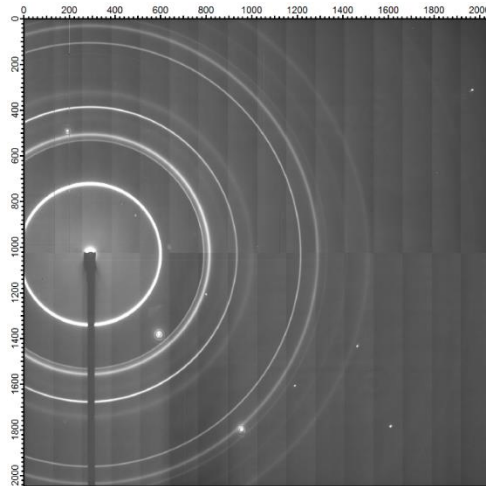


Figure 17: 2D raw diffraction pattern of graphite with beam stopper blocking direct X-ray beam. To obtain larger Debye-Scherer rings, the direct beam is not at the center of the detector.

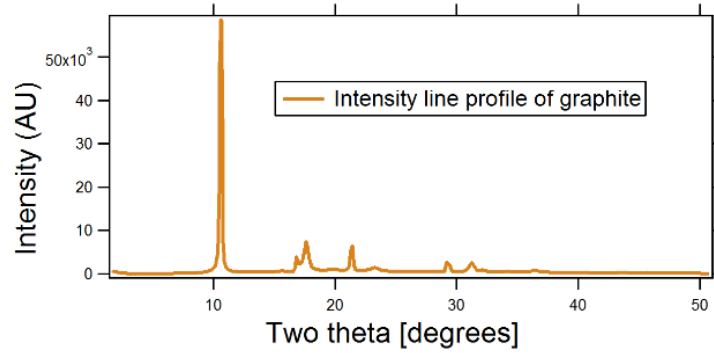


Figure 18: 1D integrated line intensity profile obtained from fig (17 ).

## 2.3 Electron Microscopy

### 2.3.1 Introduction

An electron moving with high velocity can be considered as a travelling wave and de Broglie's equation can be used to find out its wavelength. The de Broglie wavelength of a particle is given by

$$\lambda = \frac{h}{p} \quad (25)$$

Where  $p$  is the linear momentum of the moving particle and  $h$  is Plank's constant.

In TEM, kinetic energy gained by electron is due to applied accelerating potential,  $V$ . Thus loss in potential energy must be equal to gain in kinetic energy of electron.

$$eV = \frac{m_e v^2}{2} \quad (26)$$

The momentum  $p$  of electron is given by



$$p = m_e v \quad (27)$$

Substituting the value of 'v' from equation (26)

$$p = (2m_e eV)^{\frac{1}{2}} \quad (28)$$

The de Broglie equation for wavelength of non-relativistic electron becomes

$$\lambda_e = \frac{h}{(2m_e eV)^{\frac{1}{2}}} \quad (29)$$

For electron accelerated with more than 100 keV, the relativistic effect has to be taken into account and with relativistic correction, the de Broglie wavelength of electron is

$$\lambda_e = \frac{h}{\left[2m_e eV \left(1 + \frac{eV}{2m_e c^2}\right)\right]^{\frac{1}{2}}} \quad (30)$$

This equation (30) shows the inverse relationship between  $\lambda_e$  and V.

For an electron accelerated with 300 kV has a velocity of  $2.33 \times 10^8$  m/s and wavelength of  $1.97 \times 10^{-12}$  m. Due to its smaller wavelength compared to visible light, electron beam can be used for achieving atomic resolution imaging. However due to aberration, desired resolution is difficult to achieve.

As electrons interact strongly with specimen, the specimen prepared should be extremely thin.

For very thin specimen most of the  $e^-$  beam is transmitted without any deviation. This transmitted beam is called direct beam. The incident coherent beam can be forward or backward scattered.

Due to forward scattering through thin sample, we can obtain diffraction pattern (DP), image, X-

ray spectrum and electron energy-loss spectrum [EELS]. Back scattering can be used for imaging mode in scanning electron microscopy. Forward scattered beam consists of incoherent inelastic scattered electrons, coherent elastic scattered electrons and incoherent elastic forward scattered electrons. Back scattering beam consists of incoherent elastic back scattered electrons and scattering electrons from within specimen.

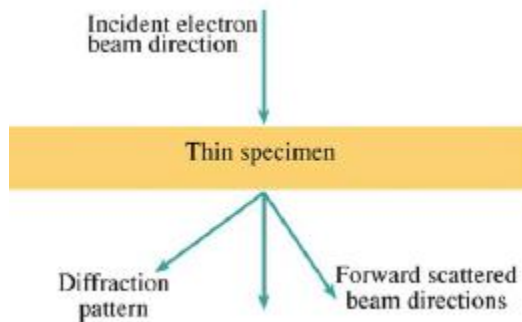


Figure 19: Different kind of electron scattering from thin specimen [51]

Elastically scattered electrons are the major source of contrast in TEM and intensity in DP.

Diffraction phenomenon can be explained by wave theory and it is controlled by angle of incidence of electron beam to the atomic planes in the specimen, spacing between the planes and interatomic distances within the planes.

Electron gun (Lithium hexaboride  $\text{LiB}_6$ ) produces thermal electrons which are accelerated by 300 kV. First condenser lens ( $C_1$ ) forms image of gun at crossover which acts as object for second condenser lens ( $C_2$ ).  $C_2$  also form point image at second crossover. Second crossover is at forward focal plane of upper objective lens or third condenser lens ( $C_3$ ).  $C_3$  lens form collimated

electron beam which are then incident on specimen. Suitable condenser aperture can be chosen to selected size or intensity of incident beam.

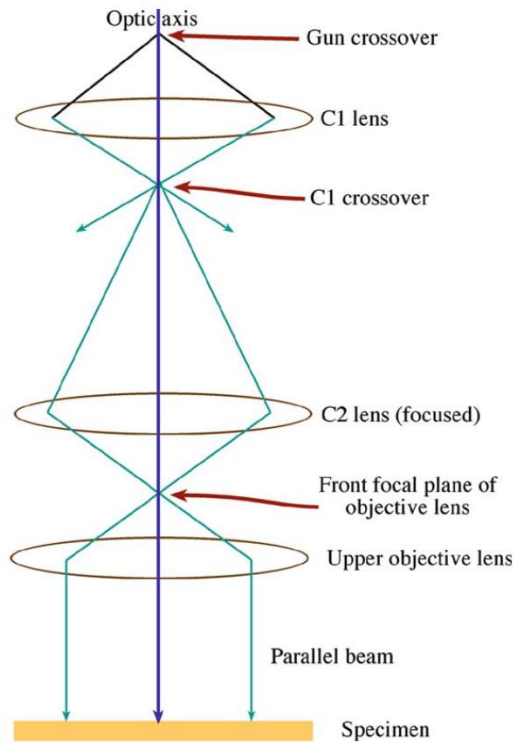


Figure 20: Parallel beam of electron formed by condenser lenses [51].

Electrons interact with both surrounding electron and proton of atom of specimen. During interaction, most of them moves without deflection while some of them are scattered. The scattered waves interfere and recombined by magnetic objective lens. Diffraction pattern is formed at back focal plane (BFP) and image is formed at image plane.

### 2.3.2 Diffraction mode:

In this mode imaging system lenses are adjusted in such a way that BFP of objective lens acts as the object plane for intermediate lens. Finally, DP is projected onto viewing screen or CCD camera by projector lens. Selected area diffraction is done by inserting aperture in one of the image plane of an imaging lens (objective lens). This creates a virtual aperture at the plane of

specimen. Condenser aperture  $C_2$  or  $C_3$  can also be inserted to converge the beam on specimen to obtain converging beam electron diffraction (CBED) pattern.

### **2.3.3 Image mode:**

In this mode, intermediate lenses are adjusted such that image plane of objective is object plane of intermediate lenses and finally image is projected on viewing screen or CCD camera.

During diffraction mode, objective aperture is removed and selected area aperture (SAA) is inserted. While in image mode SAA is removed. When objective aperture is not inserted, transmitted electron beam consists of direct as well as scattered electrons. In this configuration, final image is not very clear and at high magnification interference fringes can be seen in image (high resolution image). Inserting objective aperture selects mainly direct beam and restrict scattered beam. Selecting mainly direct beam is called bright field imaging. Also only scattered light can be selected by same aperture and this mode is called dark field imaging.

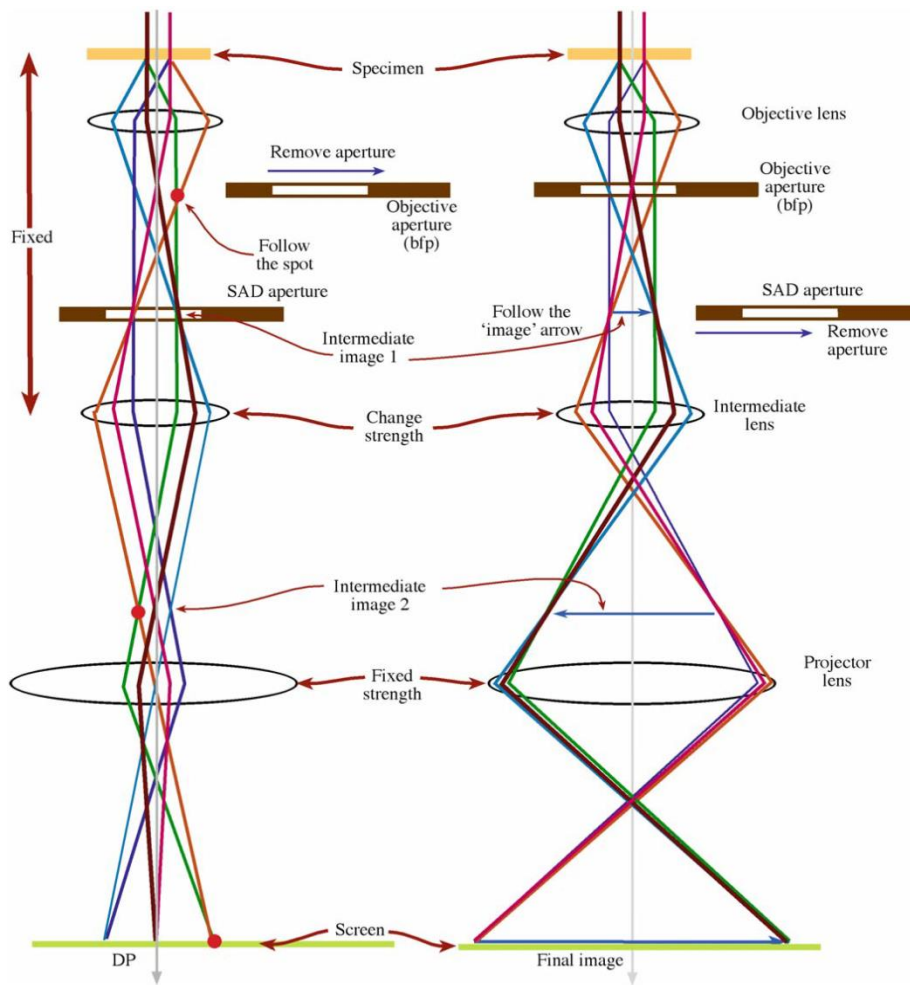


Figure 21: fig on left is DP mode and on right is image mode [51].

## 2.3.4 Energy-dispersive x-ray spectroscopy (EDX):

### 2.3.4.1 Introduction

It is most commonly employed technique used for elemental analysis of sample on the nanometer scale using analytical electron microscope. Sensitivity of this technique is comparatively better for elements with higher atomic number.

When fast moving electron traverses through thin sample, electron can be scattered elastically as well as inelastically. During inelastic interaction, energy and momentum of incident beam of electrons may be transferred to specimen, resulting in the production of two different kinds of X-rays.

Incident beam of electrons may eject inner shell electron (inner-core ionization of atom) of the specimen atoms. The vacant inner shell may be filled by transition of electron from higher orbit with the release of X-ray photons with the energy equal to the difference in the energies between two energy levels. Such produced X-rays are called **characteristic X-rays**. The energy of characteristic X-rays are characteristic of the atom and allows elemental analysis to be performed. However, the transition of electron from higher orbit to vacant shell can be accompanied by release of another electron from the same atom with energy equal to the difference in energies between two energy level. In this case, no photon will be released. This effect is called **Auger effect** and the released electron is called **Auger electron**. The energy of incident electron E has to be greater than ionization energy  $^3E_{nl}$  of a shell with quantum numbers n and l. The ionization cross section is given by formula

$$\sigma_{nl} = \frac{\pi e^4 Z_{nl}}{(4\pi\epsilon_0)^2 E E_{nl}} b_{nl} \ln\left(\frac{4E}{B_{nl}}\right) \quad (31)$$

Where  $b_{nl}$  and  $B_{nl}$  are numerical constants [ $b_k=0,35$  and  $B_k = 1.65 E_k$  for the K shell]

---

<sup>3</sup>  $E_{nl}$  is the energy difference to the first occupied state above the Fermi level

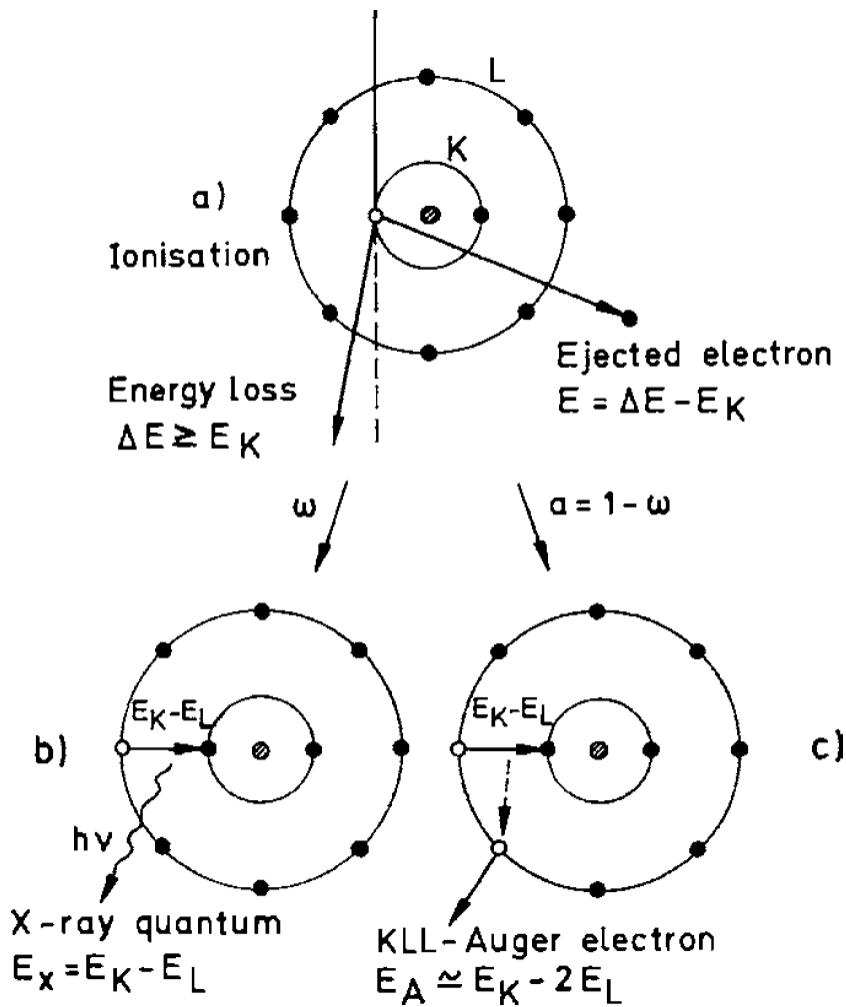


Figure 22 Schematic representation of (a) the ionization process, (b) x-ray emission, and (c) Auger-electron emission. [52]

Also incident electron beam might only be scattered by nucleus of the specimen atom. During this inelastic interaction with nucleus, electron is continuously accelerated in the Coulomb field of the nucleus and **continuum (Bremsstrahlung) X-rays** are produced [52].

Either lithium drifted silicon [Si(Li)] detectors or high purity intrinsic germanium detectors (HPGe, or IG in short) are used in modern TEM for counting X-ray photons which consists of both characteristic X-ray peaks along with continuum X-rays background. For elemental

analysis, background has to be properly removed. But characteristic peaks due to lower atomic number elements are buried inside continuum X-rays background, so the sensitivity of EDX is poor for lower atomic number elements.

#### **2.3.4.2 Experimental setup:**

TEM samples were prepared on Ni, Cu, Pt and Mo TEM grid. Single tilt, double tilt and Gatan tantalum-cup heating holder were used. Hitachi H9000NAR TEM operating at 300 keV was used. Column pressure was of the order of  $10^{-7}$  torr. CCD camera was used in TEM. SAED, bright field imaging, dark field imaging and EDX were performed.

## **2.4 Infrared Spectroscopy**

### **2.4.1 Introduction**

Infrared radiation belongs to electromagnetic radiation in the range of 700 nm- 1 mm in wavelength or  $14285 - 10 \text{ cm}^{-1}$  in wavenumber, having frequency higher than microwaves and lower than visible light. It can be further divided into far-IR  $400-10 \text{ cm}^{-1}$  ( $25-1000 \mu\text{m}$ ), mid-IR  $4000-400 \text{ cm}^{-1}$  ( $2.5-25 \mu\text{m}$ ) and near-IR  $14000-4000 \text{ cm}^{-1}$ .

Molecular vibration: A molecule with N atoms have  $3N$  degrees of freedom. It has 3 degrees of freedom for translational and another 3 degrees of freedom for rotation. So for a nonlinear molecule, there are  $3N-6$  modes of vibration (for nonlinear molecule) and  $3N-5$  for linear molecule. Each mode involves approximately harmonic displacements of the atoms from their



equilibrium positions. For each,  $i^{\text{th}}$  mode all the atoms vibrate at characteristic frequency,  $\nu_i$ .

Thus potential energy of this simple harmonic oscillator is given by the equation

$$V_{in} = h\nu_i(n_i + \frac{1}{2}) \quad (32)$$

Where  $h$  is Plank's constant,  $\nu_i$  is fundamental frequency of the  $i^{\text{th}}$  mode and  $n_i$  is the vibrational quantum number of the  $i^{\text{th}}$  mode ( $n_i = 0, 1, 2, \dots$ ).

Infrared spectra originate in transitions between two vibrational levels of the molecule in the electronic ground state and are usually observed as absorption spectra in mid infrared region. It should be noted that pure rotational, vibrational, and electronic spectra are usually observed in the microwave and far infrared, the infrared, and the visible and ultraviolet regions, respectively [53]. If the vibrational modes were strictly harmonic, no transition other than  $\Delta n_i = \pm 1$  would be allowed. However, the system behaves as anharmonic oscillator. So, overtone ( $\Delta n_i = \pm 2, 3, \dots$ ) and combination ( $\Delta n_i = 1; \Delta n_j = 1$ , where  $j$  represents a different mode) commonly appears weakly along with fundamental transitions. Also if the sample is in gaseous state, the rotational transitions are superimposed along with vibrational transitions making absorption spectra more complicated.

IR spectroscopy is used to obtain chemical information about the sample. Usually mid infrared ( $4000\text{cm}^{-1}$ - $400\text{cm}^{-1}$ ) is used for this purpose as frequency of vibration of molecule lie within this range. All the materials consist of atoms or radical and they vibrate with their natural frequency. If the beam of incident electromagnetic radiation is equal to or is the integral number multiple of natural frequency of vibration, it may be absorbed by vibrating molecule. IR radiation is only absorbed if the electric dipole moment of the vibrating molecule is changing with vibration. If electric dipole moment changes with vibration, such mode of vibration is called "IR active". It

should be noted that all modes of vibrations are not IR active. As an example, when a homonuclear diatomic molecule such as O<sub>2</sub>, N<sub>2</sub> or H<sub>2</sub> stretches, there is no change in electric dipole moment, so this stretching mode is “Infrared inactive” but stretching mode of heteronuclear molecule such as CO or NO is “Infrared active”. Usually, group theory is applied for identification of IR active modes.

IR radiation can enforce two different kinds of vibrations (stretching and bending). Usually stretching needs more energy so it absorbs IR at higher frequency (4000 cm<sup>-1</sup>-1500 cm<sup>-1</sup>) whereas bending takes place at lower frequency (below 1500 cm<sup>-1</sup>) and this region is called finger print region as spectrum in the region is complex but unique of the sample.

FTIR spectrometer consists of broadband IR source (Globar, synchrotron), Michelson interferometer, sample compartment and detector (DTGS, MCT or FPA). Light from source is made collimated and enters interferometer. Interferometer consists of beamsplitter which splits beam into two different mirrors and among those mirrors one of them is moving. IR beam reflected from those mirrors are allowed to pass through sample compartment (where some of them might get absorbed) and finally enters detector.

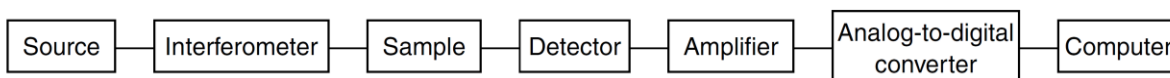


Figure 23: Basic components of FTIR spectrometer

Detector measures the intensity of IR light and makes interferogram. Interferogram is a sum of waves from different frequencies with respect to the mirror positions. It has information in time domain which is later transformed into frequency domain by fast Fourier transform (FFT).

Spectrums are obtained without sample (Background) and with sample. The ratio of sample to background gives transmittance spectrum which can be converted into absorbance by

$$A = -\log \frac{I_0}{I} \quad (33)$$

Where  $I_0$  = Intensity at detector without sample

$I$  = Intensity at detector with sample

Here we have assumed that sample doesn't reflect and scatter.

Absorbance is usually used instead of transmittance because it can be related with absorptivity ( $M^{-1} cm^{-1}$ ) which is the unique property of the sample.

Absorbance = Absorptivity ( $M^{-1}cm^{-1}$ ) \* Pathlength (cm) \* Concentration (M)

#### 2.4.2 Sources:

The most common mid-infrared source used in FT-IR spectrometers is a resistively heated silicon carbide rod which is also called Globar. It is operated around 1300K. Synchrotron based source IR is also used when high intensity beam and good signal to noise ratio (SNR) is required.

#### 2.4.3 Detectors:

Thermal or quantum detectors are mainly used for IR measurement.

Deuterated triglycine sulphate (DTGS) detector: It is a very sensitive thermal (pyroelectric) detector operated at room temperature for mid-infrared range measurements that employs

temperature-sensitive ferroelectric crystals of deuterated triglycine sulphate. When IR radiation falls on DTGS detector, its temperature changes and hence the polarizability of the crystals changes. Change in polarization generates charge which is detected by two parallel electrodes [Royal society of Chemistry]. The deuterated form of the crystals is used because of their higher Curie point ( $T_c \approx 49^\circ\text{C}$  higher by  $10^\circ\text{C}$ ). If the temperature of a pyroelectric detector exceeds its Curie temperature, its response drops to zero and the element must be repolarized before it can be reused [54]. The range of this detector is from  $400 - 8000 \text{ cm}^{-1}$ .

Sample for DTGS detector are usually made by mixing the finely crushed sample (2%) with KBr powder into pellets of 2mm diameter and about 0.1-0.3 mm thick.

Mercury cadmium telluride (MCT or HgCdTe): MCT is a highly sensitive quantum detector which is made from alloy of semimetal HgTe and semiconductor CdTe (bandgap 1.5eV at room temperature). So the alloy has tunable bandgap between 0 and 1.5eV. When Infrared photon is incident on MCT, it may kick electron from valence band to the conduction band. This ejected electron can be collected by collected by readout integrated circuits (ROIC) and transformed into an electric signal. The main drawback of MCT detector is it need to be cooled to liquid nitrogen (LN2) temperature (77K), to reduce noise due to thermally excited current carriers. But it has higher speed of detection(scan) and is more sensitive than thermal detectors. Its range is  $650 - 8000 \text{ cm}^{-1}$ .

Samples for MCT detector: MCT detector are usually attached with IR microscope. So the microscope is capable of detecting IR signals from sample of few microns in surface area and nanometers in thickness. So the sample can be placed on KBr pellet, diamond window or TEM grid of 300 mesh.

Bruker Hyperion 3000 microscope was used for IR spectroscopy. Samples were prepared on TEM grids, diamond windows and KBr pellet.

## 2.5 X-ray Absorption Spectroscopy(XAS)

XAS measurement is a technique used to characterize structure of crystalline, amorphous and even liquid states of materials. XAS can be further divided into X-ray absorption at near edge structure (XANES) and Extended X-ray absorption fine structure (EXAFS).

### 2.5.1 Principles of XAS:

When x-ray photons are incident on any material, they are absorbed by the material obeying Beer Lambert's law

$$I = I_0 e^{-\mu t} \quad (34)$$

Where  $I_0$  is intensity of incident x-ray on sample,  $t$  is the sample thickness,  $I$  is the intensity of transmitted x-ray through sample and  $\mu$  is the linear absorption coefficient of material depending on the types of atoms and the density ( $\rho$ ) of material.

For most of the x-ray energies,  $\mu$  is the smooth function of energy

$$\mu \approx \frac{\rho Z^4}{AE^3} \quad (35)$$

Where  $\rho$  is density of material,  $Z$  is atomic number and  $A$  is atomic mass and  $E$  is the energy of the incident x-ray.

This equation shows absorption coefficient for the given material decreases with the increase in energy (decrease in wavelength) of x-ray. That means X-rays with higher energy have higher penetrating power. Also refractive index for x-rays is lower than unity for any material [55]. X-ray absorption coefficient  $\sigma_a$  of an atom (or molecule) is defined as the number of electrons excited per unit time divided by the number of incident photons per unit time per unit area and it is related to absorption cross-section by the relation

$$\mu = \left( \frac{\rho_m N_A}{A} \right) \sigma_a \quad (36)$$

However, when incident x-ray energy is equal to binding energy of a core-electron, there is a sharp rise in absorption due to the promotion of core level electron to continuum state. The incident x-ray photon may eject core-electron if the energy of photon is equal or greater than binding energy of core electron. Thus, the energies of the absorbed radiation at these edges correspond to the binding energies of electron in the K, L, M .... shells of the absorbing elements and the absorption edges are labeled in the order of increasing energy, K, L and so on. This quantum mechanical phenomenon is called Photoelectric effect. As core electron binding energy is unique for every element, the absorption edge energy is also unique, so XAS is element specific technique. XAS measurement is the measurement of variation of absorption coefficient of material around absorption edge.

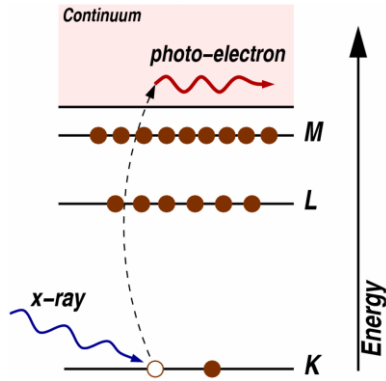


Figure 24: The photo electric effect, in which x-ray is absorbed and a core level electron is promoted out of the atom

There is single K edge but 3 distinct L edges,  $L_1$ ,  $L_2$  and  $L_3$  in decreasing order. Splitting of L shell is due to removal of degeneracy in L shell. Degeneracy of L shell is removed by (i) screening of nuclear charge by K electrons resulting lowering of 2s electrons compared to 2p electrons<sup>4</sup> (ii) spin orbit coupling resulting into difference in energy between  $2p_{1/2}$ , and  $2p_{3/2}$  orbitals.  $L_1$ ,  $L_2$  and  $L_3$  corresponds to 2s (2 electrons),  $2p_{1/2}$  (2 electrons) and  $2p_{3/2}$  (4 electrons) orbitals. Beside the photoelectric absorption<sup>5</sup>, x-rays can also be absorbed due to Thomson and Compton scattering.

If  $\hbar\omega$  be the energy of incoming x-ray photon and  $E_b$  be the binding energy of ejected electron, the final energy  $E_f$  of the photoelectron (ejected electron) is

$$E_f = \hbar\omega - E_b \quad (37)$$

<sup>4</sup> The self-consistent one-electron potential drops faster than the pure coulomb potential

<sup>5</sup> Photoelectric absorption is the dominant absorption of X-rays at photon energy less than  $m_e c^2 = 511$  keV and it is sometimes also called true absorption.

The photoelectron interacts with the neighboring atoms as a wave with momentum  $\hbar k$  and the wavevector is given by

$$k = \frac{\sqrt{2m_e(\hbar\omega - E_b)}}{\hbar} \quad (38)$$

The transition rate  $W$ , i.e. the probability of a transition to occur per unit time is calculated using Fermi's golden rule [56] [57].

$$W = \frac{2\pi}{\hbar} \sum_f |\langle f | \mathcal{H}_I | i \rangle|^2 \delta(E_f - E_i - \hbar\omega) \quad (39)$$

Where  $|i\rangle$  and  $|f\rangle$  are initial and final states,  $\mathcal{H}_I$  is interaction Hamiltonian and  $\langle f | \mathcal{H}_I | i \rangle$  is matrix element of interaction Hamiltonian. It can be shown that absorption cross-section is

$$\sigma_a = \left(\frac{2\pi}{\hbar c}\right) \left(\frac{V^2}{4\pi^3}\right) \int |\langle f | \mathcal{H}_I | i \rangle|^2 \delta(\mathcal{E}_{pe} - (\mathcal{E} - \mathcal{E}_b)) q^2 \sin\theta dq d\theta d\phi \quad (40)$$

Where,  $\mathcal{E}_{pe}$  = K.E of photoelectron =  $\hbar^2 q^2 / 2m$ ,  $\mathcal{E}$  = energy of incident x-ray photon =  $\hbar\omega$

and  $\mathcal{E}_b$  = binding energy of core shell electron

i.e. 
$$\sigma_a \propto |\langle f | \mathcal{H}_I | i \rangle|^2$$

Hence, linear absorption coefficient is

$$\mu \propto |\langle f | \mathcal{H}_I | i \rangle|^2$$

The neighboring atoms can be considered as a point scatters which scatter back outgoing photoelectron wave. The interference of multiple backscattered waves with outgoing photoelectron wave give rise to a modulation of the x-ray absorption coefficient  $\mu(E)$  after the



edge, also called fine structure. In XAS measurement  $\mu(E)$  is directly measured using equation (34).

The region before edge is called pre-edge region where as the fine structure at near edge region is called XANES (X-ray absorption near edge structure) and in the extended region is called EXAFS (Extended X-ray Absorption Fine Structure), which are shown in figure (26). XANES contains information about average oxidation state, local coordination environment (valence) and density of states of the absorber, as well as qualitative structural information [58]. XANES are difficult for interpretation using theory so they are compared with simulations. EXAFS provides quantitative information on average bond length between absorbing atom with its neighboring atoms, coordination number, type of the neighboring atoms and mean square disorder of neighboring atoms [58].

### 2.5.2 Theory for EXAFS:

For EXAFS analysis, a dimensionless quantity is defined from  $\mu(E)$  as

$$\chi(q(E)) = \frac{\mu(E) - \mu_0(E)}{\mu_0(E)} \quad (41)$$

$$\text{or, } \mu(E) = \mu_0(E)[1 + \chi(q)]$$

Where  $q(E)$  is the length of the wavevector of photoelectron,  $\mu_0(E)$  is the absorption coefficient of the isolated atom if EXAFS were absent and  $\mu(E)$  is the absorption coefficient of material of

---

<sup>6</sup> Thickness 't' in equation (34) is constant for the given sample for any energy of X-ray and can be removed by proper normalization

interest.  $\mu_0(E)$  is obtained beyond edge region by extrapolation of curve at pre-edge region.

The goal of EXAFS is to find out radii of neighboring shells and their occupation number from the atom ejecting photoelectron. The matrix element of the interaction Hamiltonian,  $\langle f | \mathcal{H} | i \rangle$  is fundamental, so it doesn't depend on details of neighboring atoms. The initial state  $|i\rangle$  describes the innermost electrons of absorbing atom, so it also doesn't depend much of the environment of the atom. It is assumed that EXAFS oscillation is due to small change in final state  $|f_0\rangle$  of the free atom due to neighbouring atoms  $|\Delta f\rangle$ .

$$|f\rangle = |f + \Delta f_0\rangle \quad (42)$$

The modulus of square of the matrix element is

$$\begin{aligned} |\langle f_0 + \Delta f | \mathcal{H}_I | i \rangle|^2 &= [\langle f_0 | \mathcal{H}_I | i \rangle + \langle \Delta f | \mathcal{H}_I | i \rangle][\langle f_0 | \mathcal{H}_I | i \rangle + \langle \Delta f | \mathcal{H}_I | i \rangle]^* \\ &\approx |\langle f_0 | \mathcal{H}_I | i \rangle|^2 + \{\langle f_0 | \mathcal{H}_I | i \rangle^* \langle \Delta f | \mathcal{H}_I | i \rangle + c. c\} \\ &= |\langle f_0 | \mathcal{H}_I | i \rangle|^2 \left( 1 + \left\{ \frac{\langle f_0 | \mathcal{H}_I | i \rangle^* \langle \Delta f | \mathcal{H}_I | i \rangle}{|\langle f_0 | \mathcal{H}_I | i \rangle|^2} + c. c \right\} \right) \end{aligned}$$

Where c.c is complex conjugate. Comparison with equation (41) the first term give absorption coefficient of free atom,  $\mu_0(E)$  so the second term must give EXAFS oscillation and

$$\chi(q) \propto \langle \Delta f | \mathcal{H}_I | i \rangle$$

The initial wavefunction of the electron is strongly localized within the absorbing atom, so it can be approximated by delta function. The change in photoelectron wavefunction due to the neighboring atoms can be denoted by  $\psi_{\text{back.sc.}}(\mathbf{r})$ .

$$\chi(q) \propto \int \psi_{\text{back.sc.}}(\mathbf{r}) \exp(i\mathbf{k} \cdot \mathbf{r}) \delta(\mathbf{r}) d\mathbf{r} = \psi_{\text{back.sc.}}(0)$$

For finding  $\psi_{\text{back.sc.}}$  from only one neighboring atom at a distance  $R$  from the absorbing atom at the origin, we assume that the absorbing atom emit outgoing spherical wave  $(\frac{e^{iqr}}{r})$ . The scattering atom will scatter incoming spherical wave into another spherical wave with amplitude proportional to the amplitude of the incident wave to a scattering length  $t(q)$ . Also neglecting electrostatic potential between the electron and the ions of the lattice, assuming phase shift in wavefunction by  $\delta(q)$ , where  $\delta(q)$  is the sum of phase shift produced by absorbing atom,  $\delta_a(q)$  and from back scattering atoms,  $\delta_{\text{back.sc.}}(q)$ .

$$\begin{aligned} \psi_{\text{back.sc.}}(0) &= \frac{t(q)(e^{i(2qR+\delta)} + c.c.)}{qR^2} \\ &\propto t(q)\left(\frac{\sin(2qR+\delta)}{qR^2}\right) \end{aligned}$$

The factor of  $q$  is included in denominator to keep  $\psi_{\text{back.sc.}}$  dimensionless. The neighboring atom at finite temperature vibrates about its mean position. If the r.m.s value of the displacement parallel to  $\mathbf{q}$  is  $\sigma$ , the amplitude of the back scattered wave is reduced by the Debye-Waller factor of  $e^{-\frac{Q^2\sigma^2}{2}}$ . For a scattering vector of  $Q=2q \sin 90^\circ = 2q$ .

Thus  $\psi_{\text{back.sc.}}(0) \propto \frac{t(q) \sin(2qR+\delta(q))}{qR^2} e^{-2(q\sigma)^2}$ . Also the hole created due to ejection of photoelectron is filled after a finite time, so the back scattered wave might not find atom at the same initial state with finite probability. Again, the photoelectron wave may be

scattered by other electrons in its round trip, so phenomenological mean-free pathlength  $\Lambda$  is introduced

$$\psi_{back.sc.}(0) = \frac{t(q) \sin(2qR + \delta(q))}{qR^2} e^{-(q\sigma)^2} e^{-\frac{2R}{\Lambda}}$$

If the absorbing atom is surrounded by shells of neighbor atoms, with  $N_j$  atoms in the  $j^{\text{th}}$  shell at a distance  $R_j$ . Finally

$$q\chi(q) \propto \sum_i N_j \left( \frac{t_j(q) \sin(2qR_j + \delta_j(q))}{(R_j^2)} \right) e^{-2(q\sigma_j)^2} e^{-\frac{2R_j}{\Lambda}} \quad (43)$$

### 2.5.3 Experimental setup:

Sample for XAS measurement can be in powdered form or if it is metal it can be in thin foil form. If the sample is powdered, it is either spread in kapton tape or filled in amorphous capillary glass tube. The XAS measurement requires highly intense continuous x-ray over a wide energy range which can be provided only by synchrotron radiation source. In Synchrotron, electrons are injected and accelerated around in a storage ring. These relativistic electrons are suddenly retarded using magnets and according to classical electrodynamics, X-ray photons are released [59] tangential to the ring.

Before taking measurement of unknown sample, at least some information should be known about the absorbing element in unknown sample. X-ray with the energy in the range just below and above core electron binding energy is used for measurement.

Polychromatic X-ray is allowed to pass through a double crystal monochromator.

Monochromator is usually made up of single crystal of Si. It works on the principle of

Bragg's law. For the given angle of incidence, it only reflects X-ray of particular wavelength or integer number multiple of the wavelength. Optics are arranged in such a way that higher order reflection are removed and only X-ray of selected wavelength is allowed to incident on sample. Ionization chambers are used for measuring intensities of X-ray. In figure 25 IC1 is the ionization chamber detector measuring intensity  $I_0$  incident on sample, IC2 is another detector used to measured intensity of transmitted X-ray. There is a fluorescence detector (optional) positioned as shown in diagram (25) if the X-ray causes any fluorescence in sample. For alignment of XAS graph obtained from unknown sample, a reference sample is placed between detectors IC2 and IC3. Reference sample is chosen in such a way that the absorbing element in unknown and Reference sample are same. For example, if  $\text{Mo}_2\text{C}$ ,  $\text{MoO}_3$  or Mo compound is unknown sample, Mo foil is usually used as reference sample.

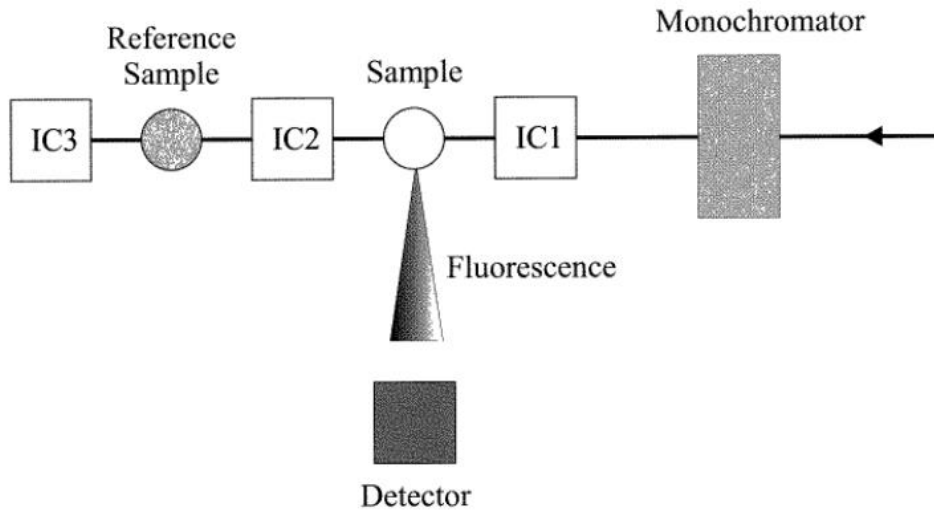


Figure 25: XAS experimental setup. IC1, IC2 and IC3 are ion chamber detectors used to detect intensity of X-ray photon incident on sample, transmitted from sample (or incident on reference sample) and transmitted from reference sample respectively. A double crystal monochromator is used. "Detector" is the detector for measuring fluorescence

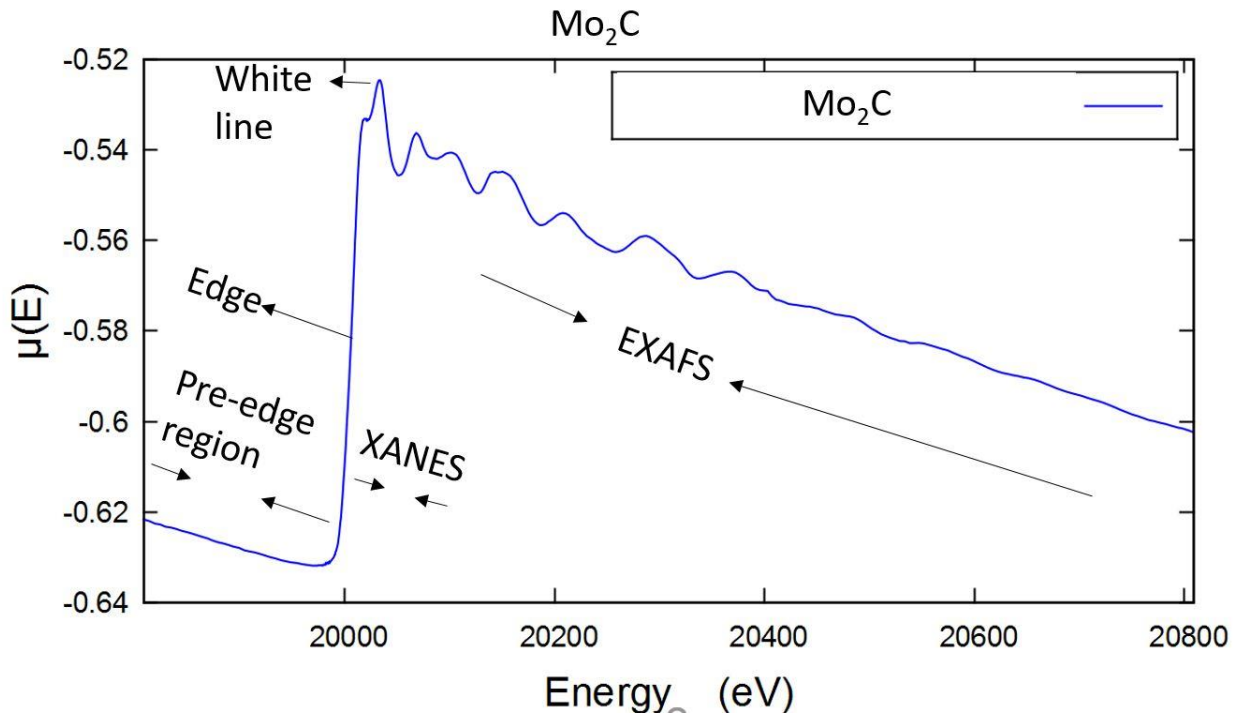


Figure 26: Raw data of X-ray absorption coefficient (times thickness) vs Energy showing decrease in absorption coefficient with increase in X-ray energy but at Mo K -edge there is drastic increase in coefficient and it oscillates after that resulting XANES and EXAFS region

After obtaining, intensity of x-ray beams incident and transmitted from sample and reference sample, graph is plotted for coefficient of linear absorption,  $\mu(E)$  vs Energy, E. Coefficient of linear absorption is obtained using Lambert Beer law (34)

$$\mu(E)t = \ln\left(\frac{I_0}{I}\right) \quad (44)$$

The figure (26) shows graph of  $\mu(E)$  times thickness (t) vs energy and so does equation (44). For a particular region in the sample thickness remains constant. The effect of thickness can be removed by proper normalization.

For normalization, pre-edge region is regressed about the edge energy,  $E_0$  between  $E_0-300$  eV and  $E_0-150$  eV, then the linear line extrapolated throughout the whole energy range (denoted by green line in fig (27)). The pre-edge line is subtracted from the whole data (blue line) so that pre-edge region of the data lies flat along X-axis. The post-edge data is also regressed with parabolic line about two point about  $E_0+150$  eV and  $E_0 + 740$  eV and extrapolated over whole energy range denoted by purple line in fig (27). The edge step  $\Delta\mu_0(E_0)$ , is calculated as the difference between post-edge line and pre-edge line at  $E_0$ . Finally, normalization is done by dividing whole data by the edge step  $\Delta\mu_0(E_0)$ .

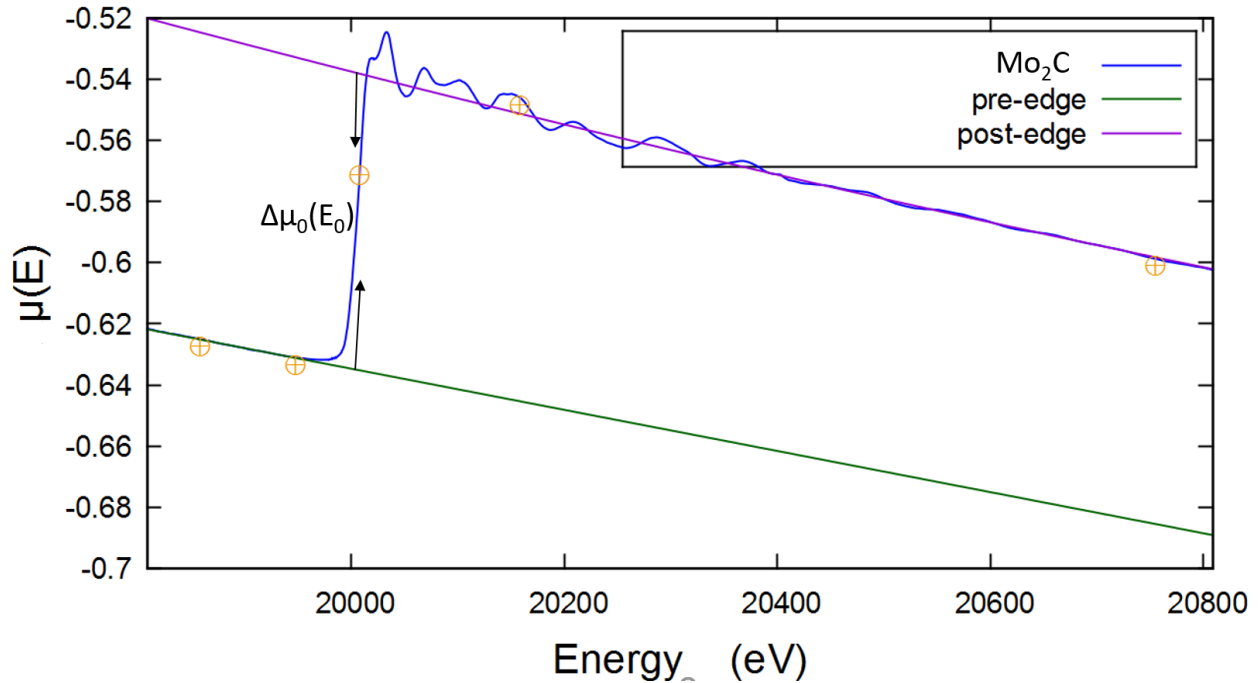


Figure 27:  $\mu(E)$  vs Energy graph for  $\text{Mo}_2\text{C}$ . Pre-edge and post-edge fitting linear and cubical lines are drawn respectively for normalization.

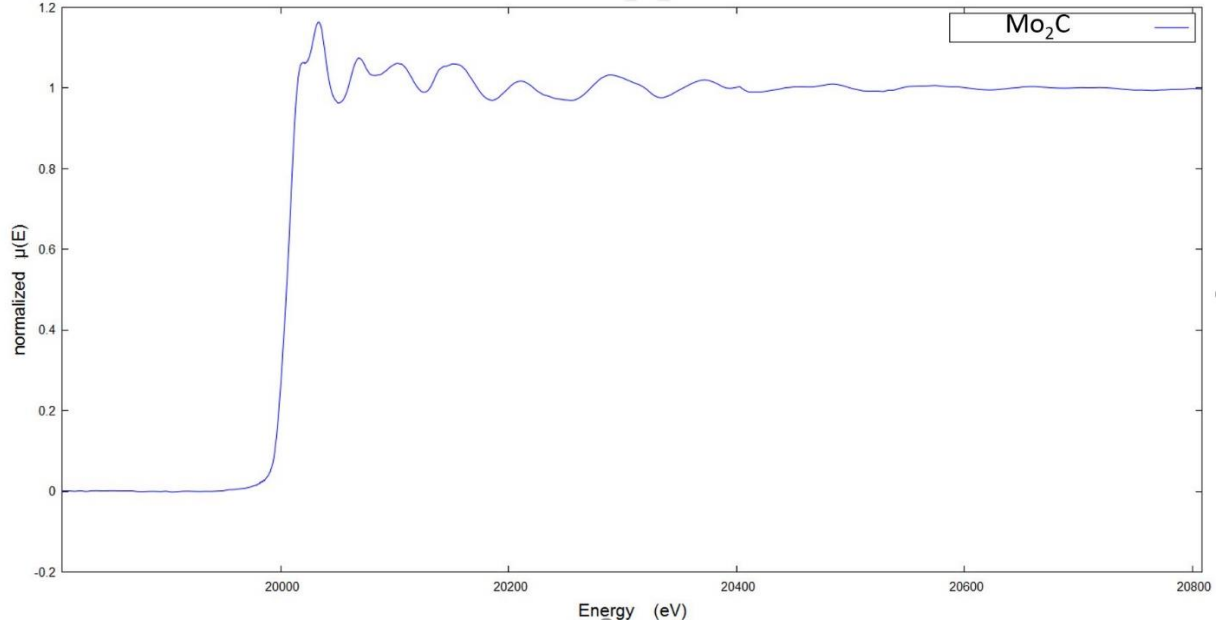


Figure 28:  $\mu(E)$  vs Energy graph of  $\text{Mo}_2\text{C}$  after normalization.

The equation used for calculating  $\chi(q)$  is slightly modified from equation (41) because  $\mu_0(E)$  factor in denominator used in the equation is not well behaved. Its measured value can be negative or positive depending upon detector and amplifier settings. So it is replaced by edge step  $\Delta\mu_0(E_0)$  for experimental purpose.

$$\chi(q(E)) = \frac{\mu(E) - \mu_0(E)}{\Delta\mu_0(E_0)} \quad (45)$$

The normalized data is ready for XANES and EXAFS analysis. It is independent of thickness and distribution of concentration of sample. The data can be used for Linear combination fitting in which XANES (or derivative  $\mu(E)$  or  $\chi(k)$ ) spectra of unknown sample is fitted with linear combination of XANES ((or derivative  $\mu(E)$  or  $\chi(k)$ ) of standard samples.

Eventually,  $\chi(q)$  or  $\chi(k)$  is Fourier transformed to obtain  $\chi(R)$ . During analysis,  $\chi(k)$  is



usually weighted with  $k$ ,  $k^2$  or  $k^3$  depending upon the requirement in data.

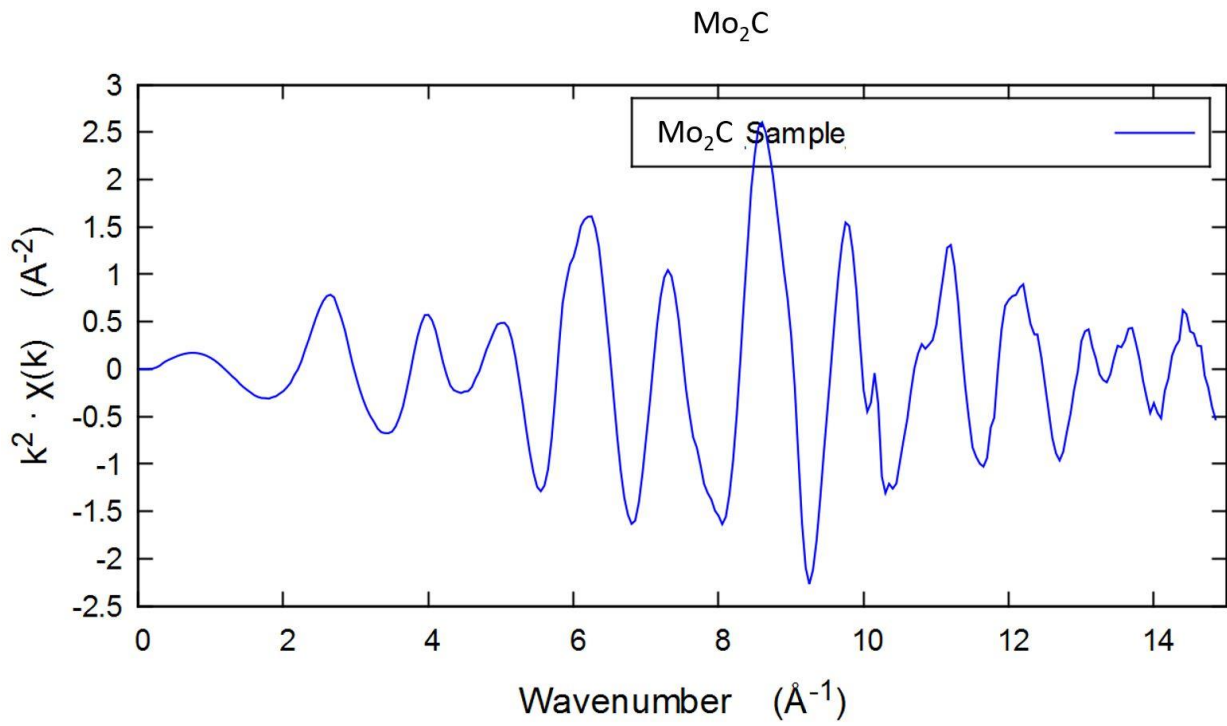


Figure 29:  $\chi(k)$  weighted by  $k^2$  of  $\text{Mo}_2\text{C}$  obtained from normalized  $\mu(E)$  from figure 28 using equation 45

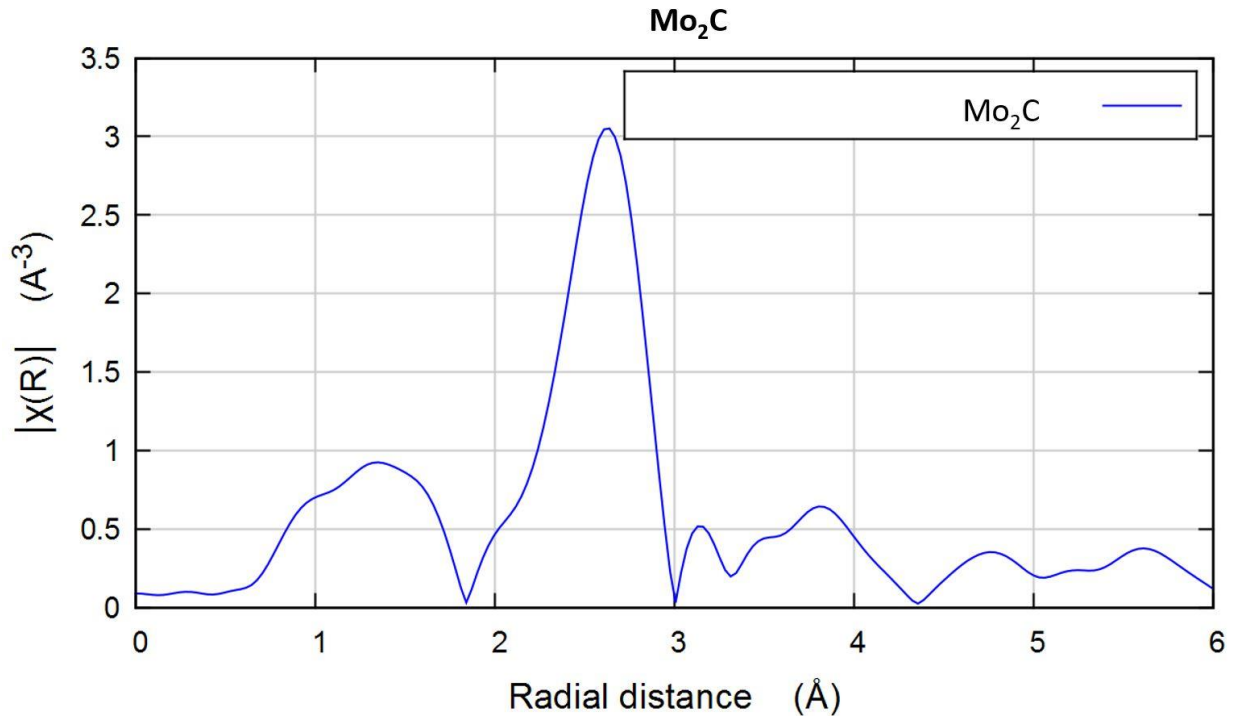


Figure 30: Fourier transform of  $k^2 \cdot \chi(k)$  of Mo<sub>2</sub>C from figure 29

Further, EXAFS analysis is performed using Athena software to fit equation (43) 29

## 2.6 UV-Vis Spectroscopy

### 2.6.1 Introduction

Electromagnetic spectrum includes radiation of very short wavelength from cosmic ray to very long wavelength radio waves. Ultraviolet (UV) and visible radiation comprises only a small part of it.

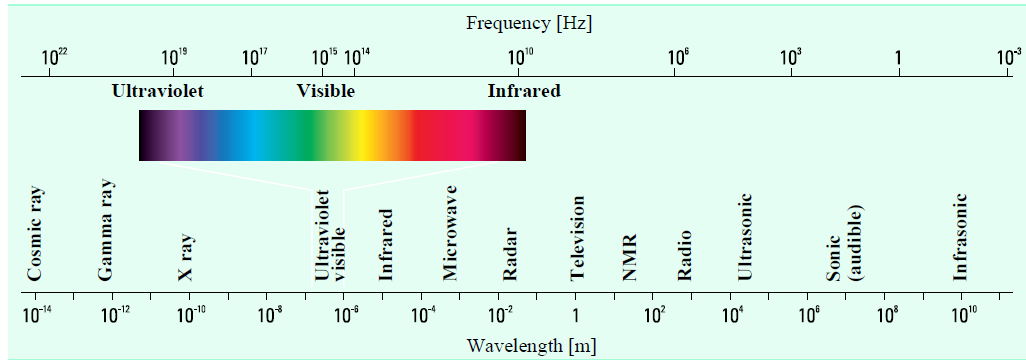


Figure 31: The electromagnetic spectrum [60]

Electromagnetic radiation can interact with matter in a different ways including reflection, transmission, scattering, fluorescence, phosphorescence and absorbance etc. During absorption, matter stores it in a form of potential energy, which is a sum of its electronic, vibrational and rotational energies.

Atoms or molecules present in material have discrete electronic energy states  $E_i$ . When the electromagnetic radiation of some matching frequency  $\nu$  is incident on an atom at ground state, electron at ground state  $E_1$  jumps to some higher energy state  $E_2$  such that

$$E = E_2 - E_1 = h\nu = h\left(\frac{c}{\lambda}\right) = hc\bar{\nu} \quad (46)$$

where  $h$  is Planck's constant ( $6.626 \times 10^{-34}$  J s) and  $\nu = c/\lambda$ .  $\lambda$  is wavelength of incident electromagnetic radiation and  $\bar{\nu}$  is wavenumber which is usually measured in  $\text{cm}^{-1}$  or  $\text{nm}^{-1}$ .

Atom in its excited state ( $E_2$ ) is not stable, so usually it emits electromagnetic radiation of exactly same frequency  $\nu$  by the transition of  $e^-$  in excited state  $E_2$  to  $E_1$ . If the absorption is in UV region, molecules absorbs energy and  $e^-$  jumps to higher energy state with matching energy.

The electrons in excited state might come down to ground state by losing energy in the form of heat or energy is exchanged to vibrational and rotational energy without radiation less process.

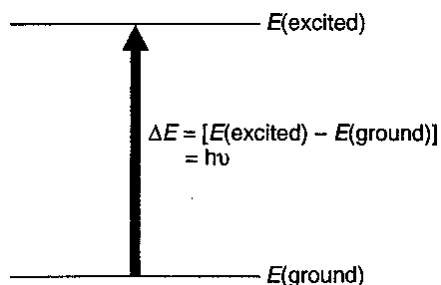


Figure 32: The excitation process

In case of absorption of ultraviolet or visible radiation by a molecule, its electron is promoted from an occupied orbital to an unoccupied orbital of greater potential. Usually, the most probable transition is from the highest occupied molecular orbital (HOMO) to the lowest unoccupied molecular orbital (LUMO). The lowest-energy occupied molecular orbitals are the  $\sigma$ -orbitals corresponding to  $\sigma$ -bonding.  $\sigma$ -bonding (single bond) are present in saturated hydrocarbons (Alkane). The  $\pi$ -orbitals lie at higher energy and are present in unsaturated hydrocarbons (Alkene and Alkyne). Then comes energy of orbitals which hold unshared pairs of electrons, the nonbonding (n) orbitals. The unoccupied, or antibonding orbitals ( $\pi^*$  and  $\sigma^*$ ) are the orbitals of highest energy. Compounds can go multiple possible transition with absorption of radiation with different energies.

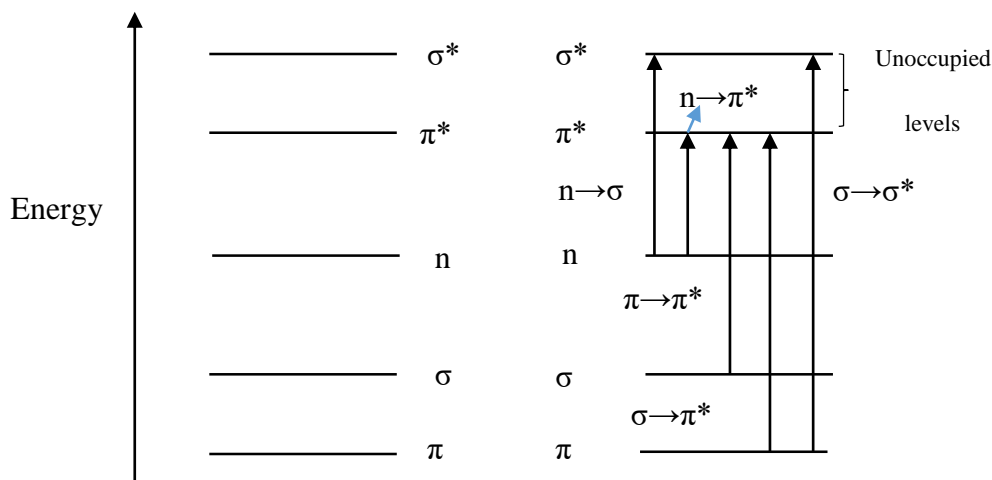


Figure 33: Electronic levels and transitions

Transition metal complexes: Transition metals have their valence electron(s) filled in five d-orbitals and have capacity of holding 10 electrons with spin up and down in each orbital. These metals often form one or more stable ions with incompletely filled d-orbitals. When their metal ions bond with ligands to form a complex, electrons in ligands and electrons in the five d-orbitals of metal repel each other. This repulsion causes splitting of d-orbitals, so some of the d orbitals gain energy and some lose. This difference in energy determines how much energy is absorbed when an electron is promoted from lower to higher level. This absorption of energy determines the colour of the complex. Hence, UV-vis spectroscopy can be used to determine how ligands are attached to central transitional metal ion in a complex. As an example  $\text{Cu}^{2+}$  ( $\text{CuSO}_4$ ) has 9 electrons in its d orbital. In aqueous solution, each  $\text{Cu}^{2+}$  ion is surrounded by 6 water ligands. d orbitals of it split into two group of differing energy. When white light is passed to the  $\text{Cu}^{2+}$  solution, some of the energy is used to promote (or excite) and electron form an orbital in lower group to an available orbital in the upper group equal to the energy gaps between higher and lower d orbitals. In this case, yellow light is absorbed, so the solution appears blue

(complementary color of yellow). The absorbed light depends upon nature of transitional metal and ligands. If small amount of ammonia is added in  $\text{CuSO}_4$  solution, it appears deep blue.

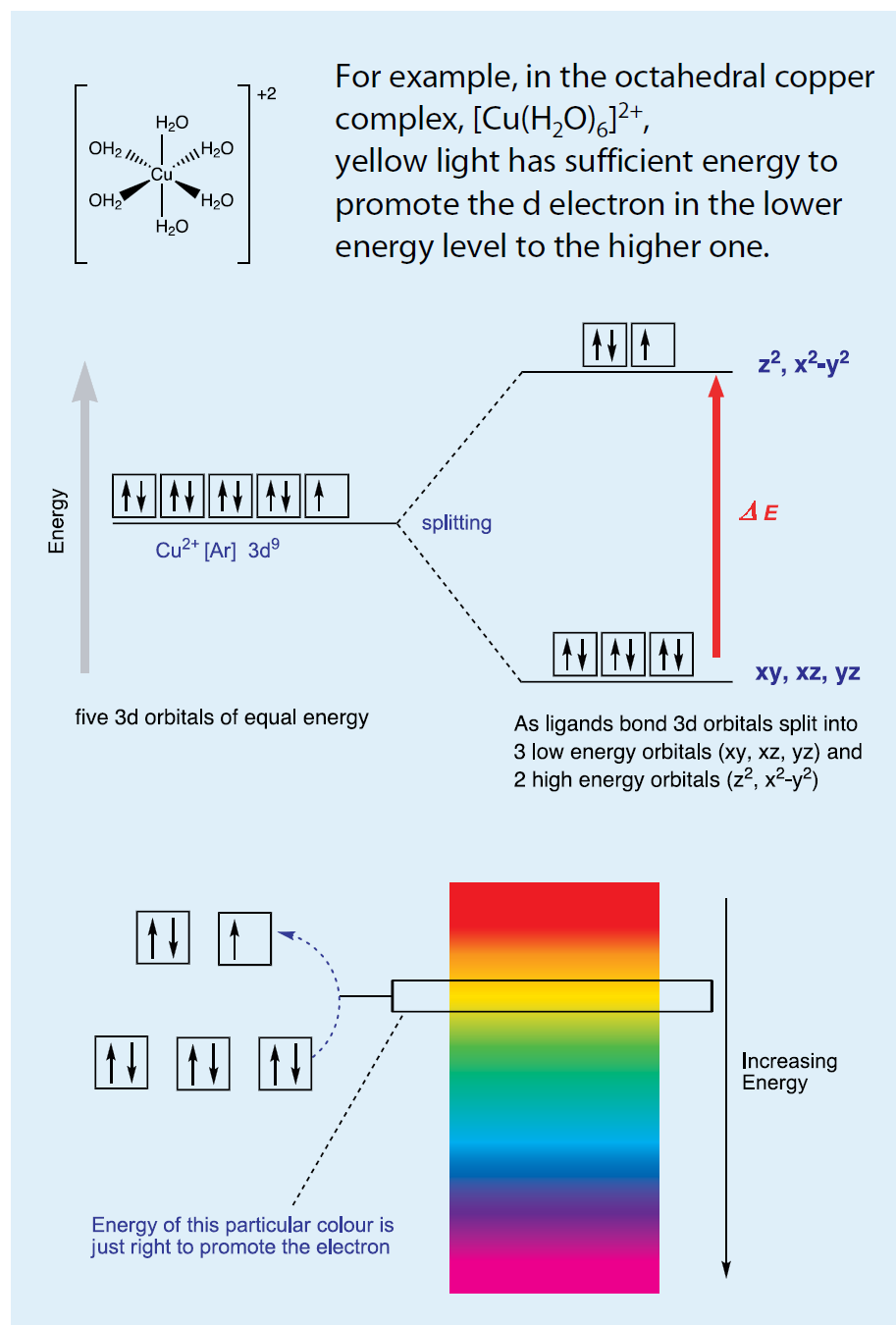


Figure 34: Splitting of d orbitals of  $\text{Cu}^{2+}$  ion in presence of water as ligand.

## 2.6.2 UV vis band structure:

For an atom, the absorption spectrum consists of very sharp lines, as would be expected for a quantized process between two discrete energy levels. However, for molecules, the absorption usually occurs over a wide range of wavelengths, because molecules normally have many excited modes of vibration and rotation at room temperature (even at absolute zero). A molecule may undergo electronic and vibrational-rotational excitation simultaneously. For a collection of molecules, there are many possible transitions, each differing from others by only a slight amount. So spectrophotometer cannot resolve them. Hence it shows band absorption band peaked at the wavelength of major transition.

The absorbance of electro-magnetic radiation depends upon concentration ( $c$ ) and pathlength ( $l$ ) and is given by Beer-Lambert's law

$$A = \log \left( \frac{I_0}{I} \right) = \epsilon cl \quad (47)$$

Where  $\epsilon$  is molar absorptivity of the sample. The absorbance is also equal to the difference between the logarithms of intensity of light entering the sample ( $I_0$ ) and the intensity of light transmitted ( $I$ ) through the sample.

UV-Vis Spectrophotometer:

The radiation emissions come from two sources: a deuterium lamp and a tungsten lamp. The deuterium lamp emits light radiation over a wavelength of 190 nm to 800 nm and the tungsten lamp contributes radiation in mainly in visible region and near-infrared regions (370 nm to 1100

nm). A good source should provide sufficient radiant energy over the entire wavelength region and intensity should remain constant during measurement. Also there may be strong characteristic peaks of the source which might not be subtracted completely during sample measurement. Usually Far UV quartz cuvettes (170-2700 nm) of 1 ml, 2 ml, 3 ml with 1 cm pathlength are used, which are filled with sample in liquid or solution form in organic or inorganic solvent. Light emitted by source is allowed to enter through optical fiber and after absorption light is passed to detector through another optical fiber. Detectors convert electromagnetic radiation into current or voltage which is directly proportional to intensity of radiation through sample. An ideal detector has high spectral sensitivity, quick response time and high signal to noise ratio. Detectors used in spectrophotometer are photomultiplier tubes, photo emissive tubes, photodiodes arrays, silicon photodiode transducers, silicon photodiodes, photovoltaic cells and photoconductivity transducers.

### **2.6.3 Experimental procedure for UV-vis measurement of Mo blue solution:**

Lamps of spectrophotometer are turned on at least 15 min prior to the experiments so that lamps reach full intensity and become stable. A blank scan even without cuvette was taken to see how good is the instrument working. An ideal blank scan should be 100% line in transmission mode. After that, cuvette filled 4/5<sup>th</sup> with deionized water was placed in sample holder, and background scan was taken. Later, deionized water was replaced with Mo blue solution and scanned with same integration time. Background scan of deionized water was subtracted from scan of Mo blue solution to get transmission UV-vis spectrum of Mo blue solution and later it was converted into absorption spectrum. Mo blue solution was further diluted into 50%, 25% and 12.5% and UV-vis measurement were taken to see any change in the position of peak with



change in concentration of Mo blue. As same cuvette was used for all the experiment, the pathlength during all the experiments were fixed.

#### **2.6.4 Application of UV-vis spectroscopy:**

This technique can be easily applied to find out the concentration of solution. So it is used in dye, ink and paint industries for quality control. It can also be used in quantification of organic materials and heavy metals in fresh water. It enables to study rate of reactions, and determine rate equations for reactions, from which a mechanism can be proposed. It is also used in pharmaceutical industries and in the study of enzyme kinetics.

## Chapter 3 Characterization of GO used for experiments:

### 3.1 Introduction

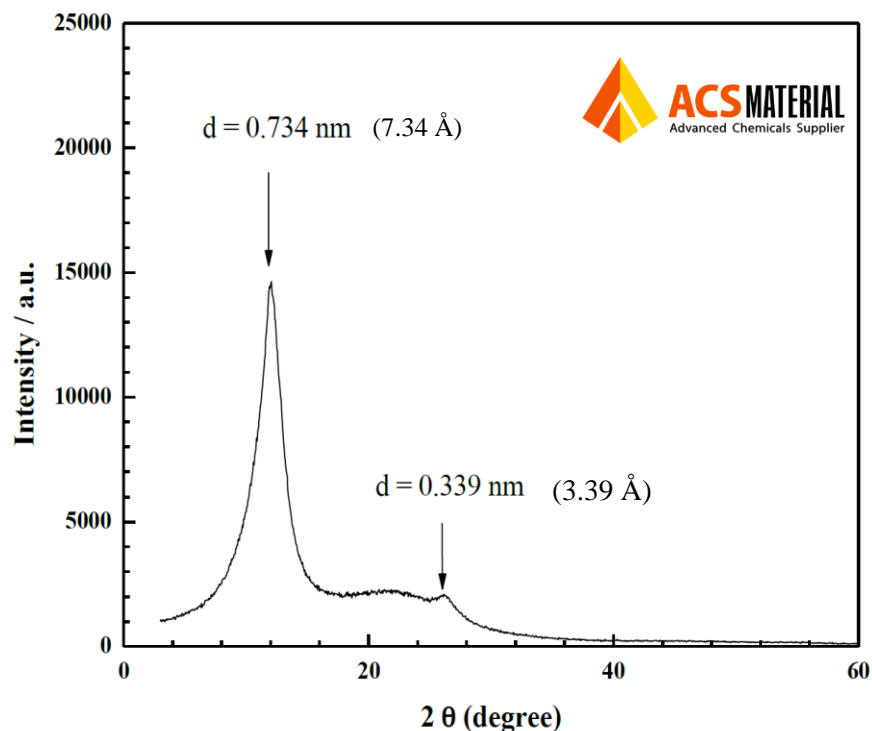


Figure 35: XRD for GO provided by ACS Material for single layered GO. Diffraction peak at 7.34 Å and 3.39 Å are due to interplaner spacing between adjacent GO layers and precursor graphite layers (002) respectively

Single layer GO (10mg/ml) was purchased from ACS materials. The XRD provided by ACS is shown in fig 35. The sharp peak at 7.34 Å is due to interplaner spacing between adjacent single layer GO and at 3.39 Å is due to remnant of graphite used to make GO. Spacing between adjacent layers of GO is higher than graphite because of intercalation of water molecules between the layers of GO bonded with hydrogen bond. The reported spacing between GO layers for dry GO is 6.1-6.3 Å and for hydrated GO is 12 Å [61]. Fig 35 doesn't show any diffraction peak due to (100) and (110) Miller planes of graphene or graphite having spacing 2.13Å and

1.23Å respectively. Huge background between 0-36°C in diffraction confirms that GO is mostly amorphous.

Before using as purchased GO in making GMO/r-GO and MoO<sub>2</sub>/r-GO nano-composite, it was characterized using XRD, TEM (*in situ* thermal annealing) and IR measurement.

### 3.2 Result and Discussion:

1. **Diffraction (XRD and SAED):** Unlike XRD provided by ACS material, XRD measurement of GO (fig 37) showed interlayer spacing of GO layers of 3.58 Å which is very close to (002) peak (3.4 Å) for graphite. The broad peak at 3.58 Å shows that ordering is poor and GO layers are arranged in random orientation. The corresponding peak in SAED is absent for before and after heating (fig 36 and 37) of GO in TEM because the layers of GO are perpendicular to the electron beam. SAED of before and after heating (fig 36 and 37) showed similar features at the real spacing of 2.13 and 1.23 Å corresponding to the (100) and (110) Miller planes of graphene present in GO. XRD showed shoulder peak at 2.13 Å but peak at 1.23 Å is invisible. As X-rays are electromagnetic waves and they are scattered by electron charge density of material through which they traverse, so at higher Bragg's angle (larger reciprocal length) they show poor diffraction. Whereas electron beam due to their higher mass are scattered due to both electron charge density surrounding nucleus and nucleus, they show better diffraction peak at larger Bragg's angle (reciprocal distance)

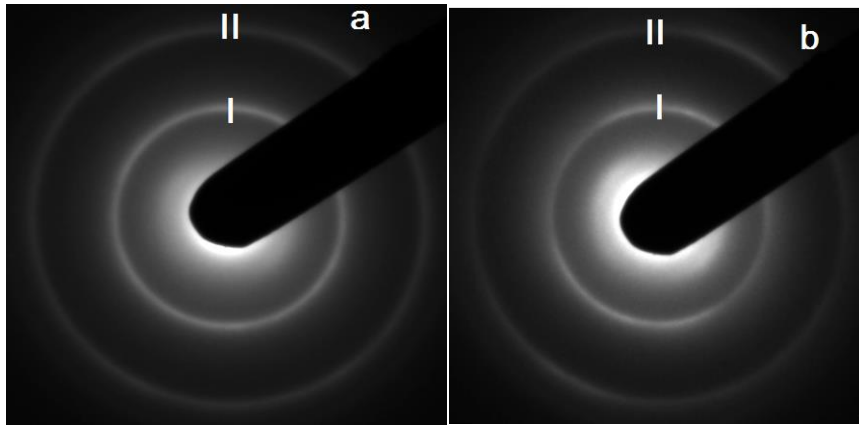


Figure 36:(a) SAED of GO before heating and (b) SAED of GO at 659°C

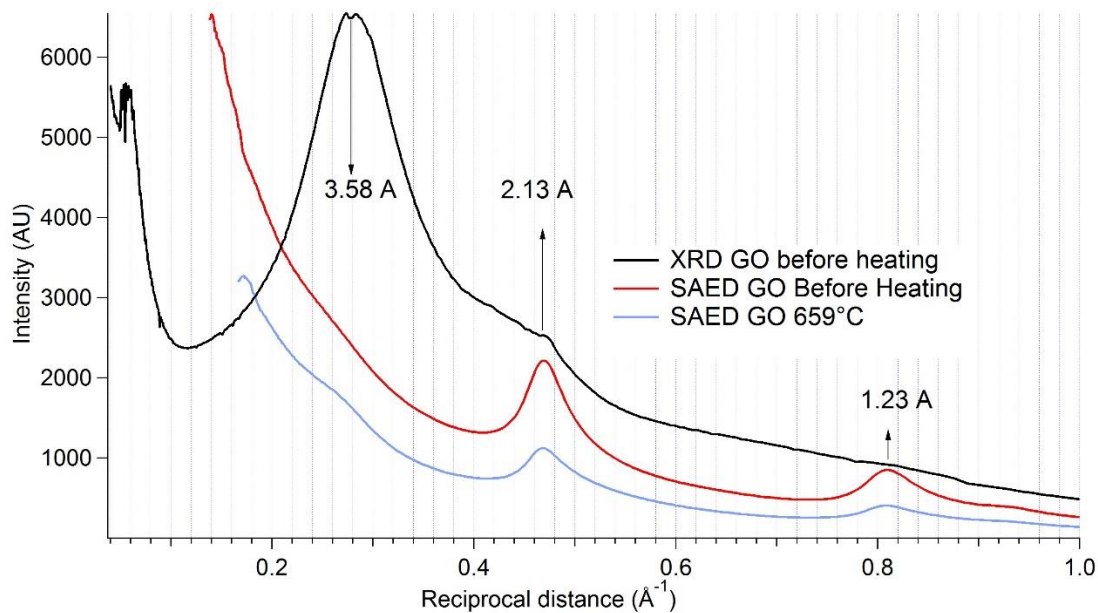


Figure 37: Comparison of XRD and SAED (before and after in situ vacuum annealing) of as purchased single layered GO Diffraction curves are stacked over another for better comparison

2. **IR measurement:** IR spectrum of GO before heating showed presence of hydroxyl (-OH) stretching and bending peaks at  $3300$  and  $1625\text{ cm}^{-1}$  respectively, while these peaks are absent for GO after heating. This shows that GO before heating has water intercalated between its layer and it vanished after heating to  $659^\circ\text{C}$ . Beside hydroxyl, there is also presence of

carbonyl ( $1728\text{ cm}^{-1}$ ), carboxyl ( $1423\text{ cm}^{-1}$ ) and alkoxy ( $1087\text{ cm}^{-1}$ ) functional group in GO before heating. But after heating only C=C stretching peak at  $1556\text{ cm}^{-1}$  and epoxy peak at  $1210\text{ cm}^{-1}$  are observed. This implies that most of the functional group with oxygen present in GO are removed during thermal annealing. Visible image of GO sample made in TEM grid in fig 39 shows sample in transmission and reflection modes before and after heating. GO sample formed in TEM grid is translucent before heating (fig 39 a) and turns opaque after heating (fig 39 c).

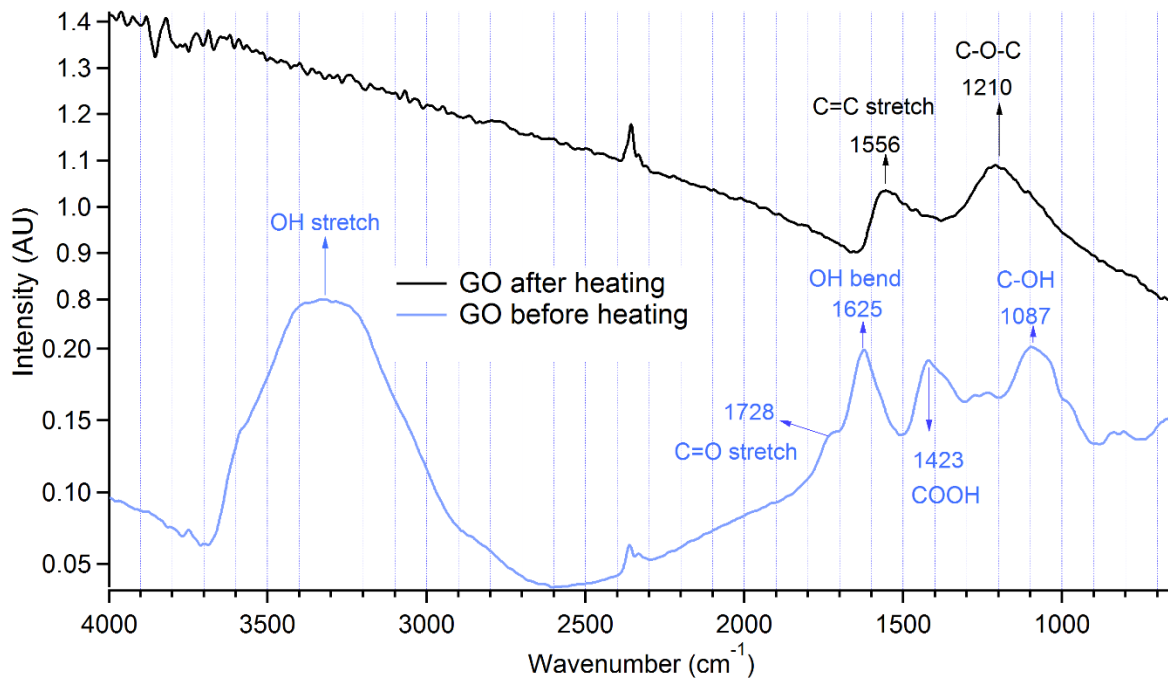


Figure 38: IR spectra of GO before and after heating

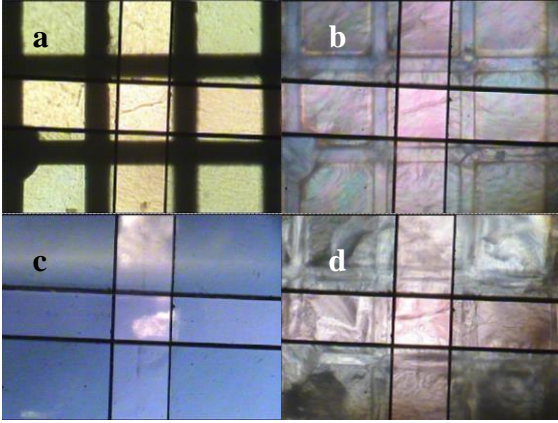


Figure 39: Visible image of GO sample in TEM grid for IR measurement. IR spectra were taken from the region between the crossbar. (a) Sample before heating in transmission mode (b) Sample before heating in reflection mode (c) Sample after heating in transmission mode (d) Sample after heating in reflection mode.

### 3.3 Conclusion:

Diffraction measurement done on as purchased single layered GO showed the inter layer spacing of GO layers are far smaller ( $3.58 \text{ \AA}$ ) compared to claimed ( $7.38 \text{ \AA}$ ). And the broad background observed in x-ray and electron diffraction shows GO is mostly amorphous. IR measurement done before heating showed GO has water present between its layers. Beside water it also has carbonyl, carboxy and epoxy peak along with C=C bonding. The oxygen present in different functional groups attached with GO makes it hydrophilic. After annealing GO is reduced but it still has epoxy functional group and C=C bonding. Due to loss of most of the oxygen containing group, it is difficult for water to form hydrogen bonding with reduced GO resulting into hydrophobic reduced GO.

## Chapter 4 Characterization of Molybdenum blue solution:

Amorphous sub-oxide of Mo is prepared by reduction of molybdic acid with Mo metal. So formed sub-oxide is highly soluble and blue in colour, so it is named as Molybdenum blue. The Mo blue when dried still carry water molecules at room temperature. Mo atom in Mo blue has oxidation state between +4 and +6.

### 4.1 Introduction

Molybdenum blue is a term applied for different polyoxometalates of molybdenum containing Mo(V), Mo(VI) and have blue colour. They may contain hetero atom such as phosphorus or silicon. They are amorphous and have complex molecules. The Mo blue reported here is also an amorphous oxide of molybdenum with deep blue colour prepared by reduction of Mo(VI) oxide by Mo metal in presence of water. It is known from different literatures that only Mo(VI) and Mo(IV) oxides of Mo are most stable oxides of molybdenum [62]. Formation of  $\text{MoO}_3$ (orthorhombic) and  $\text{MoO}_2$ (monoclinic) are favourable in oxidizing and reduction environments, respectively. Some other known crystalline form of Mo oxides with oxidation state between +4 and +6 are  $\text{Mo}_4\text{O}_{11}$ ,  $\text{Mo}_5\text{O}_{14}$ ,  $\text{Mo}_8\text{O}_{23}$ ,  $\text{Mo}_{18}\text{O}_{52}$ .

Ammonium molybdate  $((\text{NH}_4)_2\text{MoO}_4)$ , ammonium heptamolybdate  $((\text{NH}_4)_6\text{Mo}_7\text{O}_{24}\cdot 4\text{H}_2\text{O})$ , sodium molybdate  $(\text{Na}_2\text{MoO}_4)$  and molybdenum phosphate  $(\text{Mo}_3\text{O}_{16}\text{P}_4)$  are soluble compound of molybdenum, and they have been used as a precursor for formation of nanocrystals of  $\text{MoO}_3$  and  $\text{MoO}_2$  in different forms of carbons (GO, amorphous carbon and carbon nanotubes etc). Mo blue reported here is pure oxide of molybdenum, highly soluble in water and can be mixed with GO

(or any hydrophilic solvent) in any ratio to synthesize nano-composite of MoO<sub>2</sub> and reduced graphene oxide.

#### **4.2 Preparation of Mo blue solution:**

While doing IR measurement on MoO<sub>3</sub> water solution (molybdic acid) on aluminum flowcell with germanium window, it was discovered that the solution is reduced to blue solution. Similar results were obtained when the solution was mixed separately with aluminum, germanium, silicon, copper and tantalum. However, no change in colour were observed for mixing the solution with carbon (diamond and graphite), stainless steel and glass. Finally, Dr. Marvin Schoefield succeeded in reducing the solution to Mo blue solution using Mo powder which is described as follow.

Sparingly soluble 100 gm of MoO<sub>3</sub> (Sigma Aldrich) powder was mixed with 200 ml of de-ionized water for a couple of days. Clear water like, molybdic acid formed at the top was separated from MoO<sub>3</sub> powder settled at the bottom. 100 mg of Mo metal powder (<150 μm, Sigma Aldrich) was mixed with molybdic acid. The clear solution of molybdic acid was reduced immediately by Mo metal, which was indicated by change in colour of clear water like solution into light blue. In couple of days, solution became deep blue. Finally, so formed Mo blue solution was separated from Mo metal settled at the bottom of beaker.

#### **4.3 Experimental method:**

For TEM measurements, a drop of Mo blue solution was dropped in 300 mesh Ni grid with silicon monoxide film and dried in air. Selected area electron diffractions (SAEDs) and bright



field imaging were performed using Hitachi single tilt holder inside a Hitachi H9000NAR TEM operating at an accelerating voltage of 300 keV, at a constant column pressure of  $10^{-7}$  Torr. Gatan Orius SC CCD was used for capturing diffraction patterns and bright field images. For XAS and XRD measurement, Mo blue solution was filled into amorphous glass capillary tube of length 10 cm and internal diameter of 1 mm. Both measurements were performed at beamline 12BM, Advanced Photon Source (APS) at Argonne National lab Chicago, IL. X-ray powder diffraction data was collected near Mo-K edge (19.95 keV) using Pilatus 100k detector and X-ray absorption spectroscopy (XAS) data around Mo-K edge (20 keV) was collected using ion chambers (nitrogen filled). For IR measurement, a drop of Mo blue solution was spread over diamond window, and measured in a Bruker Hyperion 3000 IR Microscope using MCT detector. For comparison,  $\text{MoO}_3$  powder was spread over another diamond window. For background measurement, a scratch was drawn on diamond window using clean twister, nearby Mo blue sample (or  $\text{MoO}_3$ ). For UV-Vis measurement, a rectangular Far UV quartz cuvette (Pike technologies) with pathlength 10 mm, was filled with Mo blue solution of different concentrations, and measured using single beam photospectrometer. Reference measurement was done with the same cuvette with de-ionized water and comparison was done with its precursor  $\text{MoO}_3$  solution (molybdic acid) in UV and visible region using two different sources for different regions.

#### **4.4 Results and discussions:**

TEM measurement: SAED patterns (not shown here) obtained didn't show any diffraction spots or rings and had only amorphous background. Bright field images (not shown here) were also thick and unclear.

#### 4.4.1 IR measurement:

IR measurement of MoO<sub>3</sub> and Mo blue dried on diamond windows are shown in fig 40. Both spectra have high transmission at around 1020 cm<sup>-1</sup>. Mo-O stretching at 997 cm<sup>-1</sup> in MoO<sub>3</sub> is shifted to 963 cm<sup>-1</sup> in Mo blue. Mo blue has broad peak at 3300 cm<sup>-1</sup> due to -OH stretching and -OH bending vibration at 1613 cm<sup>-1</sup> due to presence of water molecules surrounding the Mo oxide. Difference in IR spectrum of Mo blue confirms, it is chemically different from its precursor MoO<sub>3</sub>.

#### 4.4.2 UV-Vis measurement:

UV-Vis measurement of MoO<sub>3</sub> in solution in fig 41 shows why it is colourless as there is no absorption of light in visible region. But in case of Mo blue, there is strong absorption between 500-950 nm and almost negligible absorption between 400-500 nm. The band between 400-500 nm corresponds to violet, indigo and blue light. As light band from green to red are strongly absorbed, the solution only transmits and reflect blue light, so the solution appears blue. The absorption of light in visible region is due to the transition of the single unpaired electron in d<sub>xy</sub> orbital to the doubly degenerate Mo=O( $\pi^*$ ) or two higher d( $\sigma^*$ ) levels.

Both MoO<sub>3</sub> and Mo blue absorb in UV region at 280 nm (4.4 eV) and 240 nm (5.16 eV) respectively. These broad absorption band in UV region are ascribed to the ligand metal charge transfer (LMCT) bands originating from the promotion of electrons from the filled Mo=O ( $\pi$ ) levels to the d orbitals. The energy of this absorption band is sensitive to the local symmetry of Mo ion. For tetrahedral coordinated Mo LMCT and octahedral coordinated Mo LMCT bands usually appear at 270-340 nm and 220-270 nm respectively. Distortion of local symmetry of Mo

ion from octahedral to tetrahedral shifts the LMCT band to lower wavelength [62]. For MoO<sub>3</sub> solution, Mo ion is surrounded 6 oxygen ions (Octahedral symmetry) and it is observed from UV fig 41 that LMCT band for Mo blue is at lower wavelength. This blue shift in LMCT band for Mo blue solution hint toward more distorted structure of Mo blue compared to MoO<sub>3</sub>.

#### 4.4.3 XANES:

Normalized absorption of X-ray of different oxides of molybdenum are shown in fig (42). The most striking feature of XANES analysis is presence of pre-edge peak at 20.007 eV for all Mo oxides in which oxidation state of Mo is greater than +4 (MoO<sub>3</sub>, Mo<sub>4</sub>O<sub>11</sub>, Mo<sub>5</sub>O<sub>14</sub>, Mo<sub>8</sub>O<sub>23</sub> and Mo<sub>18</sub>O<sub>52</sub>). The absorption of X-ray at pre-edge corresponds to the 1s→4d transition of photoelectron in Mo atom. But this transition is forbidden by dipole selection rule ( $\Delta l = \pm 1$ ), as also seen in the case of MoO<sub>2</sub>. In case of Mo oxides with oxidation state higher than +4, there is extensive mixing of oxygen p levels with the metal d orbitals upon formation of the molecular orbital (Mo = O). The added p-character makes this transition more allowed in Mo oxides with oxidation state greater than +4 compared to the compound without extensive d-p mixing (MoO<sub>2</sub>) [63] [64].

The comparative study of XANES of MoO<sub>3</sub> and Mo blue in fig (43), both shows presence of pre-edge peak at 20.007 eV and similar features after edge. This shows in Mo blue, oxidation state of Mo atom is greater than +4.

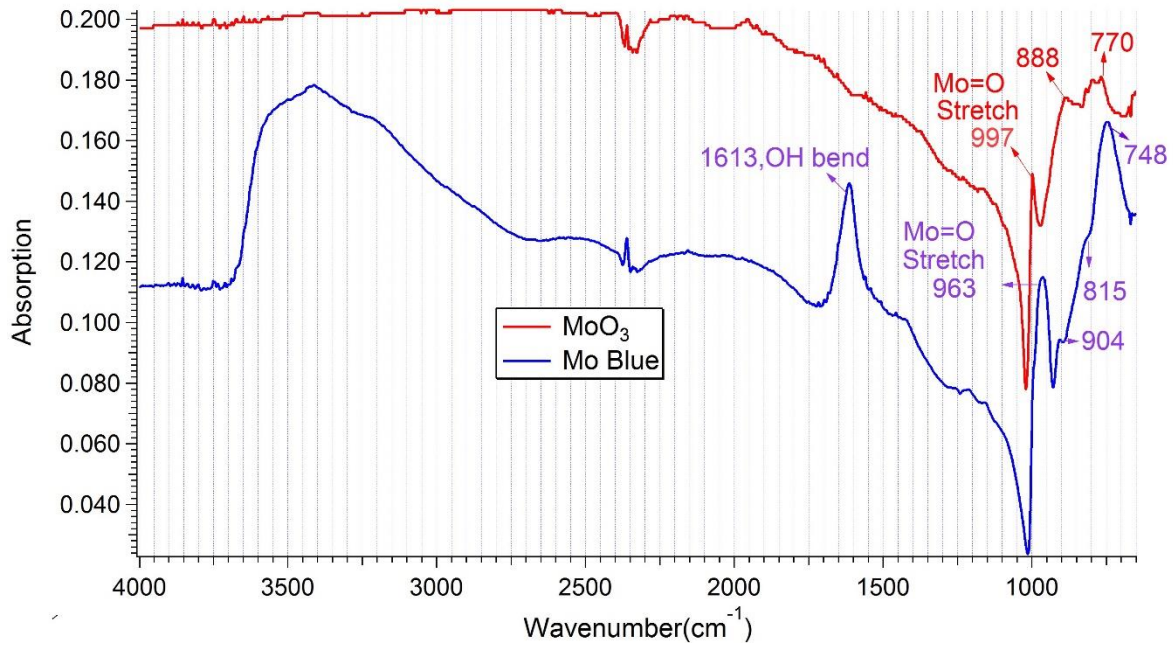


Figure 40: IR spectrum of Mo blue on diamond window compared with its precursor MoO<sub>3</sub>

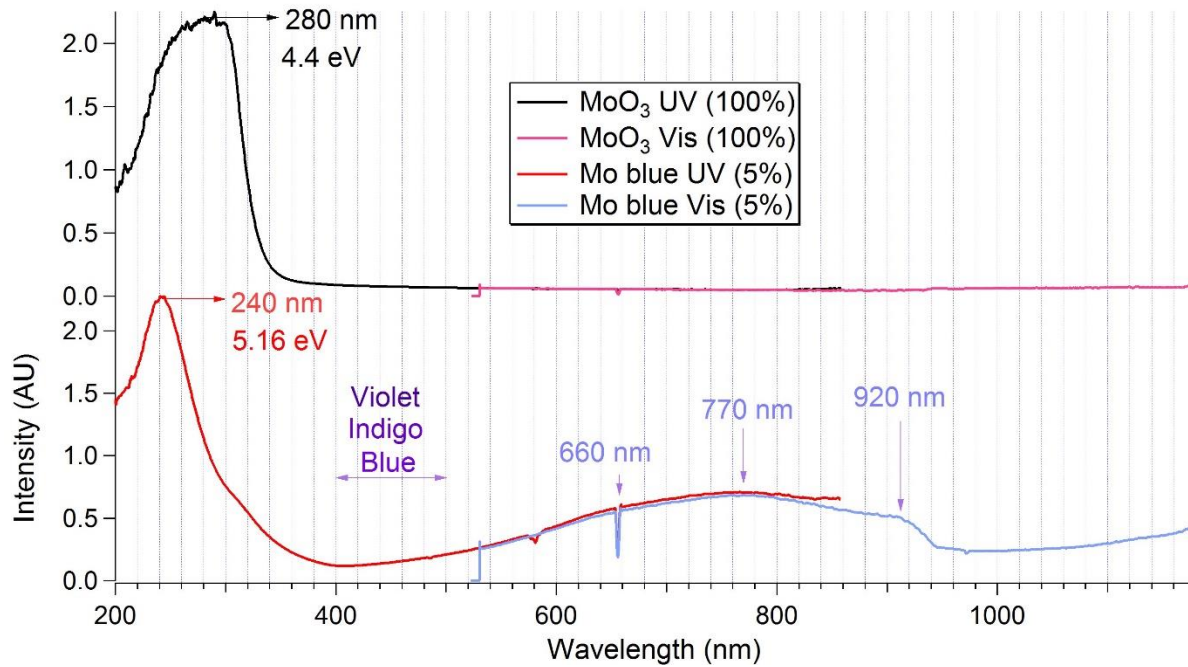


Figure 41: UV Vis measurement of Mo blue and its precursor MoO<sub>3</sub> solution. Sharp absorption observed around 580 and 655 nm are due to characteristic emission peak of source and are irrelevant to the absorption by sample.

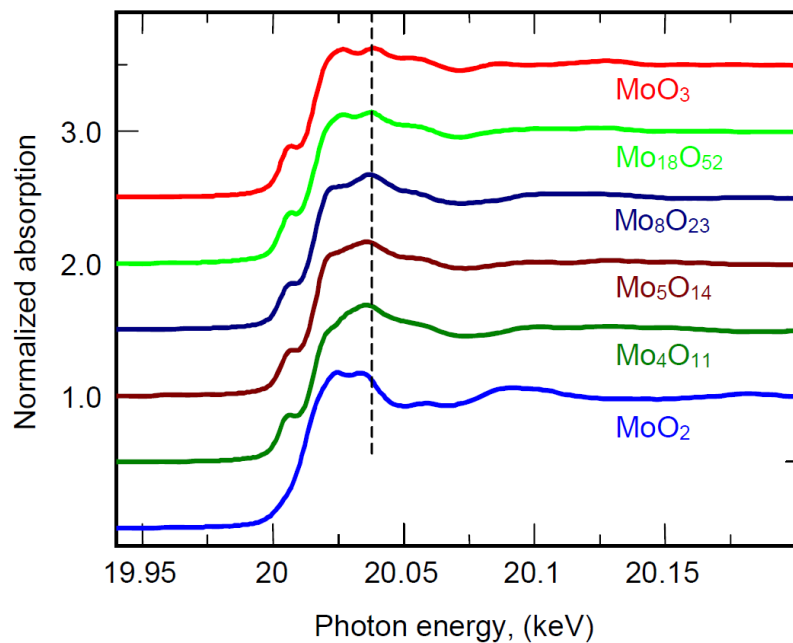


Figure 42: Mo K-edge XANES of Mo oxides [65]

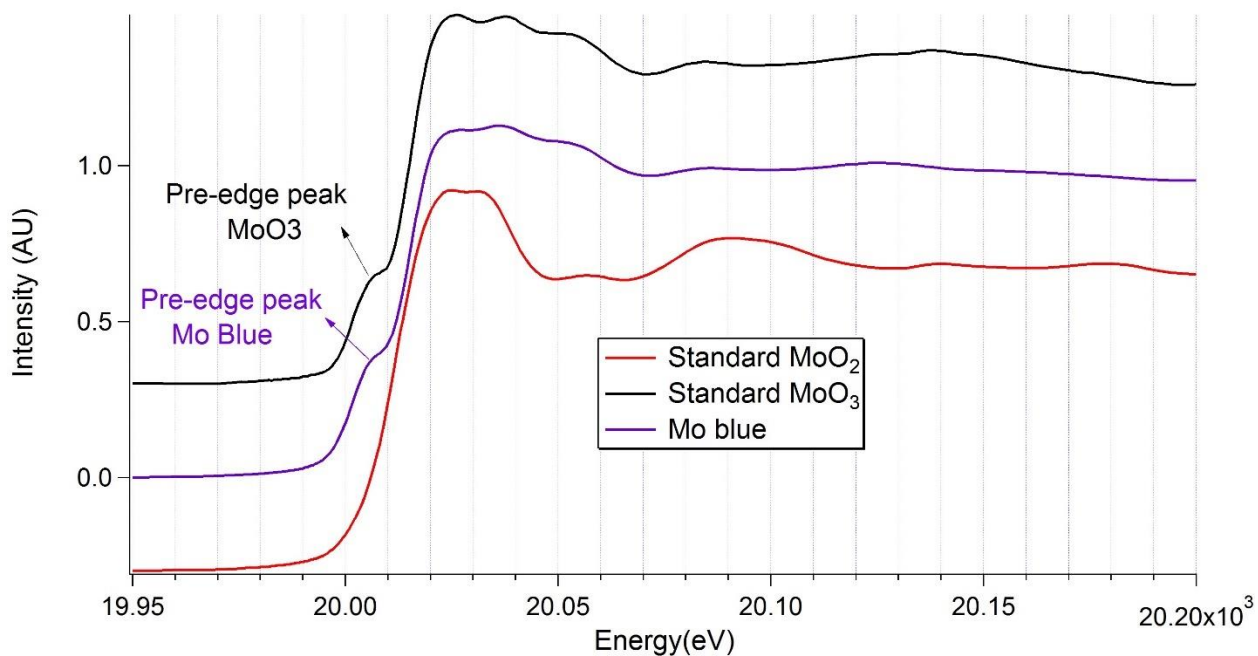


Figure 43: XANES of Mo blue along with  $\text{MoO}_2$  and  $\text{MoO}_3$ . Pre-edge peaks are present in both Mo blue and  $\text{MoO}_3$  where as it is absent in  $\text{MoO}_2$ . Also the features of XANES are quite similar for Mo blue and  $\text{MoO}_3$ .

#### 4.5 Conclusion:

We demonstrate preparation of new soluble sub-oxide of Mo by reduction of MoO<sub>3</sub> solution with Mo metal. The sub-oxide is amorphous as observed from X-ray and electron diffraction. UV-Vis measurement shows that sub-oxide has structure more distorted than its precursor MoO<sub>3</sub>. XANES analysis done of Mo blue shows similar pattern to its precursor MoO<sub>3</sub> and it has oxidation state higher +4.

## Chapter 5 Forming graphene and graphene monoxide from amorphous lacey carbon

Graphene and graphene monoxide have been obtained by heating amorphous lacey carbon exposed to molybdenum solution containing a variety of  $\text{Mo}_x\text{O}_y$  species at moderate temperature ( $600^\circ\text{C}$ ) in high vacuum ( $10^{-7}$  torr). *In-situ* selected area electron diffraction patterns show evolution of the amorphous carbon structure, from room-temperature broad rings typical for  $\text{sp}^2$  hybridization, into stronger and more defined graphene rings (centered at 0.213 nm and 0.123 nm) and graphene monoxide rings (at 0.246 nm and 0.148 nm) upon heating above  $600^\circ\text{C}$ . This catalytic thermal method provides an alternative pathway to production of crystalline graphene and graphene monoxide from amorphous carbon.

### 5.1 Introduction

Graphene, due to its single layered two dimensional crystalline structure made up of  $\text{sp}^2$  hybridized carbon, has attracted great interest in recent years. It has high specific surface area, extraordinary electronic properties and electron transport capabilities, high thermal conductivity [66] and is a semiconductor with zero bandgap [8]. It can be functionalized to make semiconducting device that function at high temperature. High specific surface area, and high electronic conductivity make it suitable for Lithium ion batteries [LIB] [67]. Large scale production of graphene is accomplished employing chemical methods such as chemical vapor deposition or via epitaxial growth of graphene on silicon carbide (SiC). Amorphous carbon which is a non-crystalline phase of carbon, consists of three-dimensional matrices of short-range ordered carbon atoms, and a mixture of orbital hybridization types (linear  $\text{sp}$ , trigonal planar  $\text{sp}^2$

and tetrahedral  $sp^3$ ) [68].  $sp^2$  hybridized orbitals are thermodynamically more stable than  $sp^3$  ones. The re-ordering of atoms of amorphous carbons to  $sp^2$  hybridized graphite can be accomplished by (1) catalytically active transition metals; (2) laser irradiation; (3) ion irradiation; (4) mechanical shear forces; or (5) high temperature annealing under high pressure. Marsh and Warburton summarized possible mechanisms of catalytic graphitization as: (1) precipitation of the dissolved carbon, (2) formation and decomposition of carbides, or (3) removal of distortion and defects within the crystallites by chemical processes [69]. Another interesting two dimensional material is graphene monoxide (GMO), which has structure similar to graphene, have quasi hexagonal unit cell with two carbon atoms bridged by double-epoxy pairs and have calculated direct bandgap of 0.9 eV [27]. Recent density functional theory (DFT) calculations have shown the formation of GMO is energetically favorable, and the bandgap can easily be tuned (0-1.35 eV) by applying strain [28] or creating defect in GMO structure [29].

In the present work, we report experimental evidence that multi-layered graphene and graphene monoxide can be generated from *in-situ* heating of amorphous carbon lacey films by catalytic property of the hydrated molybdenum oxide ( $Mo_xO_y$ ) at comparatively low temperature and pressure.

## 5.2 Sample preparation

50 mg Mo powder (Sigma Aldrich) was dissolved in 0.5 ml DI water and kept at room temperature and pressure until the color of the solution became deep blue (77 days for the experiments presented here). Infrared spectroscopy reveals that the dried deep blue solution is different from Molybdenum(VI) trioxide and Molybdenum(IV) dioxide, which is consistent with



the common wisdom of Molybdenum(V) pentoxide and water complex. 5 $\mu$ l of the blue solution was diluted with 45  $\mu$ l of DI water and a 2  $\mu$ l drop of the diluted solution was applied to a 200 mesh Ni-grid covered with amorphous lacey carbon (Ted Pella). The sample was dried in air for a day.

Sample for IR measurement was prepared by drying Mo blue solution on diamond window. For comparison, about 5g of MoO<sub>3</sub> (Sigma Aldrich) powder was mixed with excess of deionized water for a couple of days. Sparingly soluble MoO<sub>3</sub> in water forms molybdic acid. So formed few drops of clear solution of molybdic acid was deposited on diamond window and dried in air for overnight. After drying it looks much similar to powder MoO<sub>3</sub>. Also water insoluble MoO<sub>2</sub> (Sigma Aldrich) powder was spread over another diamond window for IR measurement for comparison (not shown here).

### **Transmission electron microscopy**

Upon drying in air for one day the sample was characterized in a Hitachi H9000NAR transmission electron microscope (TEM) operating at 300 kV by selected area electron diffraction (SAED) and energy dispersive x-ray spectroscopy (EDX) both before and after *in-situ* heating to 762°C with a Gatan tantalum-cup holder. Images and diffraction patterns were collected using a Gatan CCD camera in the TEM, including bright field images (BF), dark field images (DF), and SAED, and EDX data was recorded using Noran EDX detector. The heating rate was maintained at 30°C/min and column pressure was 10<sup>-7</sup> torr.

### **Infrared spectroscopy**

IR measurement was performed in transmission mode using MCT detector with 256 scans on Bruker Hyperion 3000 IR Microscope using MCT detector. Small portion of diamond window with sample was cleaned by drawing a line (scratch) on it, using a sharp clean metal for background measurement and eventually, sample measurement was performed in area nearby the line

### 5.3 Results

In figure 44 , TEM BF images of the amorphous lacey carbon film after adding the blue solution are shown, both before (44 a) and after (44 b) heating in the vacuum of the TEM without exposure to intermediate energy electrons during heating. One representative area (A1) is chosen for SAED and EDX comparative studies according to its appearance before heating. Multiple areas (H1 to H5) in figs (44a) and (44b) are clearly holes in lacey carbon since their contrast is the same as that of background. Focusing on fig (44a), before heating, A1 is clearly lacey carbon that likely has some deposits of molybdenum solution with distinct boundaries. The contrast and structures in fig (44b) look different from (44a) due to heating and modified microscope alignment. (The heating occurs on a separate holder, and the sample is transferred back and forth from the single tilt (imaging) holder to the heating holder.) The boundaries in fig (44a) are more distinct.

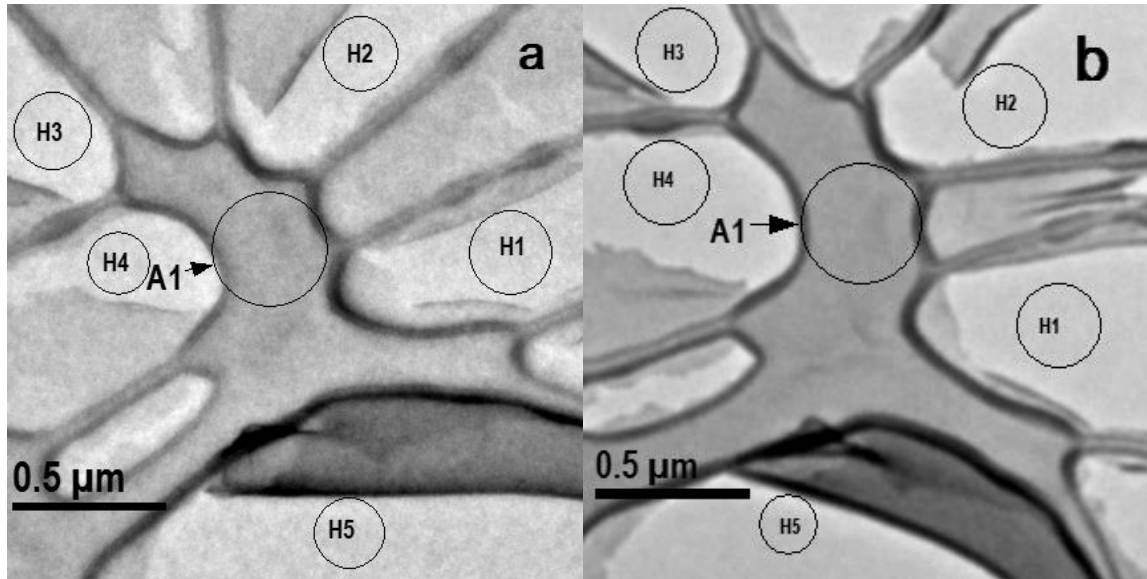


Figure 44: Bright field TEM images of lacey carbon film with Mo blue solution before heating (a) and after in-situ heating at 762°C (b). Diffraction and spectroscopy data is taken from areas, like A1, that are initially amorphous and become ordered upon heating. Holes in the film are denoted as H1-H5.

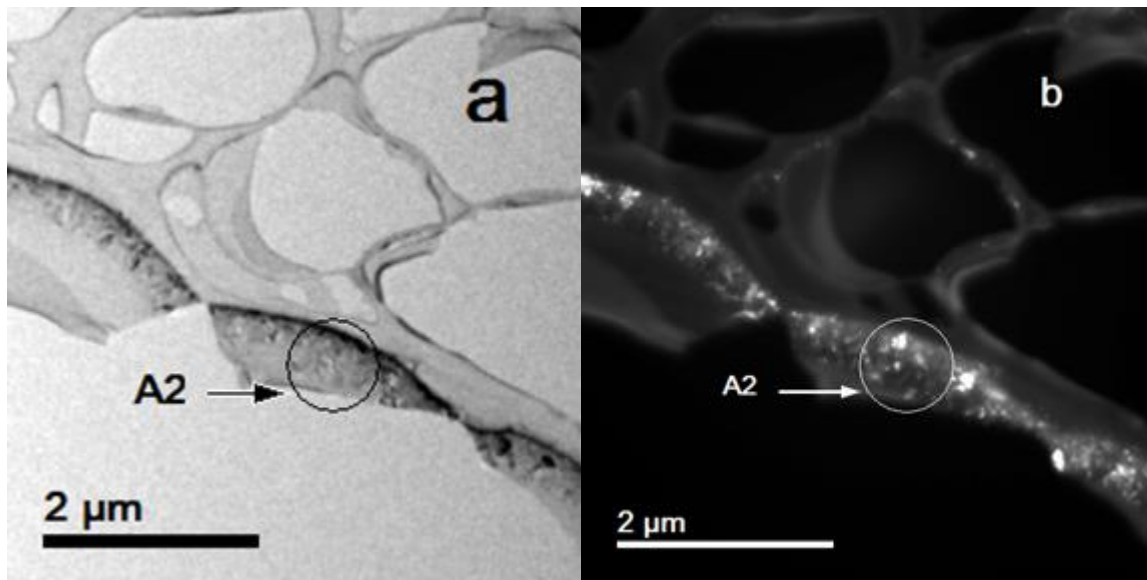


Figure 45: (a) Bright field TEM images of lacey carbon film (after in-situ heating at 762°C) with Mo blue solution at region A2 with very small dark spots (b) Dark field image of same region after in-situ heating at 762°C showing bright spots which look dark in bright field image. Spots are formed because these nano particles have different contrast than that of amorphous lacey carbon.

After heating, in nearby TEM grid of region A1, some areas with lacey carbon with bright spot in bright field image are also found (fig 45 a) or dark spots scattered in lacey carbon (fig 45 b). These spots have different contrast compared to lacey carbon.

The relative concentrations of carbon to molybdenum before and after heating reveal similar relative signals for carbon and molybdenum EDX peaks, with evidence for oxygen and carbon in both cases. SAED taken at room temperature before heating (fig 48a) shows an amorphous background with two dim and broad rings that are very similar in position and intensity as those obtained from lacey carbon that has not been exposed to molybdenum (intensity profiles in fig 49). The peak positions of these broad rings correspond to dominant  $sp^2$  bonding in the amorphous lacey carbon. It is notable that addition of the Mo blue solution and its subsequent drying does not appear to change the local carbon-to-carbon bonding.

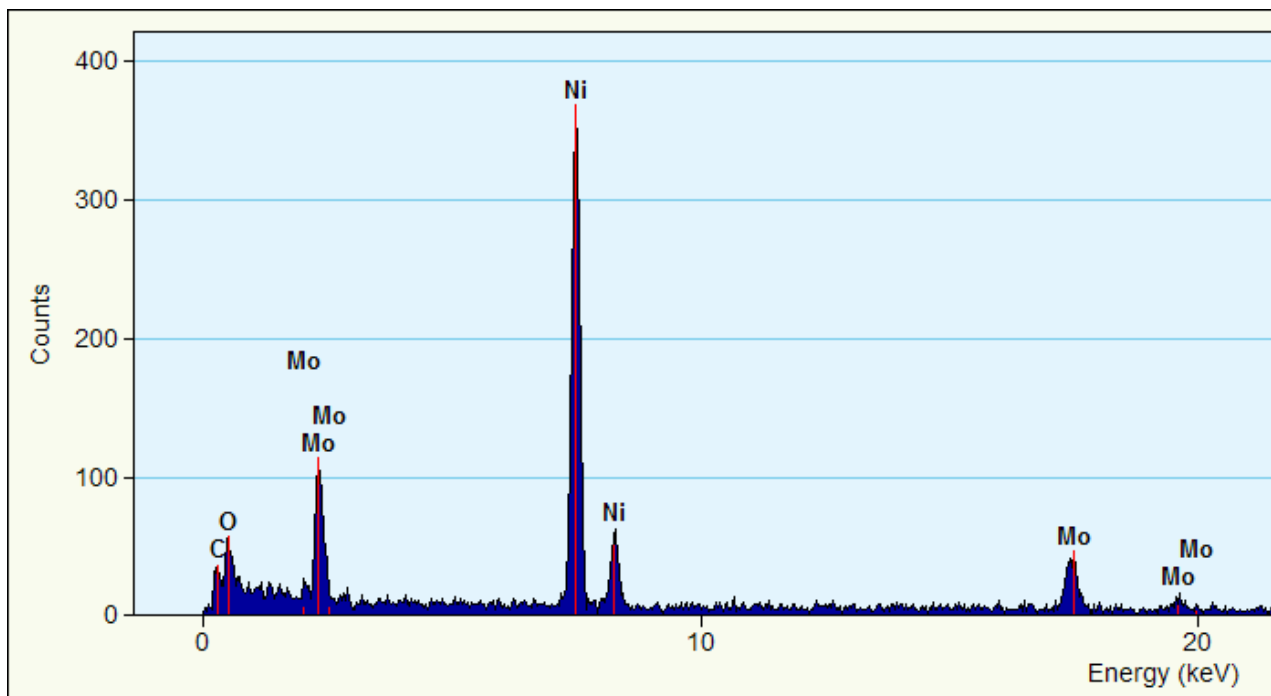


Figure 46: EDX at region A1 before heating showing the presence of carbon, oxygen and molybdenum in sample. Presence of sharp peak of Nickel is due to Ni grid.

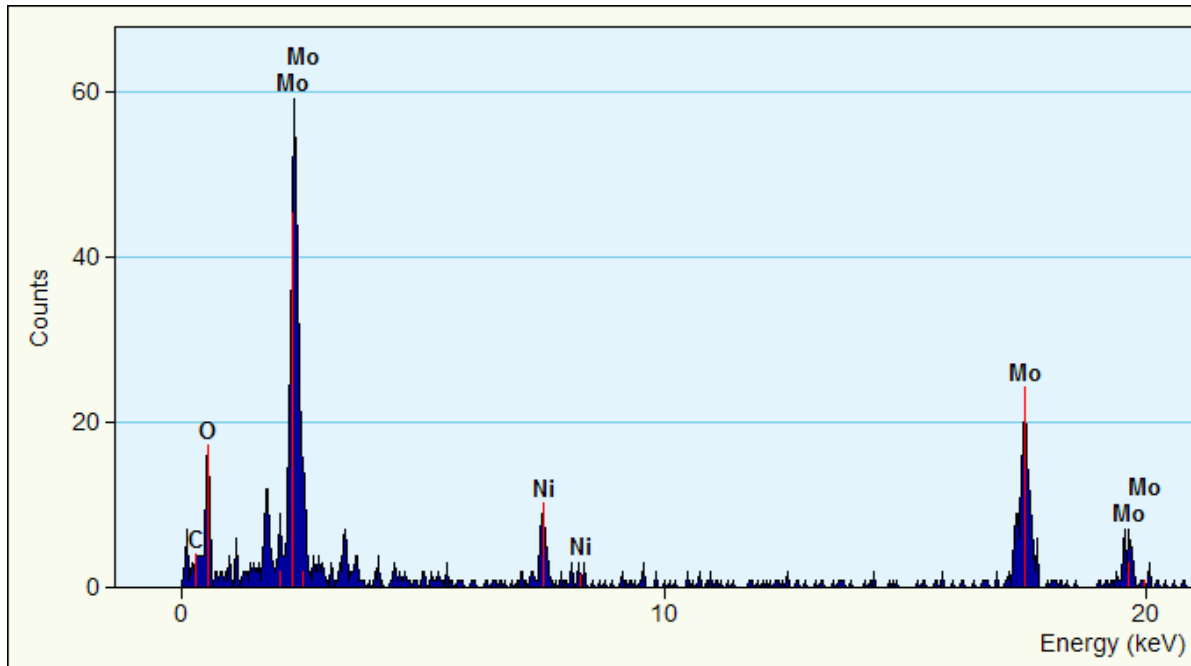


Figure 47: EDX at region A1 after heating showing similar presence of carbon, oxygen, molybdenum and nickel from grid

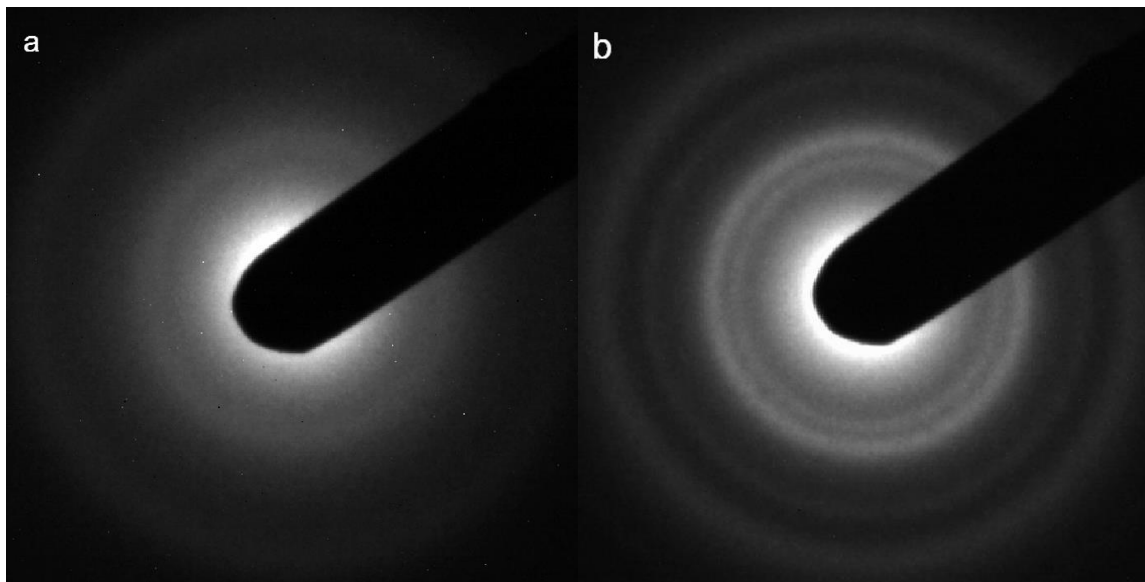


Figure 48: SAED pattern of lacey carbon film with Mo blue solution (Region A1) before heating (a) and after in-situ heating (b)

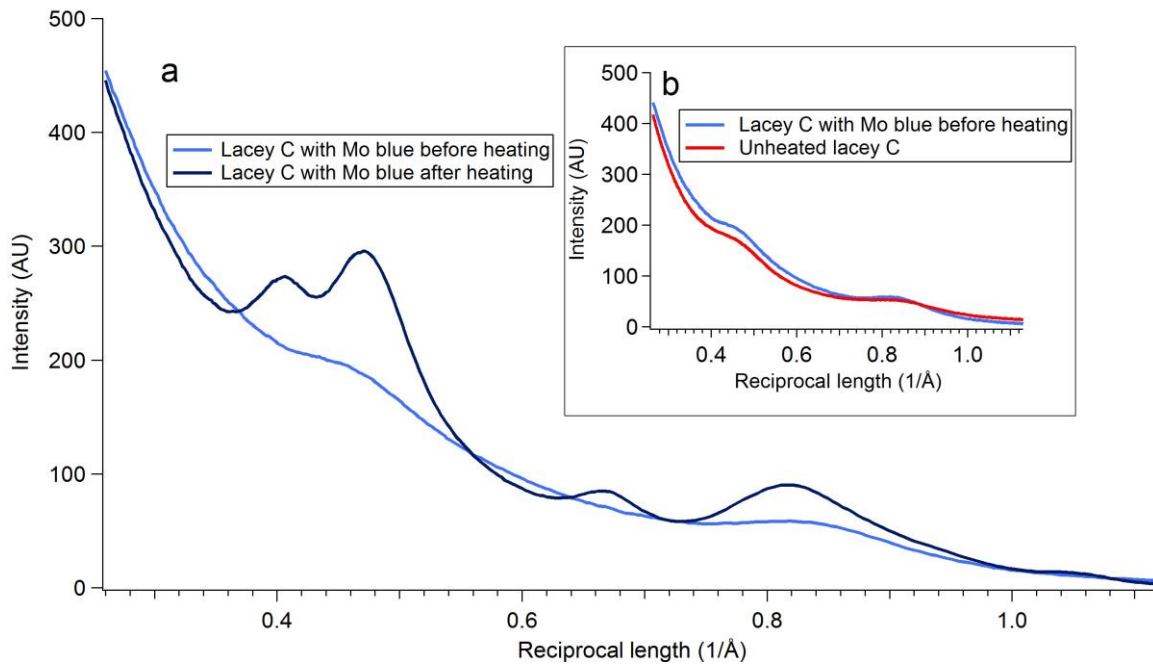


Figure 49: a) Intensity profiles of SAED of lacey C film exposed to Mo blue solution shows two broad peaks at room temperature (blue line) that are replaced by four diffraction peaks after heating (black line); b) Normalized intensity profiles of SAED of unheated lacey C with (blue line) and without (red line) Mo blue show great similarity in level of initial disorder.

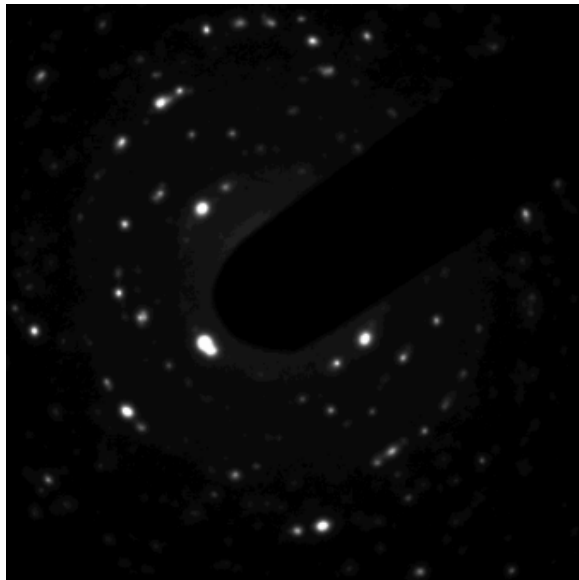


Figure 50: SAED of region A2 in lacey carbon with molybdenum blue after heating

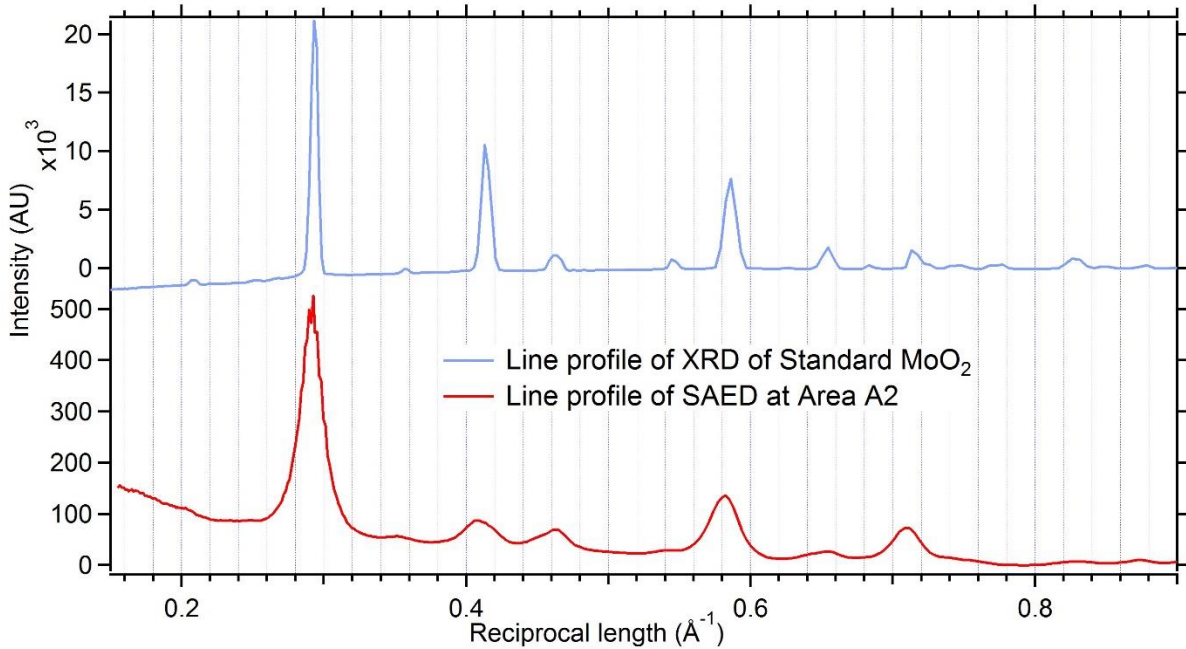


Figure 51: Integrated line profile of SAED from region A2 in sample (fig 50 ) compared with XRD line profile of standard MoO<sub>2</sub>

After heating, the broad amorphous rings become sharper and more intense with peak positions corresponding to real space distances of 0.213 nm and 0.123 nm, matching the {100} and {110} planes of graphene, respectively. Additional rings that correlate with real space distances of 0.246 nm and 0.148 nm are detected (fig 48b), consistent with formation of graphene monoxide [27]. *In-situ* heating produces local variations in temperature, necessitating exploration of multiple regions on the same sample. While the data shown above is representative of most observed regions, some sample regions like A2 (fig 45,50,51) show additional diffraction rings that can be indexed as monoclinic MoO<sub>2</sub> indicative of changes in oxidation state during the heating process.

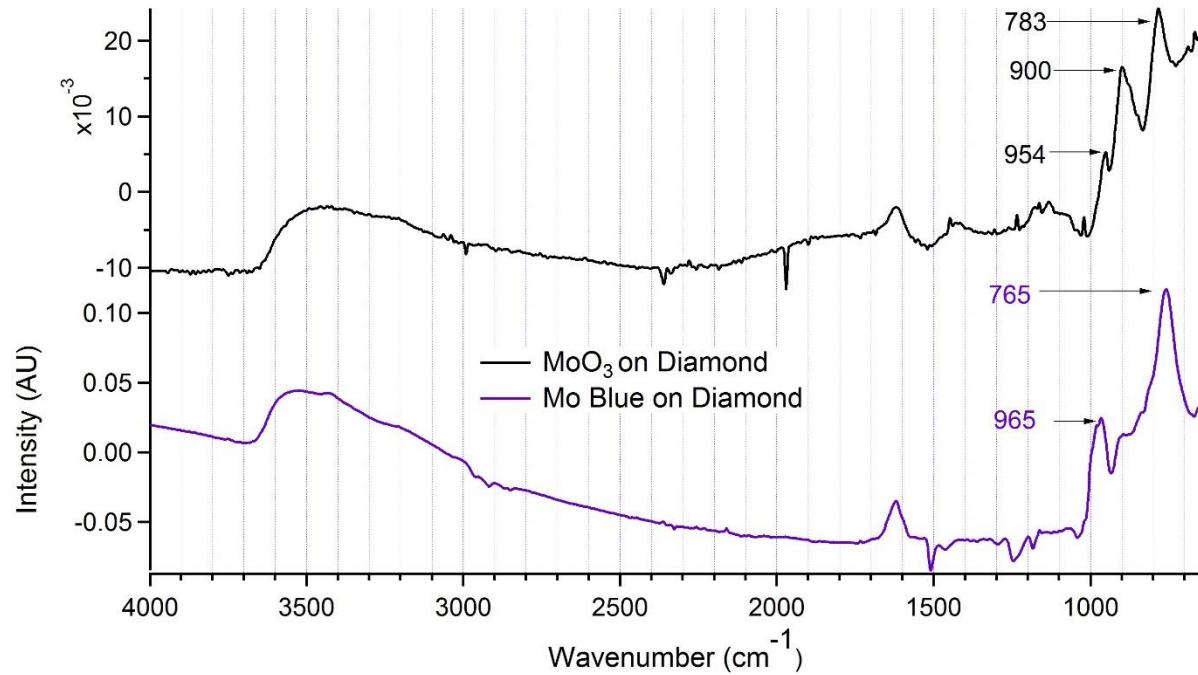


Figure 52: IR spectrum of Mo blue solution dried on diamond window compared with MoO<sub>3</sub> solution also dried on diamond window

#### 5.4 Discussion:

The BF image (fig 44a) of the lacey carbon film with Mo<sub>x</sub>O<sub>y</sub> solution is clearly different from a typical lacey carbon film (not shown here), with in homogeneities in thickness, especially at the edges, and wrinkles and distortions. This suggests that the soluble oxide of molybdenum interacts with amorphous carbon, modifying the morphology and composition of the lacey carbon film. Areas similar to A1 are lacey carbon with a small amount of precipitate of Mo oxide and a large amount of carbon as detected by EDX (figs 46 and 47). The interaction of Mo blue solution with lacey carbon on heating converts lacey carbon into graphene as evidenced by detecting graphene rings (figs 48b and 49). Diffraction rings are observed instead of diffraction spots because layers of graphene formed in amorphous carbon are randomly oriented in two dimensions. Also circular average line intensity profile of the SAEDs, in fig 49a shows peaks for



graphene along with peaks for GMO. Apart from the peak developments, the intensity profile backgrounds for lacey carbon exposed to Mo blue solution are similar before and after heating for SAED that were taken at same region. Fig 49(b), shows circular average intensity line profiles of SAED from Area A1 exposed to Mo blue and from another lacey carbon film with similar thickness. As the two experiments were done with two different currents in the TEM, the intensity of Lacey carbon is normalized with that from area A1 at the initial scattering angle. Since Mo has higher scattering amplitude than that of C, its scattering amplitude is higher, decreases sharply and ends up higher than that for C with increase in scattering angle. This trend is observed in fig 49b that compares the two SAED line profiles for the Lacey Carbon to the Lacey Carbon with Mo solution. They are normalized in the beginning and the intensity for Lacey C with Mo blue remains higher for most of the scattering angles.

The mechanism to describe the effects we have seen is discussed here. We suggest that the Mo blue solution acts as a catalyst and is capable of removing distortion and defects within layers of amorphous lacey carbon and forms graphene as heat is employed. After heating to a relatively low temperature of 600°C defined diffraction graphene rings are observed. No additional rings that can be attributed to carbides are detected. According to [70], a graphitizable carbon possesses well-ordered lamellar type molecules but graphitization is prohibited due to defects or distortions within the lamellae and in the stacking sequences of these lamellae. Gillot et al. [71] suggest that an oxidation process may eliminate these defects and form graphite. During carbothermic reduction of Mo oxide having higher oxidation state such as  $\text{MoO}_3$ ,  $\text{MoO}_2$  is formed at around 400-700°C [36]. In the present case during higher heating in vacuum molybdenum dioxide is detected (Area A2) in SAED. IR measurement done on lacey carbon

with Mo blue solution shows strong Mo-O stretching peak similar to that of MoO<sub>3</sub> before heating, but after heating it disappears as MoO<sub>2</sub> so formed doesn't show any strong peak. For comparison, IR spectra of Mo blue with Molybdic acid is shown in fig 52. Mo blue shows unique but still very much similar IR spectra to that of molybdic acid. Both shows presence of water molecule (3500 cm<sup>-1</sup> -OH stretching modes and 1625 cm<sup>-1</sup> -OH bending mode). Mo-O stretching modes in molybdic acid (954 and 900 cm<sup>-1</sup>) are both red shifted by 24 cm<sup>-1</sup> compared to trimer of MoO<sub>3</sub> [72]. The spectrum of Mo blue behaves similar to its precursor molybdic acid with some shifting except it has only shoulder at around 900 cm<sup>-1</sup>. Thus the Mo blue solution dissociated into Molybdenum dioxide and oxygen, and the formed oxygen removes defects between the original layers and forms graphene.

Table 1: Comparison of spacing of diffraction rings formed in Lacey carbon and GO

G and GMO ring (from literature [27] )	Lacey C rings	
	Before heating (nm)	After heating (nm)
I) 0.123 nm(G)	0.123 ± 0.01	0.123 ± 0.003
II) 0.213 nm(G)	0.210 ± 0.01	0.210 ± 0.006
III) 0.260 nm(GMO)	-	0.246 ± 0.006
IV) 0.152 nm(GMO)	-	0.148 ± 0.003

## 5.5 Conclusion:

Here, it is shown that graphene and graphene monoxide can be formed from amorphous carbon and a soluble oxide of molybdenum that are heated in high vacuum at temperatures in excess of 600°C. The catalytic thermal method demonstrated here can be an effective alternative to

convert amorphous carbon into crystalline graphene and graphene monoxide. Further studies of different ratios of C, Mo and O will be forthcoming to elucidate the interaction between these three components in more detail.

## Chapter 6 : Catalytic synthesis and structural characterization of Graphene

### Monoxide

Nanocomposite of Graphene monoxide and reduced graphene oxide are synthesized in a large scale (milligram) by heating the mixture of graphene oxide and molybdenum blue solution containing  $\text{Mo}_x\text{O}_y \cdot z\text{H}_2\text{O}$  at moderate temperature ( $650^\circ\text{C}$ ) in high vacuum ( $10^{-7}$  torr). Selected area electron diffraction and X-ray powder diffraction show evolution of graphene monoxide diffraction rings (at  $2.54 \text{ \AA}$  and  $1.47 \text{ \AA}$ ) after heating. Nanocomposite of reduced graphene oxide and graphene oxide are randomly oriented layered structure with spacing of about  $3.65 \text{ \AA}$ .

Keywords: EXAFS, XRD, SAED, IR, Bright field image, Dark field image

### 6.1 Introduction:

Graphene, a monolayer of graphite having two-dimensional (2D) hexagonal (honeycomb) structure of carbon atoms is of great interest because of its exceptional electrical, mechanical and thermal properties [73] [74] [75] [76] [77] [78]. However, graphene is a zero bandgap semiconductor and it can't have practical application in making semiconducting device [79]. Also manufacturing of graphene by mechanical exfoliation method is commercially not viable. Hence it is chemically functionalized to create tunable bandgap. GO is a graphene like material manufactured chemically by exfoliating graphite by modified Hummers process [80]. IR measurements on GO manufactured by Hummers method shows that it is composed of functionalized graphene sheets decorated by functional groups such as  $-\text{COOH}$ ,  $\text{C-O-C}$ ,  $\text{C=C}$  and  $\text{R-OH}$ . Nanoporous graphene and multilayered GO exhibits unlimited potential to be used as

membranes for desalination with 100% salt rejection [26]. However, GO doesn't have many other direct applications as it is non-stoichiometric, thermally unstable and a poor conductor of electricity [81].

A graphene based material, graphene monoxide (GMO) was first produced in a nanogram scale by thermal annealing of multilayered GO deposited at Mo grid in a TEM (Transmission emission microscope) [82]. GMO has centered-rectangular (quasi-hexagonal) lattice structure with two carbon atoms of graphene unit cell bridged by double epoxides with increase in lattice parameter to 3.09 Å (from 2.46 Å in graphene) and angle between them is 124° (from 120° in graphene) and 20% increase in planer area of the unit cell area [82]. First-principles calculations predict GMO as an intrinsic semiconductor with a bandgap of about 1eV, and by applying tensile uniaxial strain along zigzag direction it can be switched between indirect and direct semiconductor with tunable bandgap (0-1.3 eV) and this tunable electronic properties of GMO could find potential application in future semiconductor devices [83]. The strong anisotropic nature of direct bandgap GMO causes electrons and holes to preferentially move along the zigzag and armchair directions, respectively, minimizing the rate of recombination between electrons and holes, making it desirable material for photovoltaic devices and also the oxygen atom in GMO could act as adsorption sites and making it potential candidate in sensors and lithium ion battery applications [83].

According to DFT calculations, all the possible sequences of the GMO bilayer show the typical interlayer bonding characteristics of two dimensional bilayer systems with a weak van der Waals interactions. Band gap energy of bilayer GMO (0.418-0.448 eV) is slightly smaller than that of the monolayer (0.536 eV). These band gaps are suitable for making electric device application.

Band gap of bi-layer GMO is external electric field sensitive and at small critical electric field ( $E_c=0.22-0.30$  V/Å) semiconductor to metal transition occurs. Hence bilayer GMO is the strong candidate for nanoelectronics [84].

## 6.2 Experimental methods

### 6.2.1 Molybdenum blue solution preparation

200 mg of  $\text{MoO}_3$  powder (Sigma Aldrich) was mixed with 200 ml of de-ionized water for a couple of days at room temperature and pressure. Clear solution (molybdic acid) was separated to another beaker and 100 gm of Mo metal powder ( $< 150$   $\mu\text{m}$  diameter) (Sigma Aldrich) was added to the molybdic acid at room temperature and pressure. Immediately, the solution turned blue and became deep blue in a couple of days. Finally, the solution (Mo blue) was also separated from Mo powder.

### 6.2.2 Nanogram scale: Reduction of GO/Mo blue deposited on Ni TEM grid:

GO (10mg/ml) synthesized by modified Hummers method was purchased from ACS nano and was mixed with Mo blue solution in the ratio 1:2 by volume. The mixture was diluted by mixing with de-ionized water in the ratio 1:10. Diluted GO 2  $\mu\text{l}$  of the mixture was drop casted onto 300 mesh Ni TEM grid and dried in air, to form self-supporting, multilayered GO/Mo blue sample. *In situ* heating of sample was done using a Gatan tantalum-cup heating holder inside a Hitachi H9000NAR pressure TEM operating at an accelerating voltage of 300 kV, at a constant column pressure of  $10^{-7}$  Torr. Gatan Orius SC CCD was used for capturing high resolution images, selected area electron diffractions (SAEDs), bright and dark field images. The sample in TEM grid was *in situ* heated at the rate of about  $30^\circ\text{C}$  per minute up to  $650^\circ\text{C}$ . IR measurement was

done on the same sample before and after *in-situ* heating using Bruker Hyperion 3000 IR Microscope using MCT detector.

### 6.2.3 Milligram scale: Reduction of GO and Mo blue solution

10ml of GO (10mg/ml) and 20 ml of Mo blue solution were mixed uniformly by sonicating the mixture for an hour. The mixture was poured into 3 cavities of silicone "Slide Duplicating Mold" each 1" x 3" x 3/32" (Electron Microscopy Sciences). After drying the mixture at room temperature and pressure, thin dark GO/Mo blue paper was obtained. The paper like sample was transferred to Alumina coated tantalum boat (3" x 3/4" x 3/8"). The boat was heated (Joule's heating) at pressure of  $8 \times 10^{-6}$  torr, with constant rise of current (1 amp/min) from room temperature to 280°C in 32 mins at about 8°C/min then held constant for 30 mins to keep the pressure below  $1.2 \times 10^{-5}$  torr. The current flowing through the boat and potential difference across it were measured to calculate temperature of boat and correlated to temperature measured from a radiation pyrometer above 550°C. Residual gas analyzer(RGA) was used to analyze gas released during heating. The boat was further heated very slowly up to 290°C while keeping the constant pressure (below  $1.2 \times 10^{-5}$  torr) by increasing current by 4 amp in 70 mins. Current through boat was increased by 1amp/min for another 6 mins to reach temperature of 340°C. At 340°C there was second burst in pressure ( $3.0 \times 10^{-5}$  torr), so heating was stopped for another 6 mins. After that the boat was again heated at 1 amp/min till 650°C at 5°C rise in temp per min in 70 mins and stayed at the temp for another 10 mins.

After reaching 650°C in 165 minutes, the current was terminated and the sample was allowed to cool. The heated sample of less than 1mm diameter was crushed with a mortar and pestle and

formed a powder that was dispersed in methanol. For TEM measurements, a drop of mixture with methanol was dropped on 300 mesh Ni grid with lacey carbon and dried in air. The remaining annealed sample was crushed into powder and filled into amorphous glass capillary tube of length 10 cm and internal diameter of 1 mm for X-ray powder diffraction measurement near Mo-K edge (19.95 keV) using Pilatus 100k Detector and X-ray absorption spectroscopy (XAS) measurement around Mo-K edge (20 keV) using ion chambers (nitrogen filled) at beamline 12BM, Advanced Photon Source (APS) at Argonne National lab Chicago, IL. About a mm diameter of paper like heated sample was crushed and sprayed over diamond window for infrared measurement. To compare XRD and XAS of the standard  $\text{MoO}_2$ ,  $\text{MoO}_3$ ,  $\text{Mo}_2\text{C}$  powder (Sigma Aldrich) were spread on Kapton tape were also collected. For IR measurement, tiny amount the powder was spread over diamond window, and measured in a Bruker Hyperion 3000 IR Microscope using MCT detector. Two dimensional SAED and XRD pattern were reduced into one dimensional by using Nika software [85]. X-ray absorption spectroscopy (XAS) data were processed by using Athena software and EXAFS data were fitted by Artemis using theoretical standards from FEFF [86].



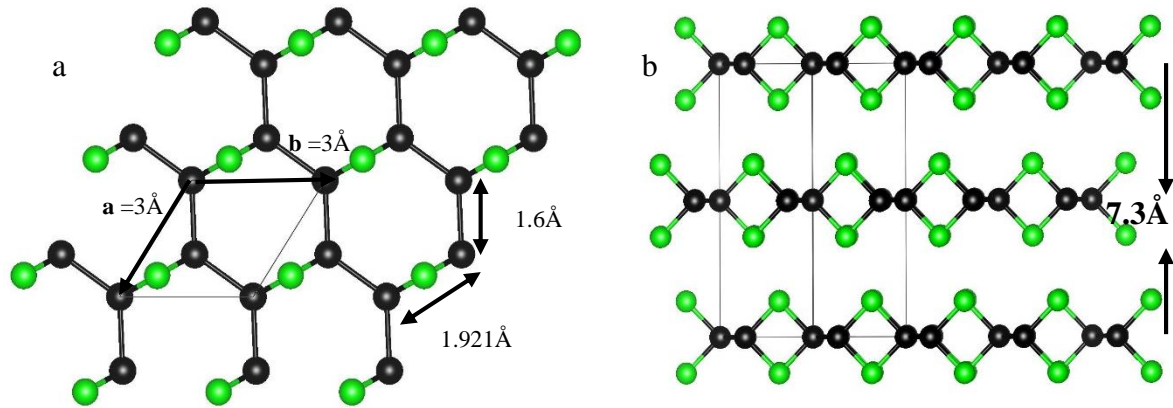


Figure 53:(a) Unit cell of two dimensional GMO (top view) with lattice vectors  $\mathbf{a}$  and  $\mathbf{b}$  equal to  $3 \text{ \AA}$  and angle between them equal to  $122.64^\circ$ . (b) Model of 3D GMO in which GMO layers are in AB stacking (side view) similar to graphite having separation of  $7.3 \text{ \AA}$  between alternate layers.

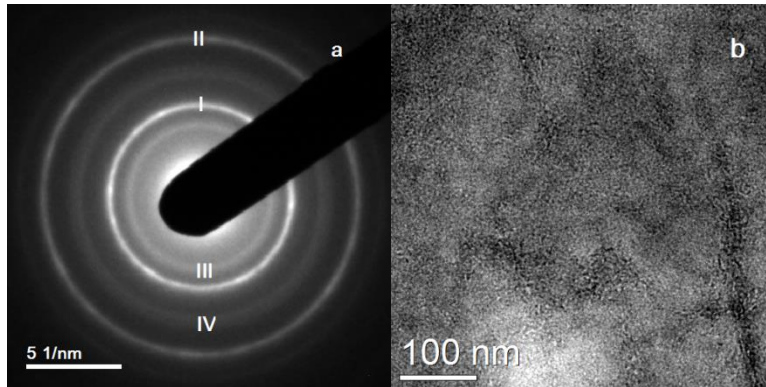


Figure 54: (a) SAED of nanogram scale GO/GMO composite after in-situ heating GO and Mo blue mixture in Ni TEM grid. Ring I and II are diffraction rings due to graphene ( $2.13 \text{ \AA}$  and  $1.23 \text{ \AA}$  due to graphene planes (100) and (110) respectively). Rings III and IV are GMO rings which starts to form after  $550^\circ\text{C}$  during in-situ heating ( $2.68 \text{ \AA}$  due to (100) and (1-10) GMO planes and  $1.54 \text{ \AA}$  due to GMO (110)). (b) Bright field image of GO/GMO composite from where SAED pattern was obtained.

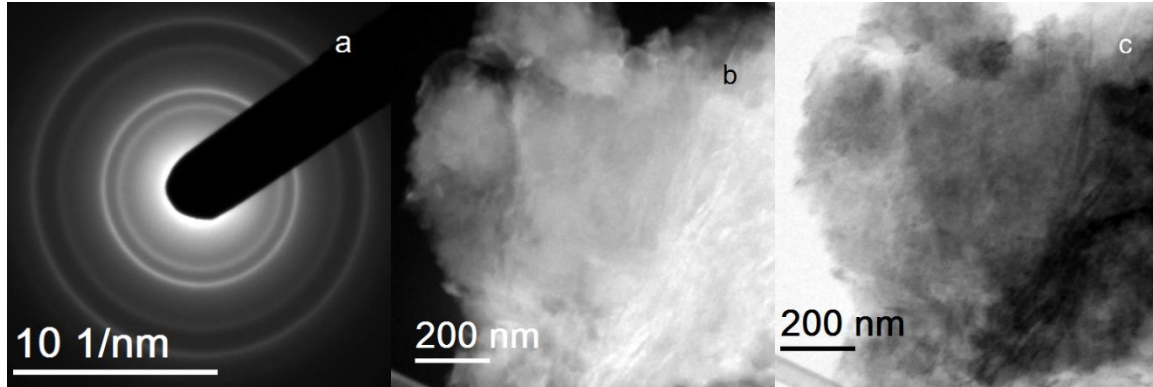


Figure 55: Milligram scale: (a) SAED of milligram scale GO/ GMO composite showing rings similar to that in nanogram scale, (b) bright field image and (c) dark field image

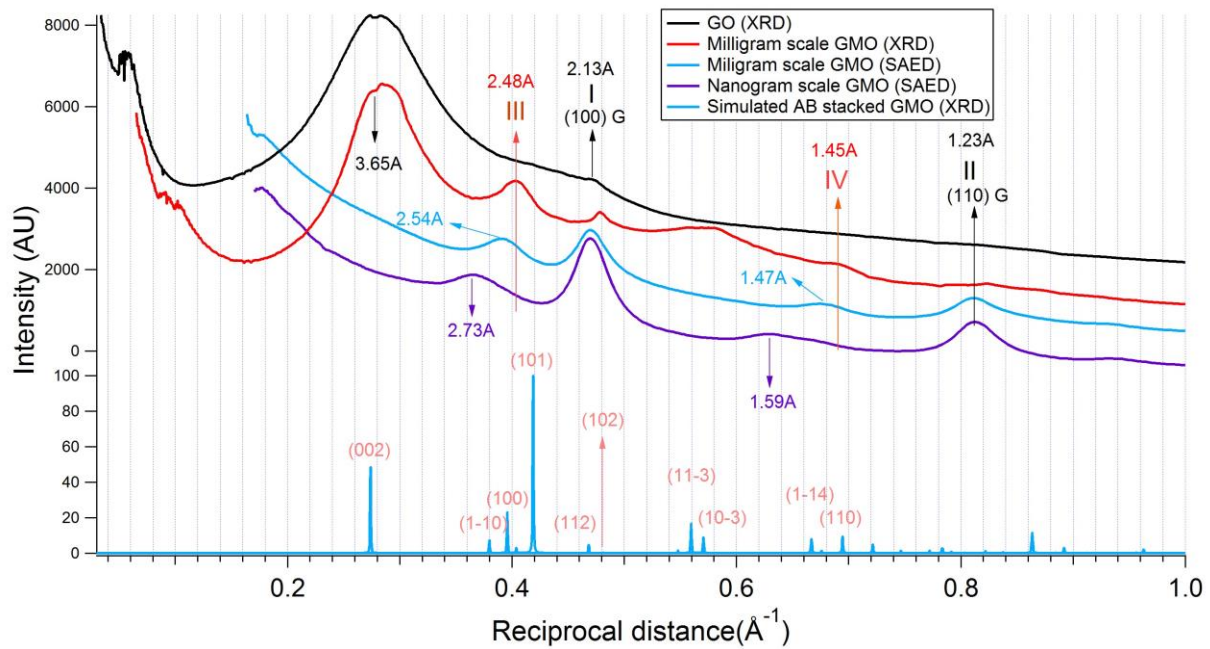


Figure 56: XRD and SAED diffraction integrated line profile of r-GO/GMO nanocomposite (milligram scale) in reciprocal distance compared with r-GO/GMO nanocomposite (nanogram scale) and simulated AB stacked GMO using X-ray powder diffraction

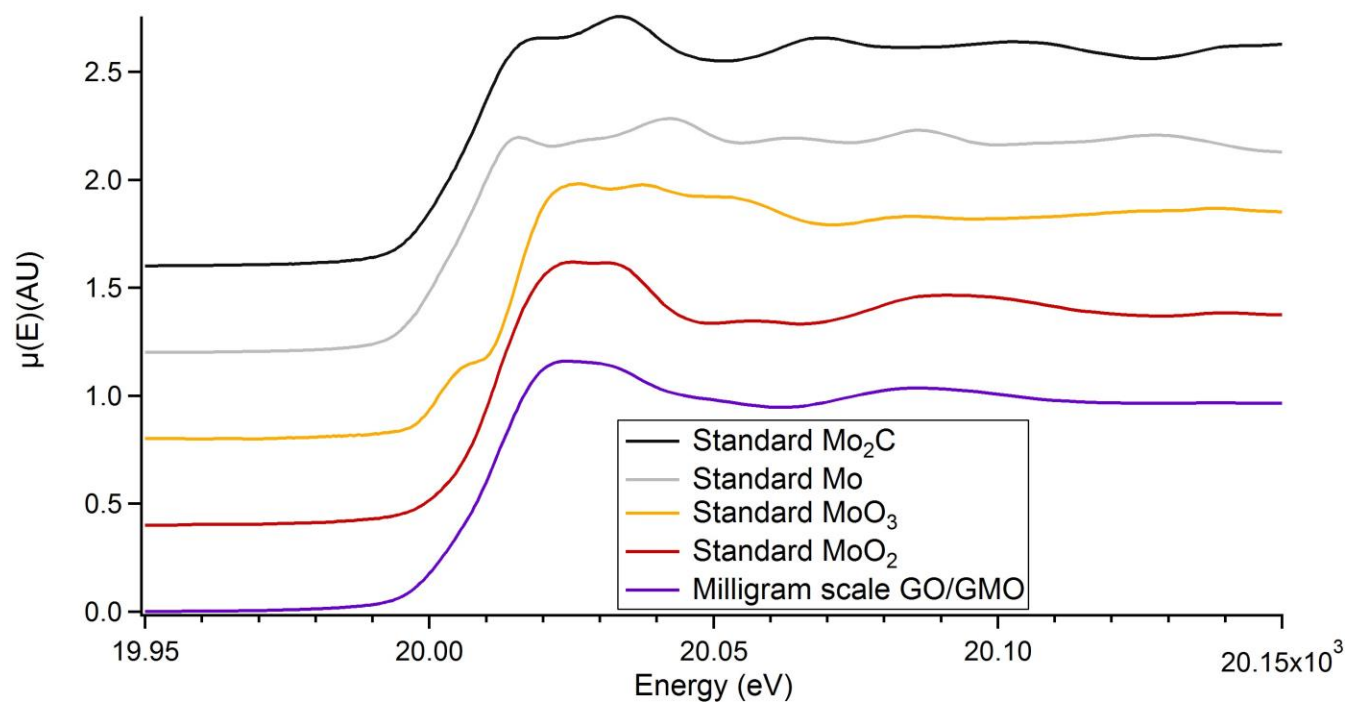


Figure 57: Comparison of XANES of r-GO/GMO sample (milligram scale) with standard Mo<sub>2</sub>C, Mo metal powder, MoO<sub>3</sub> and MoO<sub>2</sub> powder. All of the XANES plots are stacked along vertical axis.

Table 2: Pre-edge and Edge peak energies of Mo, Mo<sub>2</sub>C and Mo-oxides with milligram scale GO-GMO

Sample	Pre-edge, (eV)		Edge Energy, E <sub>o</sub> (eV)	
	Experimental	[87]	Experimental	[87]
Mo powder	Absent	Absent	20008.5	NA
Mo foil (reference)	Absent	Absent	20009.5	20008.1
Mo <sub>2</sub> C	Absent	Absent	20008.5	NA
MoO <sub>3</sub>	20001.5	20004.9	20015.5	20013.6
MoO <sub>2</sub>	Absent	Absent	20012.0	20011.5
Milligram Scale GO-GMO	Absent	Absent	20012.0	NA

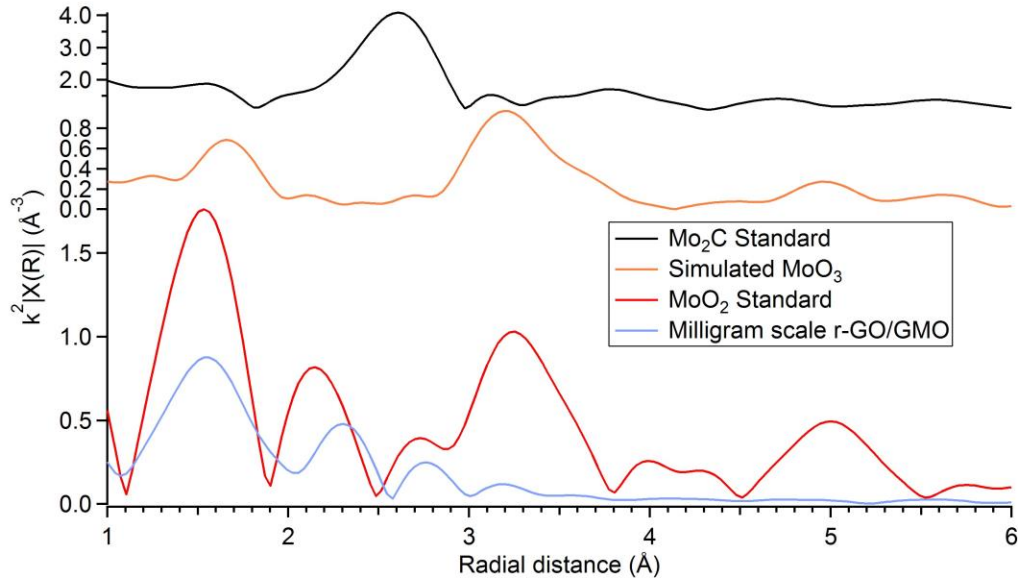


Figure 58: Milligram scale: (From bottom) Fourier transform of  $\chi(k)$  of milligram scale GMO and standard MoO<sub>2</sub>. The first peak at 1.5  $\text{\AA}$  is due to back scattering of photoelectron wave from nearest 6 oxygen atoms of the reference Mo atom. The second, third and fourth peaks from left are mainly due to scattering of the wave from first (1 Mo atom), second (1 Mo atom) and third (8 Mo atoms) nearest Mo neighbors respectively. The EXAFS shows very much similar structure of MoO<sub>2</sub> and Milligram scale r-GO/GMO, but in short range. Also simulated EXAFS of MoO<sub>3</sub> and EXAFS of experimental Mo<sub>2</sub>C are presented for comparison.

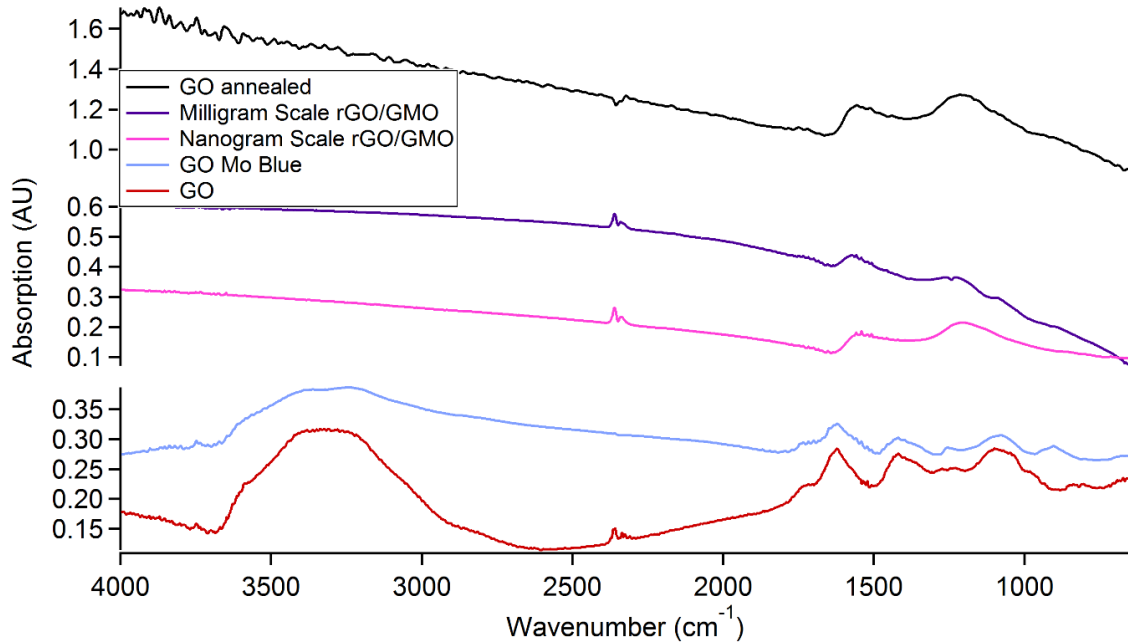


Figure 59: IR spectrum of (From bottom) GO, mixture of GO and Mo blue solution, nanogram scale r-GO/GMO, milligram scale r-GO/GMO and nanogram scale r-GO.

## 6.3 Results and discussions:

### 6.3.1 TEM measurement:

a. **Nanogram scale:** SAED performed on the sample (fig 54 a) shows diffraction rings due to graphene planes (100) spacing 2.13 Å (Ring I) and (110) spacing 1.23 Å (Ring II) before heating and addition of two more rings due to the formation of GMO after reaching temperature of 550°C spacing 2.68 Å (Ring III) due to GMO planes (1-10) and (100), and 1.54 Å (Ring IV) due to GMO plane (110). The measured real spacings of graphene rings are consistent with corresponding spacings in graphene or graphite, however real spacing of both Ring III and IV due to GMO are larger than spacing of 2.60 Å and 1.52 Å respectively as mentioned in [82] for GMO. Small increment in the real spacing of diffraction rings of GMO is due to high flexibility in length of lattice vectors and angle between lattice vectors in the unit cell of GMO. In graphene bond between carbon atoms is rigid so the real spacing of diffraction rings due to its planes are always constant. However, in case of GMO, DFT theory has predicted bridging bond of double epoxide between carbon atoms in GMO can be highly flexible with small stress. Nanogram scale r-GO/GMO composite is only few layered and the GMO unit cell exist in relaxed state with minimal strain. Fig 54 b is the bright field image corresponding to SAED shown in fig 54 a. The image doesn't show much change in contrast of the sample during heating.

b. **Milligram scale:** SAED of milligram scale r-GO/GMO (fig 55 a) composite doesn't look much different than that of nanogram scale. Real spacing of diffraction Rings I and II due to graphene are exactly same as expected but real spacing of the Rings due to GMO are decreased to 2.54 Å (Ring III) and 1.47 Å (Ring IV) in SAED. These real spacing of Ring III and IV were used to calculate lattice parameters and a GMO model is obtained (fig 53 a). Dark field and

bright field image corresponding to the SAED pattern in fig 55 b and 55 c shows uniform material with homogenous contrast.

### 6.3.2 XRD Measurement:

Powder-XRD pattern of milligram scale r-GO/GMO composite is compared with its own SAED, its precursor unheated GO and simulated XRD pattern of two dimensional planes of GMOs arranged in AB stacking in fig 56. As TEM sample is very thin and its planes are always oriented perpendicular to the electron beam, its SAED pattern is formed only due diffraction from its Miller planes parallel to c-axis. Whereas during powder XRD measurement, powdered samples are randomly oriented, so XRD pattern shows all possible diffraction planes including Miller planes perpendicular to c-axis of crystal.

XRD of unheated GO and r-GO/GMO composite have huge broad peak at  $3.65 \text{ \AA}$  ( $0.274 \text{ \AA}^{-1}$ ) (fig 56), is due to interplaner spacing between GO layers (or GMO layers), which is analogous to (002) peak in graphite. This diffraction peak is forbidden in SAED due to orientation of plane of the 2D crystals lying perpendicular to electron beam. XRD peak due to (100) graphene plane in unheated GO and SAED peak due to milligram and nanogram scale r-GO/GMO are exactly positioned at  $2.13 \text{ \AA}$ . In contrary, the corresponding XRD peak of milligram scale r-GO/GMO is shifted to  $2.09 \text{ \AA}$ . This mismatching of (100) graphene peak in two diffraction techniques for the same milligram scale r-GO/GMO composite is an evidence of some sort of periodicity along c-axis in newly formed GMO crystals. Also the spacings of the Ring III and Ring IV in XRD of milligram scale r-GO/GMO are lowered to  $2.47 \text{ \AA}$  and  $1.45 \text{ \AA}$  respectively which are smaller than spacings obtained from SAED of the same sample. This shifting of peaks between two different diffraction techniques can only be explained if we consider periodic stacking of two

dimensional planes in vertical direction. r-GO or GMO planer crystals are randomly stacked together with periodicity for few layers in vertical direction. To understand the effect of periodicity of 2D crystals, a hypothetical 3D model of GMO (fig 53 b) is constructed with AB stacking (similar to graphite) having interplaner spacing  $3.65\text{\AA}$  obtained from XRD for r-GO/GMO (fig 56) and powder XRD simulation is obtained (fig 56). Also powder-XRD is simulated for 3D GMO model with middle layer of GMO translated with different distances along **a** and/or **b** directions (not shown here). Intensity of simulated powder-XRDs vary a lot with different types of stacking but the position of peaks remains unchanged. The comparison of experimental XRD and SAED of milligram scale r-GO/GMO composite with simulated powder-XRD in fig 56 shows shifting of XRD peaks for Ring III and Ring IV are due to presence of diffraction peak due to (101) and (102) planes respectively.

As one of the precursor Mo blue used in making the sample r-GO/GMO is an amorphous oxide of Mo, the XRD pattern of milligram scale r-GO/GMO was compared with available JCPDS files of oxides and carbides of Mo (not shown in fig). None of the available JCPDS files match with XRD of the sample and it shows absence of any crystalline form of Mo compound present in the milligram scale nanocomposite.

#### **XAS measurement:**

To understand the structure of Mo compound present in the composite of r-GO/GMO, XANES (fig 57) and EXAFS (fig 58) of the composite were compared with standard oxides and carbide of Mo. Standard  $\text{MoO}_3$  has strong pre-edge peak at  $20001.5\text{ eV}$  and similar pre-edges are also observed in sub-oxides of Mo such as  $\text{Mo}_4\text{O}_{11}$ ,  $\text{Mo}_5\text{O}_{14}$ ,  $\text{Mo}_8\text{O}_{23}$  and  $\text{Mo}_{18}\text{O}_{52}$  [88] but absent in  $\text{Mo}_2\text{C}$ , Mo metal and  $\text{MoO}_2$ . XANES as well as EXAFS of the GMO composite is very much

similar to that of MoO<sub>2</sub> (fig 57 and 58). XANES analysis done for the GMO composite shows that more than 85% of the sample is MoO<sub>2</sub> and only about 10% of the sample may have MoO<sub>3</sub>. Also edge of MoO<sub>2</sub> and the sample are same. The EXAFS analysis done on milligram scale sample shows structure similar to MoO<sub>2</sub> within short range.

### 6.3.3 IR measurement:

Change in bonding or chemistry during heating was examined by IR measurement in normal incidence transmission mode. The mixture of GO and Mo blue showed IR peaks due to functional groups hydroxyl (3300 cm<sup>-1</sup> and 1625 cm<sup>-1</sup>), carbonyl (1708 cm<sup>-1</sup>), carboxyl (1425 cm<sup>-1</sup>), epoxide (1245 cm<sup>-1</sup>) and alkoxy (1080 cm<sup>-1</sup>) and C=C stretching (1580 cm<sup>-1</sup>) including Mo-O stretching (900 cm<sup>-1</sup>) due to Mo blue compound (fig 59). After annealing hydroxyl, carbonyl, carboxyl, alkoxy peaks vanishes from the sample making it hydrophobic. Also Mo-O stretching peak disappears indicating chemical change in Mo blue composition. However, C=C (1560 cm<sup>-1</sup>) stretching remains an asymmetric fano line shape, activated due to the defects. Also epoxy peaks (1215 cm<sup>-1</sup>) is red shifted after heating.

### 6.3.4 Conclusion:

We have demonstrated a thermal reduction method for the nanogram scale as well as milligram scale production of r-GO and GMO nanocomposite in high vacuum. Our XRD measurement performed on milligram scale nanocomposite also demonstrated, so formed GMO is multilayered with interlayer spacing similar to its precursor GO about 3.65Å. We found the lattice vectors and angle between them for 2D unit cell of multilayered GMO is lowered to 3Å and 122.64°, which



is due to the stress applied on GMO crystal due to stacking. Small variation in lattice parameters were observed for both nanogram scale as well as milligram scale nanocomposites, which are consistent with the prediction made by DFT theory for highly flexible bonding between carbon and oxygen atoms. EXAFS and XANES analysis performed on the material confirmed the formation of amorphous MoO<sub>2</sub> along with r-GO and GMO. These amorphous MoO<sub>2</sub> molecules have very short range of periodicity ( $\sim 3 \text{ \AA}$ ) and hence they are not observed in TEM imaging and also don't show any diffraction.

### 6.3.5 Acknowledgements

We thank Dr. Sungsik Lee and Benjamin Reinhart for their assistance during the experiments conducted at 12-BM-B of the Advanced Photon Source. This work and the use of the Advanced Photon Source, a U.S. Department of Energy (DOE) Office of Science User Facility at Argonne National Laboratory, are supported by the U.S. DOE, Office of Science, Office of Basic Energy Science, Division of Chemical Sciences, Biosciences and Geosciences, under Contract No DE-AC02-06CH11357.

## Chapter 7 : Formation of graphene monoxide by electron bombardment and *in situ* heating mixture of graphene oxide and chromium trioxide

As a part of finding new ways of making GMO using different catalytical methods, GMO was successfully prepared by *in situ* electron bombardment (300 keV) of the mixture of GO and chromium trioxide in TEM ( $10^{-7}$  torr of pressure) at room temperature. *In situ* SAED showed that further heating of sample favors in removing amorphous background and improve crystalline quality at very low temperature of 250°C. SAED performed with tilted sample confirms so formed GMO is two dimensional.

### 7.1 Introduction

After successfully synthesizing of GMO/r-GO composite from GO in presence of Mo metal (grid, wire or powder), MoO<sub>3</sub> solution and Mo blue solution, we tried to make GMO using transition metals similar to molybdenum. The first choices were easily available transitional metals such as Ni, Cu, Au and Pt which have been well known for their catalytic properties for very long time. However, none of these metals were useful in making GMO. Then we decided to use metal in the same group of periodic table with Mo. Dr. Schoefield, heated mixture of tungsten wire and GO in Ni grid. But GMO wasn't formed with tungsten. Later, similar experiments were performed with oxides of chromium. The easily available oxides of chromium are chromium (VI) oxide (CrO<sub>3</sub>) and chromium (III) oxide (Cr<sub>2</sub>O<sub>3</sub>). Among these two oxides, CrO<sub>3</sub> was a better choice because it is very much similar to MoO<sub>3</sub> as both of them have similar formula and have strong oxidizing strength. CrO<sub>3</sub> was a better choice also because of its high

solubility, unlike  $\text{MoO}_3$  which is sparingly soluble in water.  $\text{Cr}_2\text{O}_3$  wasn't a good choice as it wasn't soluble and doesn't have any oxidizing property. Process of formation of GMO with two different concentrations of  $\text{CrO}_3$  is explained in the following section.

## 7.2 Experimental:

1%  $\text{CrO}_3$  was prepared by dissolving  $\text{CrO}_3$  crystals with de-ionized water. GO (10mg/ml) synthesized by modified Hummers method was purchased from ACS nano. Two different samples were prepared by mixing GO and  $\text{CrO}_3$  solution in different ratio.

Sample1: GO (10mg/ml) and 1%  $\text{CrO}_3$  were mixed in the ratio 1:2 and a drop from the mixture was drop casted onto 300 mesh Ni TEM grid and dried in air to form self-supported multilayered sample.

Sample2: 0.4 ml of GO (10mg/ml) and 0.2 ml of 1%  $\text{CrO}_3$  were mixed (GO: 1%  $\text{CrO}_3 = 2:1$ ), further diluted by adding 2 ml of water. A drop from the mixture was drop casted onto 300 mesh Ni TEM grid and dried in air for a day to form self-supported multilayered sample.

*In situ* heating of sample was done using a Gatan tantalum-cup heating holder inside a Hitachi H9000NAR pressure TEM operating at an accelerating voltage of 300 kV, at a constant column pressure of  $10^{-7}$  Torr. Gatan Orius SC CCD was used for capturing the bright field image, dark field image and selected area electron diffraction.

## 7.3 Results:

When Sample1 was exposed to electron beam of 300 keV, it initially had only two diffraction rings (Ring I and II) due to graphene corresponding to planes (100) and (110) as shown in fig 60 (a). Diffraction rings were broad and have amorphous background probably due to poor

crystallinity and thickness of sample. During acquisition of SAED pattern, two more rings emerged having real spacing 0.258 nm and 1.49 nm (Rings III and IV in fig 60) quite close to spacing of GMO rings as described in literature [27]. During heating intensity of diffraction rings slightly improved throughout the sample and attained saturation at temperature less than 250°C. SAED taken nearby the same region at 659°C is also shown in fig 60(b) and it shows slightly

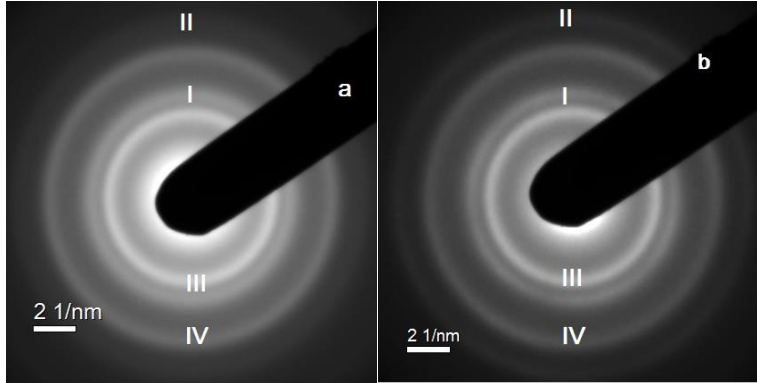
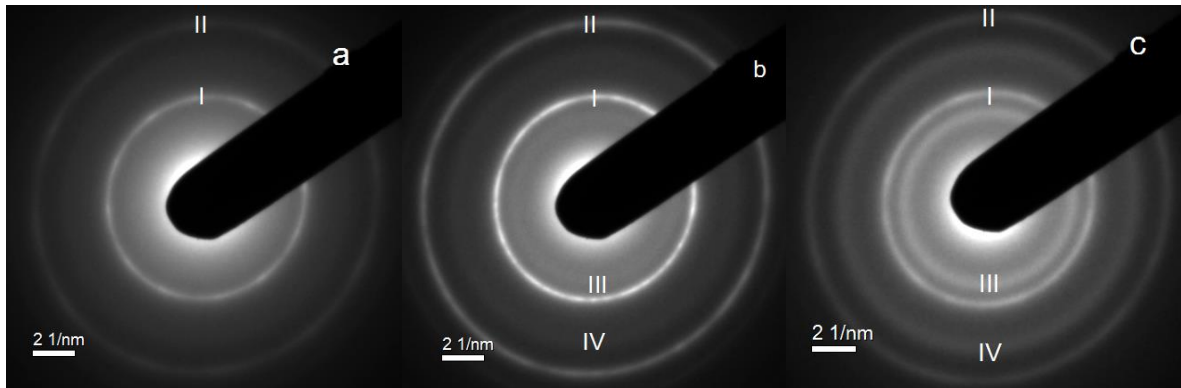


Figure 60: (a) SAED of Sample1, right after exposure to electron beam, showing diffraction rings due to Graphene (Rings I and II) and GMO (Rings III and IV) (b) SAED at another region at temperature 659°C also showing diffraction rings due to Graphene and GMO



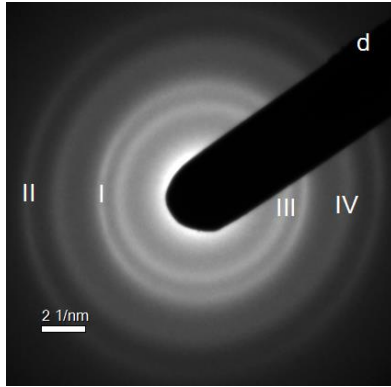


Figure 61: SAED of Sample2 (a) SAED at region 1 before heating showing ring I and II (b) SAED at region 1 at 601°C showing bright ring I and II and faint ring III and IV. (c) SAED at region 2 showing brighter rings I, II, III and IV. (d) SAED at region 3 with sample2 tilted at 15° resulting in blurring of diffraction rings at top and bottom compared to sides.

sharper diffraction rings with less background.

Effect of electron beam on Sample2 was negligible. Layers of GO formed on grid was thin and had lower concentration of CrO<sub>3</sub>. Region 1 having comparatively thin and bright diffraction rings I and II due to graphene were chosen for *in situ* SAED (fig 61 a) and it started forming diffraction rings III and IV after heating above 100°C. All the rings continued to grow brighter and thinner with increase in temperature. SAED of the same region 1 at 601°C is shown in fig 61 (b) with faint ring III and IV. However, there were areas which were previously thicker before heating showed brighter rings I, II, III and IV at 601°C (fig 61 c). Sample2 in the grid was tilted to see its effect on diffraction pattern. Fig 61 (c) has depicted blurring of all the rings during tilting by 15°.

#### 7.4 Discussion:

Sample1 had greater thickness (because of less amount of water) and larger concentration of highly reactive (oxidizing) CrO<sub>3</sub>. When electron beam with 300 keV bombarded sample, it might have dissociated some CrO<sub>3</sub> releasing highly reactive atomic oxygen. This atomic oxygen might

have selectively oxidized graphene oxide to form GMO. Formation of rings III and IV in fig 60 (a). Increase in temperature helps in removing water and other functional groups responsible for amorphous background, so heating favored the formation of brighter rings in fig 60(b).

However, in Sample 2, sample on grid was thin layered (diluted sample) and had less concentration of  $\text{CrO}_3$  so only electron bombardment wasn't enough to create enough GMO, so the diffraction rings III and IV were almost invisible in fig 61 (a). Even heating to  $601^\circ\text{C}$  couldn't produce bright rings of GMO (fig 61 b). But at thicker region, which had higher amount of  $\text{CrO}_3$  intercalated between the layers of GO, showed brighter GMO rings after heating to  $601^\circ\text{C}$  (fig 61 c). To confirm, 2D nature of GMO, the sample was tilted (fig 61 d) and as expected both graphene and GMO rings blurred at top and bottom.

## 7.5 Conclusion:

With electron bombardment and *in situ* heating at lower, two dimensional GMO was formed from mixture of GO and  $\text{CrO}_3$ . The catalyst  $\text{CrO}_3$  is not only alternative to previously used catalyst Mo,  $\text{MoO}_3$  and Mo blue but also more efficient in producing GMO from GO. Our work (tilting SAED experiment) also supports GMO as a two dimensional structure of only carbon and oxygen, and our method of electron bombardment might be useful in making large amount of GMO for nano electric devices.

## Chapter 8 : Synthesis of Molybdenum dioxide/reduced GO nano-composite

Homogeneous nanocomposite of molybdenum dioxide/reduced-graphene oxide ( $\text{MoO}_2/\text{r-GO}$ ) was successfully synthesized by solution based method, mixing GO and Mo blue solution followed by heating at high vacuum ( $10^{-6}$  torr) at low temperature of  $650^\circ\text{C}$ . The tunable composition of nano-composite was prepared without using any surfactant and any toxic ammonia based chemical. The material was highly electrostatic and was characterized using TEM, XRD and EXAFS. Similar composite was also prepared inside TEM in nanoscale by heating GO deposited onto TEM Mo grid under similar conditions.

### 8.1 Introduction:

Graphene, a two dimensional, hexagonal, honey comb structure of carbon has attracted a lot of interest due to its unique electronic and mechanical properties [73] [74] [75] [76] [77] [78]. Mechanical exfoliation of graphite [74] [89] [90], carbon vapour deposition (CVD) [91] [92] [93] [94] and epitaxial growth on silicon carbide [95] [96] and ruthenium [97] are a few methods to produce pure and single layered graphene. But these methods are expensive for mass production. Chemical exfoliation of graphite using strong oxidizing agents, by modified Hummer's method is the cheapest method of synthesizing graphene like material called graphene oxide (GO) [80]. However, GO is insulating [91], non-stoichiometric and composed of functional groups such as epoxide, carbonyl, carboxyl and hydroxyl. These functional groups make GO hydrophilic and enables it to mix homogeneously with solutions of metal oxides. The mixture of GO and metal oxides can be reduced either chemically or thermally to obtain reduced graphene oxide (r-GO), which has large surface area with significant increase in conductivity

[98] [99].

MoO<sub>2</sub>, due to its distorted rutile structure possesses metallic conductivity ( $8.8 \times 10^{-5} \Omega \text{ cm}$ ) and has high melting point with high stability. Its metal like conductivity could also be attributed to its high density of states in the valence band energy region [100]. Thus MoO<sub>2</sub> is an excellent candidate for sensors, recording media, super capacitors, electrochromic devices and lithium-ion batteries [101]. MoO<sub>2</sub> has high theoretical specific capacity of 839 mAhg<sup>-1</sup> which is larger than theoretical specific capacity of traditionally used anode material, graphite (373 mAhg<sup>-1</sup>). Also the higher density of MoO<sub>2</sub> makes it a suitable material for LIBs [102]. However, bulk metal oxide electrodes pulverize during the volume change when taking Li ions, leading to rapid decay in capacity and limiting the potential use [103]. MoO<sub>2</sub> as nanomaterial composites with carbon nanoparticles, nanowires, nanorods, nanobelts, ultrathin nanosheets and complex assemblies have been engineered, and exhibit better performance in LIB due to higher surface areas, more active sites and shorter ion diffusion paths [104]. MoO<sub>2</sub>/r-GO nano composite has been reported for making supercapacitors [105], and for environmental friendly and noble-metal free catalyst for electrocatalytic hydrogen evolution reaction [106]. Ultrathin Carbon layer-coated molybdenum dioxide nanoparticles are used in near-infrared photothermal cancer therapy [107]. Nanoscale MoO<sub>2</sub> is of interest for important technological applications including catalysts for partial oxidation of hydrocarbons, solid oxide fuel cell anodes [108]. Reports for nano MoO<sub>2</sub> suggest high catalytic activity for the partial oxidation of Jet-A fuel with good resistance against coking and sulphur poisoning. It can also be used in development of internal reforming anode of Jet-A solid oxide fuel cell [109]. Carbon-supported molybdenum dioxide has been used in the oxidative desulphurization of thiophene [110].



Soluble ammonium heptamolybdate (AHM) [102] [111] or highly corrosive phosphomolybdic acid [112] is widely used as a precursor for MoO<sub>2</sub>. Highly toxic ammonia is used on manufacturing of AHM and during its reduction, ammonia is again released. In this work, we demonstrate production of MoO<sub>2</sub>/r-GO nano composite using two different methods to demonstrate scale up.

1. **Nanogram scale:** Reduction of GO deposited on Mo TEM grid
2. **Milligram scale:** Reduction of GO and Mo blue solution

Mo blue solution (Mo<sub>x</sub>O<sub>y</sub>.zH<sub>2</sub>O) was prepared by reducing MoO<sub>3</sub> solution (Molybdic acid) with Mo metal powder. The resulting Mo blue solution was mixed with GO. The reduction of GO/Molybdenum blue solution was achieved thermally at low temperature (650°), without using any toxic chemicals such as hydrazine and sodium borohydride, at high vacuum of 10<sup>-6</sup> torr. Similar result was also obtained for *in-situ* annealing of this mixture deposited on nickel TEM grid inside TEM.

## 8.2 Experimental methods

### 8.2.1 Nanogram scale: Reduction of GO deposited on Mo TEM grid:

GO (10mg/ml) synthesized by modified Hummers method was purchased from ACS nano and was diluted to 1mg/ml by adding de-ionized water. 2 µl of diluted GO (1mg/ml) was drop casted onto 300 mesh Mo TEM grid and dried in air, to form self-supporting, multilayered GO sample. *In situ* heating of sample was done using a Gatan tantalum-cup heating holder inside a Hitachi H9000NAR pressure TEM operating at an accelerating voltage of 300 kV, at a constant column pressure of 10<sup>-7</sup> Torr. Gatan Orius SC CCD was used for capturing high resolution images, bright

field images, dark field images and selected area electron diffraction(SAED) patterns. Heating was done at the rate of about 30°C per minute up to 837°C. SAED patterns were taken at multiple regions at different temperatures to understand the effect of rise in temperature on sample and evaluate the variation over different regions. Bright field, dark field and high resolution images were also captured from different regions of the samples, after they were annealed at 837°C for 20 mins, and then allowed to cool to room temperature. Measurement of size of crystallites for Nanogram scale were also done by direct measurement using tool in Gatan's digital micrograph software.

## 8.2.2 Milligram scale: Reduction of GO and Mo blue solution

### Molybdenum blue solution preparation:

200 mg of sparingly soluble  $\text{MoO}_3$  powder (Sigma Aldrich) was mixed with 200 ml of de-ionized water for a couple of days at room temperature and pressure. Clear solution (molybdic acid) was separated to another beaker and 100 gm of Mo metal powder ( $< 150 \mu\text{m}$  diameter) (Sigma Aldrich) was added to the molybdic acid at room temperature and pressure. Immediately, the solution turned blue and became deep blue in a couple of days. Finally, the solution (Mo blue) was also separated from Mo powder.

10ml of single layered GO (10mg/ml) purchased from ACS materials and 20 ml of Mo blue solution were mixed uniformly by sonicating the mixture for an hour. The mixture was poured into 3 cavities of silicone "Slide Duplicating Mold" each 1" x 3" x 3/32" (Electron Microscopy Sciences). After drying the mixture at room temperature and pressure, thin and dark GO/Mo blue paper was obtained. The paper like sample was transferred to Alumina coated tantalum boat

(3" x 3/4" x 3/8"). The boat was heated (Joule's heating) at pressure of  $10^{-6}$  torr, with constant rise of current of 1 amp/min from room temperature to 318°C (~ 10°C/min), held constant for 30 mins, then again constant rise in 1 am current, from 318°C to 430°C (~ 6°C/min), 430°C to 520°C (~ 5°C/min) and 520°C to 693°C (~ 4°C/min) in 165 min in total. The current flowing through the boat and potential difference across it were measured to calculate temperature of boat and it was correlated to temperature measured from a radiation pyrometer above 550°C. Residual gas analyzer(RGA) was used to analyze gas released during heating. At about 183°C, masses of 12, 17, 18, 44 were detected until the temperature reached 318°C. At 318°C, there was a sudden burst of 12, 17, 18, 28 and 44 masses. The pressure increased from  $3.6 \times 10^{-6}$  torr to  $8.4 \times 10^{-6}$  torr. At this point, the current and therefore temperature were kept constant (at 318°C) for half an hour, when the pressure returned to  $3.6 \times 10^{-6}$  torr, the current was again increased at constant rate. There was slight increase in pressure correlated of 12 and 44 masses after 348°C till 648°C.

After reaching 693°C in 165 minutes, the current was terminated and the sample was allowed to cool. For TEM measurement, the heated sample of less than 1mm diameter was crushed with a mortar and pestle, and so formed powder was dispersed in methanol. A drop of mixture with methanol was dropped on 300 mesh Ni grid with lacey carbon and dried in air. For XRD and XAS measurement, remaining heated sample was crushed into powder and filled into amorphous glass capillary tube of length 10 cm and internal diameter of 1 mm. X-ray powder diffraction measurement was carried out near Mo-K edge (19.95 keV) using Pilatus 100k Detector and X-ray absorption spectrum (XAS) including X-ray absorption near edge structure (XANES) and Extended X-ray absorption fine structure (EXAFS) were measured around Mo-K edge (20 keV)

at beamline 12BM, Advanced Photon Source (APS) at Argonne National lab Chicago, IL using ion chambers (nitrogen filled) detector. For comparison, standard MoO<sub>2</sub> (Sigma Aldrich) was spread on Kapton tape for XRD and XAS measurement. The small amount of crushed sample was also mixed with KBr to make pellet (2% concentration) for infrared measurement.

Conversion of two dimensional SAED and XRD pattern were reduced into one dimensional by using Nika software [85]. Crystallites size for all samples were calculated from width of the diffraction peak obtained from electron and powder XRD, using Scherrer equation  $T = \frac{K\lambda}{\beta \cos\theta}$ .

XAS data were processed by using Athena software and EXAFS data were fitted by Artemis software using theoretical standards from FEFF [86].

### 8.3 Results:

#### 8.3.1 Nanogram scale: Reduction of GO deposited on Mo TEM grid:

Annealing of GO deposited on Mo grid inside TEM, at above 550°C formed graphene monoxide (GMO), which is described in detail in [113]. IR spectrum is also not different from that of reduced GO described in [113]. Unlike GO and GMO, which are uniform and have similar contrast, granulated three dimensional nanocrystals like structures are also formed on GO and Mo grid interface during heating above 600°C. Diffraction pattern due to graphene (in GO) and GMO are uniform rings as they are multi-layered randomly oriented planes. But SAED taken from GO with these embedded three dimensional nanocrystals (fig 62 c) are non-uniform rings composed of diffraction spots. Intensity of these diffraction spots dominates over diffraction rings of graphene which had previously existed before heating. High resolution imaging acquired from these three dimensional nano-crystallites are also reported in fig (64). Size of the visible

embedded nanoparticles measured directly from bright field image from fig (62 a) ranges from 5-40 nm (50-130 Å).

### 8.3.2 Milligram scale: Reduction of GO and Mo blue solution

The heating of GO/Mo blue paper in alumina lined tantalum boat inside vacuum bell jar created a sample that was soft and highly electrostatic. The mass of sample was decreased from 200 mg to 50 mg after heating. TEM shows minute dark solid spheres like particles embedded inside GO film in bright field image (fig 65 a) and bright solid spheres like particles embedded in GO film in dark field image (fig 65 b). SAED done at the same part of the sample is shown in fig 65 c. Diffraction rings can be attributed to three dimensional nanocrystals formed during heating. Integrated line profile of SAED in fig 65 c is shown in fig 67. Integrated line profile of XRD is also shown in fig 67 and they are compared with XRD of standard MoO<sub>2</sub>. EXAFS of it is compared with EXAFS of standard MoO<sub>2</sub> in fig 68. Similarly, XANES comparison is done in fig 69. Infrared spectroscopy of the material after heating shows presence of C=C planer stretching at 1560 cm<sup>-1</sup> and epoxide group at 1200 cm<sup>-1</sup> (Fig 70). Average Size of crystallites calculated using Scherrer equation is 52Å.

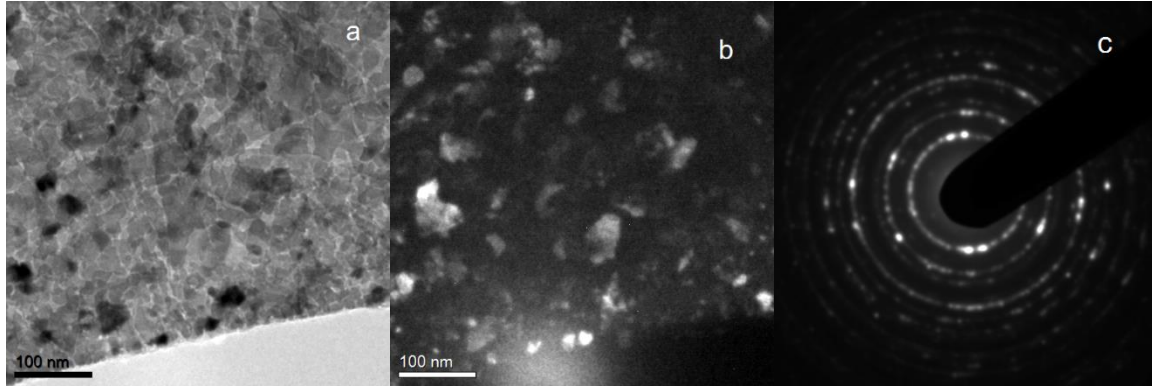


Figure 62: Nanogram scale: (a) Bright field image of GO with 3D nano-crystals embedded on it after heating it up to at 837 °C (b) dark field image from the same region (c) SAED pattern of GO, nearby Mo grid showing non-uniform diffraction rings formed due to polycrystalline 3D nanocrystals

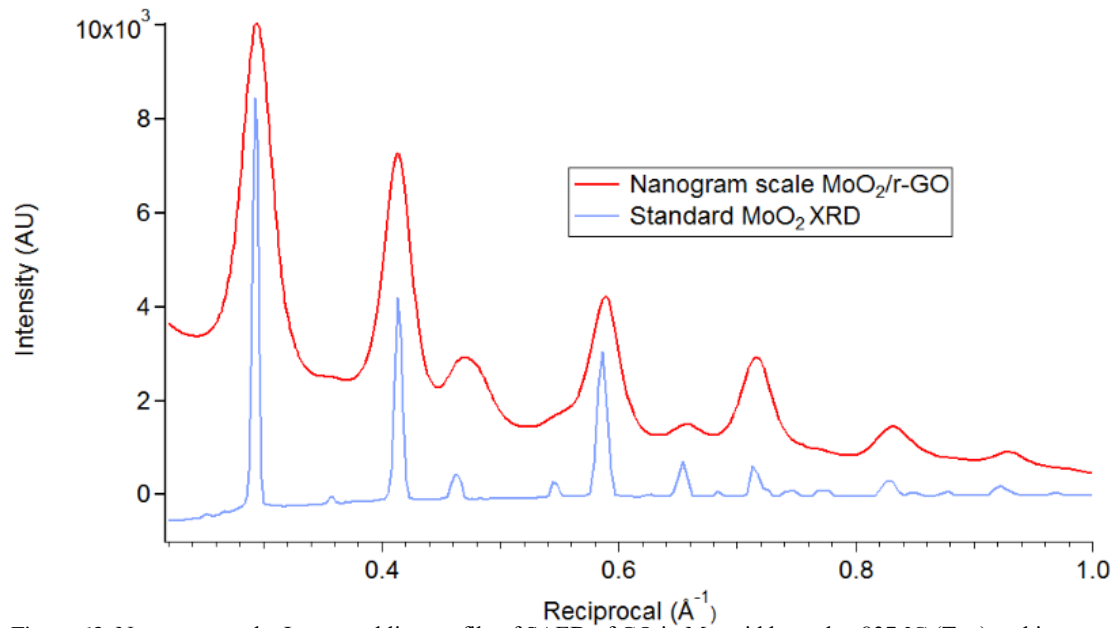


Figure 63: Nanogram scale: Integrated line profile of SAED of GO in Mo grid heated at 837 °C (Top) and integrated line profile of XRD of standard MoO<sub>2</sub> at room temperature (bottom)

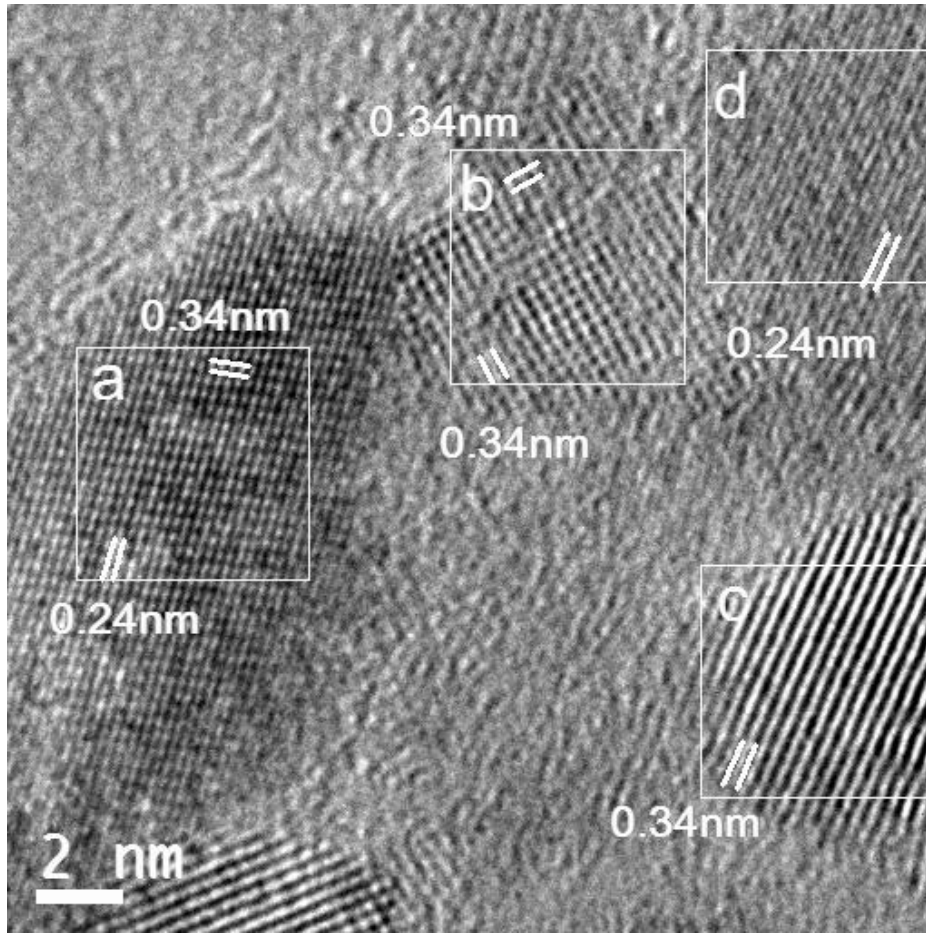


Figure 64: Nanogram scale: High resolution image of MoO<sub>2</sub>/r-GO nanocomposite showing crystallites of MoO<sub>2</sub> embedded inside reduced graphene oxide. 0.34 nm and 0.24 nm are the spacing consistent to the spacing of lattice planes of MoO<sub>2</sub>

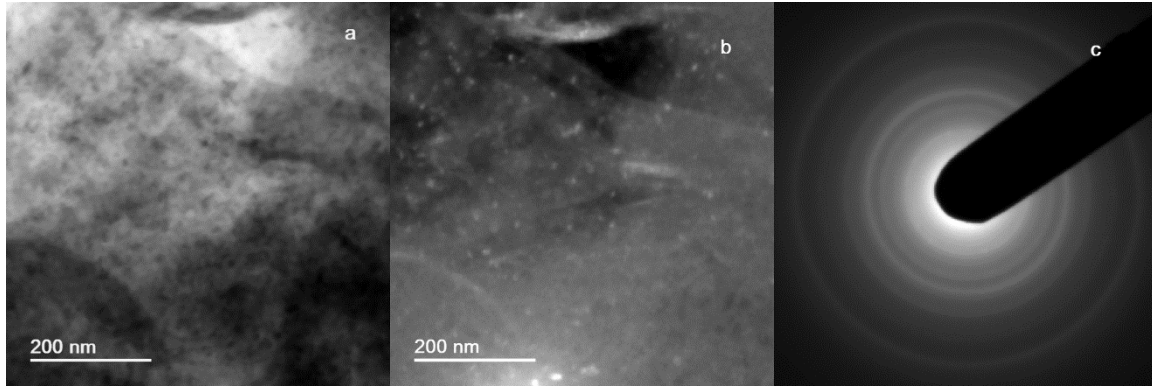


Figure 65: Milligram scale: (a), Bright field image of MoO<sub>2</sub>/r-GO composite transferred to Ni grid with lacy carbon showing dark spots due to formation of monoclinic MoO<sub>2</sub> on r-GO film lying over lacy carbon at region one. (b) Dark field image of the region one with bright spots of MoO<sub>2</sub>, and (c) SAED taken around the region one, displaying almost uniform diffraction rings having spacing due to MoO<sub>2</sub> crystals.

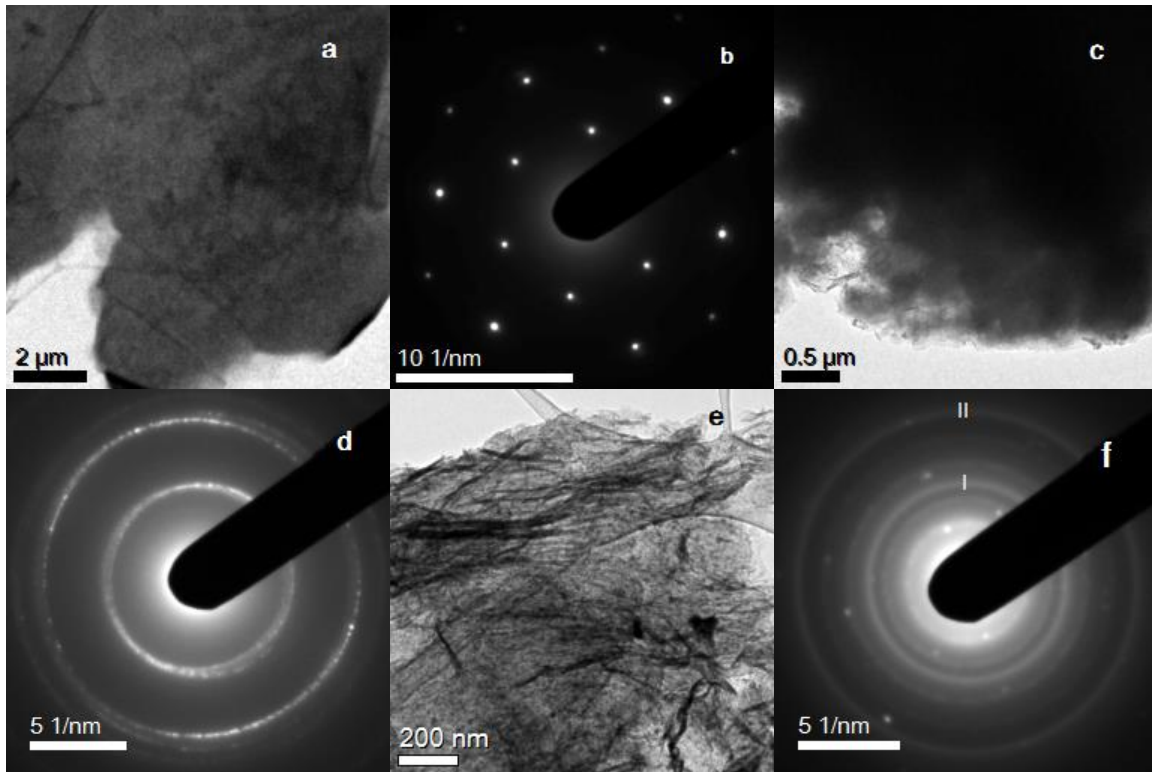


Figure 66: Milligram scale: (a) Bright field image of the sample at region two and (b) SAED at the region two showing the region is a single crystal of hexagonal graphene. (c) Bright field image at region three and (d) SAED at the region three shows the formation of graphene (e) At region four, homogeneous distribution of tiny MoO<sub>2</sub> crystallites in thin film of GO held on lacy Carbon of Ni TEM grid and (f) SAED from the region four showing diffraction due to graphene (Ring I and II) along with diffraction rings due to MoO<sub>2</sub>



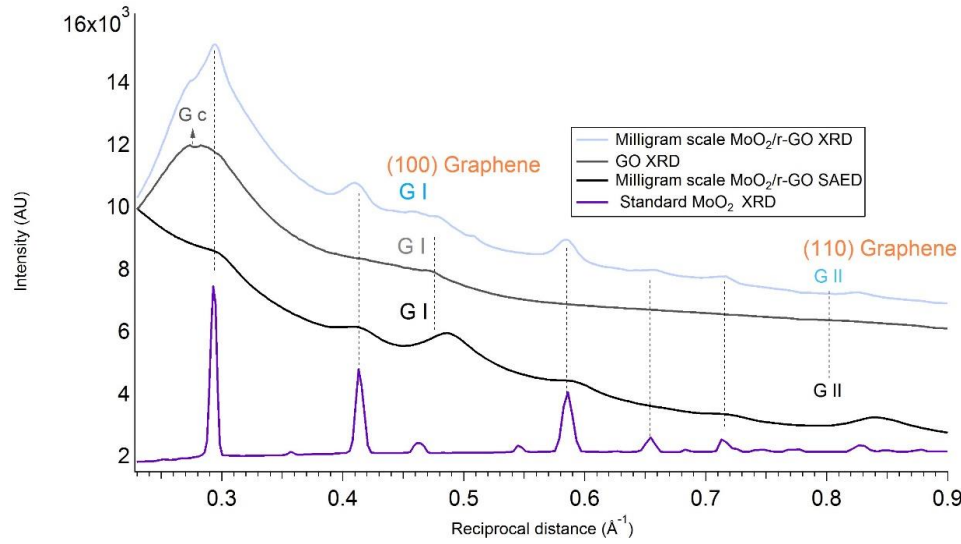


Figure 67: Milligram scale: Comparison of diffraction patterns of different forms of MoO<sub>2</sub>/r-GO nanocomposite with XRD of MoO<sub>2</sub> standard. From top: XRD of milligram scale MoO<sub>2</sub>/r-GO nanocomposite, XRD of GO before heating, SAED of milligram scale MoO<sub>2</sub>/r-GO nanocomposite, and XRD of Standard MoO<sub>2</sub>. Peak G<sub>c</sub> (3.65 Å) is due to diffraction from interplaner spacing between graphene sheets, G I and G II are diffraction from graphene planes with spacing of 2.13 Å (100) and 1.23 Å (110) respectively.

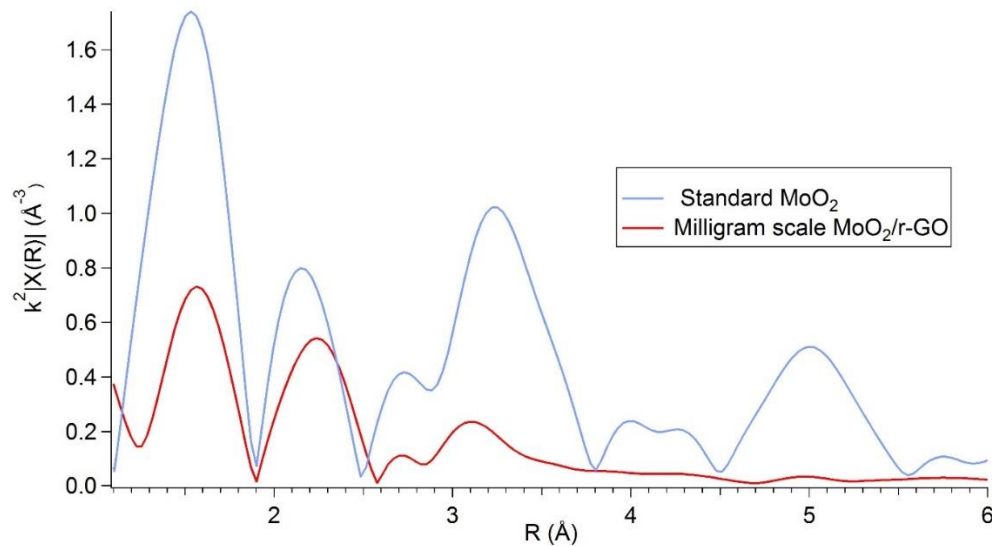


Figure 68: Milligram scale: Weighted Fourier transform of  $\chi(k)$  of Standard MoO<sub>2</sub> and milligram scale MoO<sub>2</sub>/r-GO nanocomposite showing similar peak in short range with small difference in position of peaks due to presence of GO in nanocomposite. Also there is absence of long range ordering in the nanocomposite. The first peak at 1.56 Å is due to scattering of photo electron wave by the 6 nearest neighbor oxygen in monoclinic MoO<sub>2</sub>, the second peak at 2.2 Å is mainly due to scattering of the wave from first Mo neighbor and the third peak at 2.7 Å is mainly due to the scattering of the wave from the second nearest Mo atom and the peak at 3.2 Å is due to 8 third nearest Mo atoms at 3.694 Å.

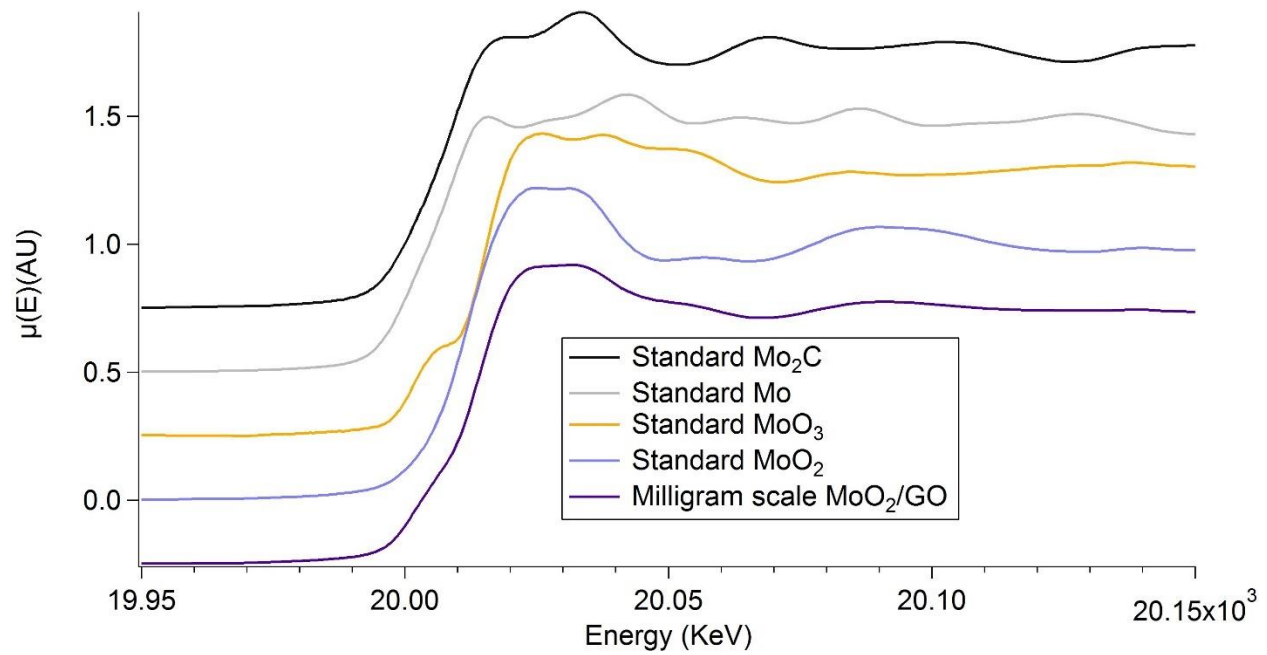


Figure 69: Milligram scale: Normalized XANES of milligram scale MoO<sub>2</sub> showing similar features to that of MoO<sub>2</sub> standard. Normalized absorption of Mo<sub>2</sub>C, Mo, MoO<sub>3</sub>, MoO<sub>2</sub> and Milligram scale MoO<sub>2</sub>/GO from top to bottom. The plots are stacked along vertical axis.

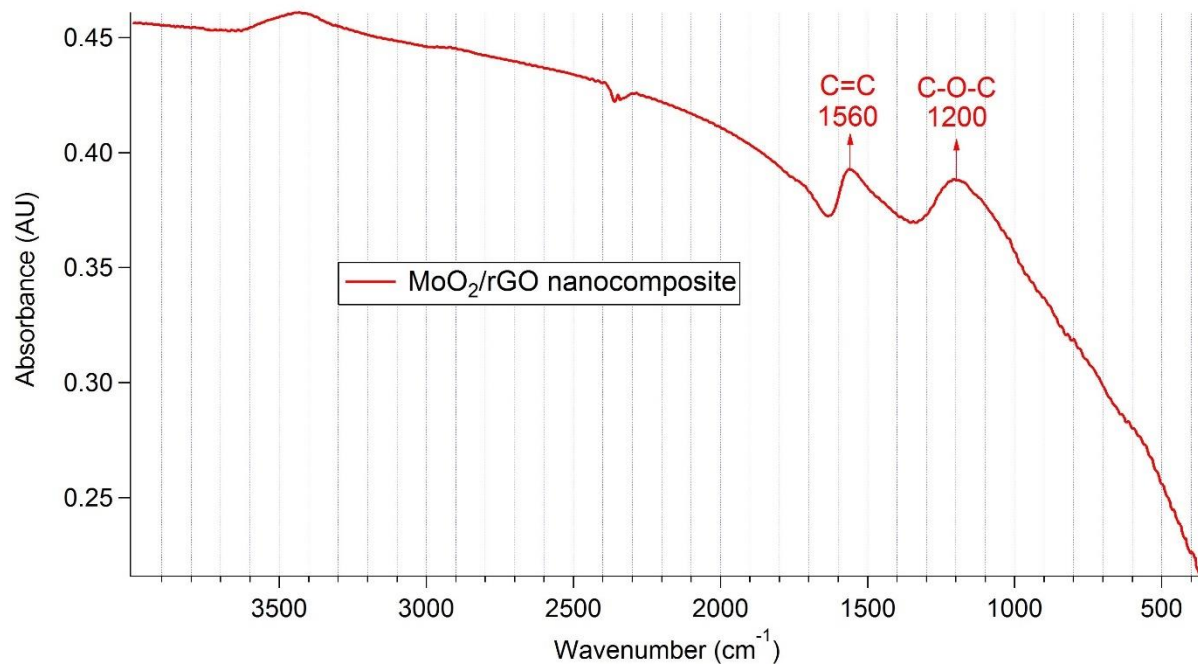


Figure 70: Milligram scale: Absorbance IR spectrum of ex-situ heated Mo blue/GO in vacuum showing presence of epoxide group (1200 cm<sup>-1</sup>) and carbon- carbon double bond stretching vibration (1560 cm<sup>-1</sup>).

## 8.4 Discussion:

### 8.4.1 Nanogram scale:

Granulated nano structures observed in bright and dark field images in fig 62 (a) and (b) and strong diffraction rings composed of large number of diffraction spots (fig 62 c) with disappearance of two dimensional diffraction rings (spacing 2.13 Å (100) and 1.23 Å (110)) due to graphene present in GO) hints toward so formed granulated structures are pure polycrystalline and composed of highly scattering heavy element compared to carbon and oxygen which forms GO and GMO. Integrated intensity profile of the SAED of the sample was compared with XRD of standard monoclinic-MoO<sub>2</sub> is shown in fig (64). Granulated particles formed on GO/Mo grid interface were confirmed to be monoclinic MoO<sub>2</sub>. Diffraction rings spacing 2.13 Å and 1.23 Å belonging to graphene were absent in fig (62 c) and (64) because graphene oxide has very small domain of graphene in it and Mo ions present in r-GO/MoO<sub>2</sub> nanocomposite are far stronger scatter of electron compared to graphene (carbon and oxygen) present in GO. Usually Mo metal is highly stable even at high temperature but in presence of air and water, it is oxidized. During *in-situ* heating, water trapped between layers of GO may have reacted with Mo metal of TEM grid. So Mo oxides are formed at the surface of Mo in grid and under reducing environment inside TEM, these oxides are reduced to crystalline monoclinic MoO<sub>2</sub> at temperature higher than 550°C. As temperature and duration of heating increases, more MoO<sub>2</sub> crystallites were formed due to unlimited supply of Mo from the grid and hence, sharper diffraction due to MoO<sub>2</sub> was observed.

#### 8.4.2 Milligram scale:

Comparison of integrated line profile of SAED and x-ray powder diffraction of the sample with X-ray powder diffraction of standard monoclinic  $\text{MoO}_2$  and pure graphene oxide (fig 67) confirms the formation of nanocrystalline composite of monoclinic  $\text{MoO}_2$  with GO. This evidence of formation of monoclinic  $\text{MoO}_2$  is also supported by EXAFS analysis shown in fig (68) and XANES analysis shown in fig (69). Diffraction rings due to graphene are invisible because domains of graphene present in the sample are small and Mo atoms present in the sample dominate the scattering of incident electron waves. However, IR spectrum of the sample in fig (70) shows the presence of C=C group ( $1560\text{ cm}^{-1}$ ) and epoxy group ( $1200\text{ cm}^{-1}$ ) and it is very much similar to IR of reduced GO as described in [113]. This means, though diffraction is mainly dominated only by monoclinic  $\text{MoO}_2$  crystals, chemical composition of the GO is modified to reduced GO. Mo blue has strong IR bands slightly different from  $\text{MoO}_3$  but so formed  $\text{MoO}_2$  after heating has very weak IR peaks and they are invisible in presence of IR bands of reduced GO.

During thermal annealing, TEM results have shown some variation in the formation of products. At multiple regions, a single crystal of graphene was also observed (fig 66 a and b). Some GO has reduced to graphite (fig 66 c and d) and in some regions diffraction of reduced GO has dominated over  $\text{MoO}_2$  crystallites (fig 66 e and f).

It is reported that GO is thermally unstable, and it starts losing mass (gas, water molecules) even at temperature below  $100^\circ\text{C}$ , the loss of mass peaks at  $200\text{-}230^\circ\text{C}$  and  $500\text{-}550^\circ\text{C}$  [114]. At  $226^\circ\text{C}$ , mass loss is mainly due to ejection of CO,  $\text{CO}_2$  and steam accompanied by the huge expansion [115], whereas at  $541^\circ\text{C}$  mass loss is due to pyrolysis of carbon skeleton of GO

takes place. Similar abrupt change in pressure were observed during annealing at 183°C and 318°C and RGA recorded the evolution steam (18), carbon dioxide (44) and carbon monoxide (28) gases.

Mo blue, an amorphous oxide ( $\text{Mo}_x\text{O}_y \cdot z\text{H}_2\text{O}$ ) was prepared by partial reduction of  $\text{MoO}_3$  (VI) by Mo metal. As Mo blue is soluble and GO is hydrophilic, Mo blue was uniformly distributed in GO. Later it was dried, and when heated abruptly at low pressure, its molecules must have further reduced into  $\text{MoO}_2$  (IV) molecules at around 550°C in presence of reducing agents such as carbon and carbon monoxide evolved during thermal annealing. So formed  $\text{MoO}_2$  molecules aggregated to form nano-crystallites of  $\text{MoO}_2$  which can be evidenced by XRD and SAED integrated line profile shown in fig 67. However, EXAFS analysis (fig 68) says the nano-crystallites of  $\text{MoO}_2$  have some defects as the position of peaks for them doesn't exactly matches with that for standard  $\text{MoO}_2$ , also the relative intensities of corresponding peaks don't match and there is no long range ordering for these nano-crystallites.

## 8.5 Conclusion:

We demonstrated a simple approach to synthesize monoclinic  $\text{MoO}_2$  and r-GO nanocomposite in nanogram scale as well as in milligram scale, was evidenced by SAED measurement performed on nanogram scale and SAED and XRD done on milligram scale. In nanogram scale the Mo grid was used as precursor for  $\text{MoO}_2$  and heating is done inside TEM. In milligram scale the nanocomposite was obtained through solution based method using Mo blue solution as precursor for  $\text{MoO}_2$ , followed by thermal annealing under similar conditions. Exactly similar results were obtained for heating a couple of micro-liters of mixture used for milligram scale in Ni TEM grid

inside TEM under similar condition. EXAFS done on milligram scale sample showed the local periodicity in MoO<sub>2</sub> is short ranged of distance only around 3.5 Å.

## **8.6 Acknowledgements**

We thank Dr. Sungsik Lee and Benjamin Reinhart for their assistance during the experiments conducted at 12-BM-B of the Advanced Photon Source. This work and the use of the Advanced Photon Source, a U.S. Department of Energy (DOE) Office of Science User Facility at Argonne National Laboratory, are supported by the U.S. DOE, Office of Science, Office of Basic Energy Science, Division of Chemical Sciences, Biosciences and Geosciences, under Contract No DE-AC02-06CH11357.

## Chapter 9 Concluding remarks

During my research, I have been involved in learning different theoretical and experimental techniques. I have always focused myself on making new material having some practical applications. During that process, I have learnt different characterization techniques and applied them to characterize materials. I have worked mainly on reduction of GO, and GMO. I have listed some of my work I have accomplished as a part of my dissertation in this section.

Making GMO inside TEM has been straightforward. It can be achieved by annealing GO in presence of Mo grid or soluble oxide of Mo oxide. Repeating similar result outside TEM for a larger quantity of GO under similar condition was hard to achieve. It was necessary to understand how GO behave with increase in temperature. Water molecules trapped between layers of GO, make it explode between 240-280°C and another burst in pressure occurs between 320-340°C due to reaction of carbon and oxygen present in GO. It took several attempts and several months to make GMO in milligram scale but this experience was helpful in making another useful material, nanocomposite of MoO<sub>2</sub> and r-GO.

When GMO was first prepared inside TEM and it was detected by its characteristic two dimensional diffraction rings spacing 2.6 Å and 1.52 Å, there were some doubt that those diffraction rings may be due to some unknown oxide or carbide of Molybdenum material. Once we made larger quantity of GMO, we were able to use XRD, XANES and EXAFS characterization techniques. These techniques have confirmed that GMO is different from any oxide or carbide of Mo. Another strong evidence for existence of GMO is the outcome of GO/CrO<sub>3</sub> experiment in which GMO is formed inside TEM by electron bombardment without

even using heat. The mechanism behind conversion of GO into GMO using different catalyst may be due to their high oxidizing power. Soluble oxides of Mo ( $\text{MoO}_3$  in solution or Mo blue solution) can be reduced at above  $500^\circ\text{C}$ . During reduction into  $\text{MoO}_2$ , they produce highly reactive atomic oxygen. This atomic oxygen has enough energy to break bond between carbon atom in the plane of GO and form double epoxy bridge between two carbon atoms. In case of  $\text{CrO}_3$ , energy is supplied by 300 keV electron beam which can enhance the catalytic reaction for the formation of GMO.

Combining the outcomes of XRD and SAED, I have modeled the structure of GMO in 3D. According to the model, GMO crystals are not in fully relaxed state because each GMO layers are constrained to remain in randomly oriented layers with same spacing to that of its precursor GO. Due to this fact, the diffraction pattern obtained for GMOs during each synthesis have variations in their lattice parameters.

Another product, nanocomposite of  $\text{MoO}_2/\text{r-GO}$  is also of great interest as this material is a good candidate for making energy storage device.  $\text{MoO}_2$  due to its distorted rutile structure has metallic conductivity and r-GO is very much similar to graphite, which has been used in cathode of LIBs. r-GO has larger interplaner spacing than graphite, so it can accommodate larger number of Li ions than graphite between its space. Also  $\text{MoO}_2$  has higher theoretical specific charge. In addition, these nano composite have larger surface area compared to the volume which make this nanocomposite a good candidate for making anode for LIBs. Currently my group is working on this project.



## References

- [1] C. Kittel, Introduction to Solid State Physics, John Wiley and Sons, Inc.
- [2] L. Wei, P. K. Kuo, R. L. Thomas, T. R. Anthony and W. F. Banholzer, "Thermal conductivity of isotopically modified single crystal diamond," *Phys. Rev. Lett*, vol. 70, p. 3764, 1993.
- [3] D. R. Cooper, B. D' Anjou, N. Ghattamaneni, B. Harack, M. Hilke, A. Horth, N. Majlis, M. Massicotte, L. Vandsbuerger, E. Whiteway and V. Yu, "Experimental Review of Graphene," *Condensed Matter Physics*, p. 56, 2012.
- [4] A. K. Geim and K. S. Novoselov, "The rise of graphene," *Nature Materials*, p. 183, 2007.
- [5] H. W. Kroto, J. R. Heath, S. C. O'Brien, R. F. Curl and R. E. Smalley, "C60: Buckminsterfullerene," *Nature*, pp. 162-163, 1981.
- [6] S. Iijima, "Helical microtubules of graphitic carbon," *Nature*, vol. 354, pp. 56-58, 1991.
- [7] P. R. Wallace, "The band theory of graphite," *Physical review*, vol. 71, no. 9, p. 662, 1947.
- [8] K. S. Novoselov, A. K. Geim, S. V. Morozov, D. Jiang, Y. Zhang, S. V. Dubonos, I. V. Grigorieva and A. A. Firsov, "Electric field effect in atomically thin carbon films," *Science*, vol. 306, p. 666, 2004.

- [9] K. S. Novoselov, D. Jiang, F. Schedin, T. J. Booth, V. V. Khotkevich, S. V. Morozov and A. K. Geim, "Two-dimensional atomic crystals," *PNAS*, vol. 102, no. 30, pp. 10451-10453, 2005.
- [10] K. S. Novoselov, A. K. Geim, S. V. Morozov, D. Jiang, M. I. Katsnelson, I. V. Grigorieva, S. V. Dubonos and A. A. Firsov, "Two-dimensional gas of massless Dirac fermions in graphene," *Nature*, pp. 197-200, 2005.
- [11] Graphene, Royal Swedish Academy of Sciences, 2010.
- [12] M. Acik and Y. J. Chabal, "A Review on Thermal Exfoliation of Graphene Oxide," *Journal of Materials Science Research*, pp. 101-112, 2013.
- [13] B. C. Brodie, "On the Atomic Weight of Graphite," *Philosophical transactions*, pp. 249-259, 1859.
- [14] W. S. Hummers and R. E. Offeman, "Preparation of Graphitic Oxide," *Journal of American Chemical Society*, vol. 80, no. 6, p. 1339, 1958.
- [15] S. Park, "Chemical methods for the production of graphenes," *nature nanotechnology*, pp. 217-224, 2009.
- [16] A. Buchsteiner, A. Lerf and J. Pieper, "Water Dynamics in Graphite Oxide Investigated with Neutron Scattering," *J. Phys. Chem*, vol. 110, no. 45, p. 22328–22338, 2006.
- [17] H. He, T. Riedl, A. Lerf and J. Klinowski, "Solid-State NMR Studies of the Structure of Graphite Oxide," *Journal of physical chemistry*, pp. 19954-19958, 1996.
- [18] H. He, J. Klinowski, M. Forster and A. Lerf, "A new structural model for graphite oxide," *Chemical Physics Letters*, vol. 287, pp. 53-56, 1998.

- [19] D. W. Lee, L. D. L. Santos V, J. W. Seo, L. L. Felix, A. D. Bustamante, J. M. Cole and C. H. W. Barnes, "The structure of graphite oxide: Investigation of its surface chemical groups," *Condensed matter material science*, pp. 1-6, 2010.
- [20] A. Lerf, H. He, M. Forster and J. Klinowski, "Structure of Graphite Oxide Revisited," *Journal of Physical Chemistry*, pp. 4477-4482, 1998.
- [21] D. R. Dreyer, S. Park, C. W. Bielawski and R. S. Ruoff, "The chemistry of graphene oxide," *Chemical Society Reviews*, pp. 228-240, 2009.
- [22] S. Stankovich, D. A. Dikin, R. D. Piner, K. A. Kohlhaas, A. Kleinhammes, Y. Jia, Y. Wu, S. T. Nguyen and R. S. Ruoff, "Synthesis of graphene-based nanosheets via chemical reduction of exfoliated graphite oxide," *Carbon*, pp. 1558-1565, 2007.
- [23] D. Li, M. B. Muller, S. Gilje, R. B. Kaner and G. G. Wallace, "Processable aqueous dispersions of graphene nanosheets," *Nature nanotechnology*, pp. 101-105, 2008.
- [24] H.-J. Shin, K. K. Kim, A. Benayad, S.-M. Yoon, H. K. Park, I.-S. Jung, M. H. Jin, H.-K. Jeong, J. M. Kim, J.-Y. Choi and Y. H. Lee, "Efficient Reduction of Graphite Oxide by Sodium Borohydride and Its Effect on Electrical Conductance," *Advanced Functional Materials*, pp. 1987-1992, 2009.
- [25] S. SashaStankovich, R. D. Piner, X. Chen, N. Wu, S. T. Nguyen and R. S. Ruoff, "Stable aqueous dispersions of graphitic nanoplatelets via the reduction of exfoliated graphite oxide in the presence of poly(sodium 4-styrenesulfonate)," *Journal of Materials Chemistry*, pp. 155-158, 2005.

- [26] Y. You, V. Sahajwalla, M. Yoshimura and R. K. Joshi, "Graphene and graphene oxide for desalination," *Nanoscale*, vol. 8, p. 117–119, 2016.
- [27] E. C. Mattson, H. Pu, S. Cui, M. A. Schofield, S. Rhim, M. J. Nasse, R. S. Ruoff, G. Lu, M. Weinert, M. Gajdardziska-Josifovska, J. Chen and C. J. Hirschmugl.
- [28] H. H. Pu, S. H. Rhim, C. J. Hirschmugl, M. Gajdardziska-Josifovska, M. Weinert and J. H. Chen, "Strain-induced band-gap engineering of graphene monoxide and its effect on graphene," *Physical review B*, vol. 87, p. 085417, 2013.
- [29] J. Woo, K.-H. Yun, S. B. Cho and Y.-C. Chung, "Defect-induced semiconductor to metal transition in graphene monoxide," *Phys. Chem. Chem. Phys.*, vol. 16, pp. 13477-13482, 2014.
- [30] J. J. Sardroodi, A. Jalalinia and A. R. Ebrahimzadeh, "Engineering of the electronic structure of graphene monoxide by out of plane and in-plane strains investigated by DFT," *Computational and Theoretical Chemistry*, vol. 1090, pp. 34-40, 2016.
- [31] J. Woo, K.-H. Yun and Y.-C. Chung, "Graphene monoxide bilayer as a high performance on/off switching media for nanoelectronics," *ACS Applied Materials & Interfaces*, 2016.
- [32] H. S. H.S. HUANG and K. S. HWANG, "Deoxidation of Molybdenum during Vacuum Sintering," *METALLURGICAL AND MATERIALS TRANSACTIONS A*, vol. 33A, pp. 657-664, 2002.
- [33] K. L., "Least squares refinement of the crystal structure of molybdenum trioxide," *Arkiv för Kemi*, vol. 21, pp. 357-364, 1963.

- [34] C. A. Ellefson, O. Marin-Flores, S. Ha and M. G. Norton, "Synthesis and applications of molybdenum (IV) oxide," *J Mater Sci*, vol. 47, p. 2057–2071, 2012.
- [35] L. Zhuang, Q. Li and S. Chen, "In-situ preparation of porous carbon-supported molybdenum dioxide and its performance in the oxidative desulfurization of thiophene," *J Mater Sci*, vol. 49, p. 5606–5616, 2014.
- [36] S. Chaudhury, S. K. Mukerjee, V. N. Vaidya and V. Venugopal, Kinetics and mechanism of carbothermic reduction of MoO<sub>3</sub> to MoO<sub>2</sub>, vol. 261, Mumbai: Elsevier, 1997, pp. 105-113.
- [37] A. J. Hegedus and J. Neugebauer, *Z. Anorg. Chem*, vol. 305, p. 216, 1960.
- [38] X. Xie, L. Lin, R.-Y. Liu, Y.-F. Jiang, Q. Zhu and A.-W. Xu, "The synergistic effect of metallic molybdenum dioxide nanoparticle decorated graphene as an active electrocatalyst for an enhanced hydrogen evolution reaction," *Journal of Materials Chemistry A*, vol. 3, p. 8055–8061, 2015.
- [39] A. Katrib, J. W. Sobczak, M. Krawczyk, L. Zommer, A. Benadda, A. Jablonski and G. Maire, "Surface studies and catalytic properties of the bifunctional bulk MoO<sub>2</sub> system," *SURFACE AND INTERFACE ANALYSIS*, vol. 34, p. 225–229, 2002.
- [40] A. Katrib, P. Leflaive, L. Hilaire and G. Maire, "Molybdenum based catalysts. I. MoO<sub>2</sub> as the active species in the reforming of hydrocarbons," *Catalysis Letters*, vol. 38, pp. 95-99, 1996.
- [41] P. Roy and S. K. Srivastava, "Nanostructured anode materials for lithium ion batteries," *Journal of Materials Chemistry A*, vol. 3, pp. 2454-2484, 2015.

- [42] H. C. Choi, Y. M. Jung, I. Noda and S. B. Kim, "A Study of the Mechanism of the Electrochemical Reaction of Lithium with CoO by Two-Dimensional Soft X-ray Absorption Spectroscopy (2D XAS), 2D Raman, and 2D Heterospectral XAS-Raman Correlation Analysis," *J. Phys. Chem. B*, vol. 107, pp. 5806-5811, 2003.
- [43] G. G. Amatucci, J. M. Tarascon and L. C. Klein, "CoO<sub>2</sub>, The End Member of the LiCoO<sub>2</sub> Solid Solution," *Journal of Electrochemical Society*, vol. 143, pp. 1114-1123, 1996.
- [44] D. Aurbach, Y. Talyosef, B. Markovsky, E. Markevich, E. Zinigrad, L. Asraf, J. S. Gnanaraja and H.-J. Kim, "Design of electrolyte solutions for Li and Li-ion batteries: a review," *Electrochimica acta*, pp. 1-8, 2004.
- [45] A. Bhaskar, M. Deepa and T. N. Rao, "MoO<sub>2</sub>/Multiwalled Carbon Nanotubes (MWCNT) Hybrid for Use as a Li-Ion battery Anode," *ACS Applied Materials and Interfaces*, vol. 5, pp. 2555-2566, 2013.
- [46] J. Cabana, L. Monconduit, D. Larcher and M. R. Palacín, "Beyond Intercalation-Based Li-Ion Batteries: The State of the Art and Challenges of Electrode Materials Reacting Through Conversion Reactions," *Advanced Energy Materials*, vol. 22, pp. E170-E192, 2010.
- [47] G. Liu, S. Xun, N. Vukmirovic, X. Song, P. Olalde-Velasco, H. Zheng, V. S. Battaglia, L. Wang and W. Yang, "Polymers with Tailored Electronic Structure for High Capacity Lithium Battery Electrodes," *Advanced Materials*, vol. 23, pp. 4679-4683, 2011.
- [48] Y. Liu, H. Zhang, P. Ouyang and Z. Li, "One-pot hydrothermal synthesized MoO<sub>2</sub> with high reversible capacity for anode application in lithium ion battery," *Electrochimica Acta*, vol. 102, p. 429– 435, 2013 .

- [49] L. Zhou, H. B. Wu, Z. Wang and X. W. (. Lou, "Interconnected MoO<sub>2</sub> Nanocrystals with Carbon Nanocoating as High-Capacity Anode Materials for Lithium-ion Batteries," *ACS applied material and interfaces*, vol. 3, pp. 4853-4857, 2011.
- [50] J. Ilavsky, "Nika - software for 2D data reduction," *J. Appl. Cryst*, vol. 45, pp. 324-328, 2012.
- [51] D. B. Williams and C. B. Carter, *Transmission Electron Microscopy A Textbook for Materials Science*, Springer, 2009.
- [52] L. Reimer and H. Kohl, *Transmission Electron Microscopy*, Germany: Springer series, 2008.
- [53] K. Nakamoto, *Infrared and Raman Spectra of Inorganic and Coordination compounds*, Milwaukee: A Wiley-Interscience Publication, 1986.
- [54] P. R. Griffiths and J. A. de Haseth, *Fourier Transform Infrared Spectrometry*, Hoboken, New Jersey: John Wiley & Sons, 2007.
- [55] J. Als-Nielsen and D. McMorrow, *Modern X-rays Physics*, Denmark: John Wiley & Sons, Ltd, 2001.
- [56] R. Shankar, *Principles of Quantum Mechanics*, Newyork and London: Plenum Press, 1994.
- [57] J. J. Sakurai, *Modern Quantum Mechanics*, Addison-Wesley Publishing Company, Inc, 1994.
- [58] R. S. Bare, *X-ray absorption spectroscopy*, Des Plaines: UOP LLC, a Honeywell Company, 2006.

- [59] J. D. Jackson, *Classical Electrodynamics*, John Wiley & Sons, Inc., 1998.
- [60] T. Owen, *Fundamentals of UV-visible spectroscopy*, Germany: Hewlett-Packard Company, 1996.
- [61] S. Stankovich, D. A. Dikin, R. D. Piner, K. A. Kohlhaas, A. Kleinhammes, Y. Jia, Y. Wu, S. T. Nguyen and R. S. Ruoff, "Synthesis of graphene-based nanosheets via chemical reduction of exfoliated graphite oxide," *Carbon*, vol. 45 , p. 1558–1565, 2007.
- [62] N. A. Dhas and A. Gedanken, "Characterization of Sonochemically Prepared Unsupported and Silica-Supported Nanostructured Pentavalent Molybdenum Oxide," *J. Phys. Chem. B*, vol. 101, pp. 9495-9503, 1997.
- [63] T. D. Tullius, W. O. Gillum, R. M. Carlson and K. O. Hodgson, "Structural study of the Vanadium complex in living Ascidian Blood Cells by X-ray Absorption spectroscopy," *J. Am. Chem. Soc*, vol. 102, pp. 5670-5676, 1980.
- [64] S. P. Cramer and K. O. Hodgson, "X-ray Absorption Spectroscopy: a New Structural Method and Its Application to Bioinorganic Chemistry," *Progress in Inorganic Chemistry*, vol. 25, pp. 1-33, 1979.
- [65] T. Ressler, J. Wienold, R. E. Jentoft and T. Neisius, "Bulk Structural Investigation of the Reduction of MoO<sub>3</sub> with Propene," *Journal of Catalysis*, vol. 210, p. 67–83 , 2002.
- [66] J. Song, X. Wang and C.-T. Chang, *Journal of Nanomaterials*, vol. 2014, p. 6, 11 March 2014.
- [67] Y. Sun, X. Hu, W. Luo and Y. Huang, *American Chemical Society*, vol. 5, no. 9, pp. 7100-7107, 2011.



- [68] G. C. Loh and D. Baillargeat, *Journal of applied physics*, vol. 114, p. 033534, 2013.
- [69] H. Marsh and A. P. Warburton, *Journal of applied chemistry*, vol. 20, no. 4, pp. 133-142, 1970.
- [70] I. Mochida, E. Nakamura, K. Maeda and T. Kenjiro, *Carbon*, vol. 14, no. 6, pp. 341-344, 1976.
- [71] J. Gillot, B. Lux, P. Cornuautt and F. d. Chaffaut, *J. chem Phys*, no. Special Issue, p. 172, (Apr. 1969).
- [72] W. D. Hewett, Hr, J. H. Newton and W. W. Weltner, Jr, "Absorption spectra of Molybdenum Oxide molecules and Molybdenum atoms in Neon and Argon matrices at 4K," *The Journal of Physical Chemistry*, vol. 79, no. 24, pp. 2640-2649, 1975.
- [73] K. S. Novoselov, A. . K. Geim, S. V. Morozov, D. Jiang, Y. Zhang, S. V. Dubonos, I. V. Grigorieva and A. A. Firsov, "Electric Field Effect in Atomically Thin Carbon Films," *Science*, vol. 306, pp. 666-669, 2004.
- [74] K. S. Novoselov, D. Jiang, F. Schedin, T. J. Booth, V. V. Khotkevich, S. V. Morozov and A. K. Geim, "Two-dimensional atomic crystals," *PNAS*, p. 10451–10453, 2005.
- [75] A. K. Geim and K. .. NOVOSELOV, "The rise of graphene," *Nature materials*, vol. 6, pp. 183-191, 2007.
- [76] A. K. Geim, "Graphene: Status and Prospects," *SCIENCE*, vol. 324, pp. 1530-1534, 2009.
- [77] M. J. Allen, V. C. Tung and R. B. Kaner, "Honeycomb Carbon: A Review of Graphene," *Chem. Rev*, vol. 110, p. 132–145, 2010.

- [78] K. S. Novoselov, V. I. Fal'ko, L. Colombo, P. R. Gellert, M. G. Schwab and K. Kim, "A roadmap for graphene," *Nature*, vol. 490, pp. 192-200, 2012.
- [79] J. Woo, K.-H. Yun, S. B. Cho and Y.-C. Chung, "Defect-induced semiconductor to metal transition in graphene monoxide," *Phys.Chem.Chem.Phys.*, vol. 16, p. 13477, 2014.
- [80] D. R. Dreyer, S. Park, C. W. Bielawski and R. S. Ruoff, "The chemistry of graphene oxide," *Chemical Society Reviews*, vol. 39, p. 228–240, 2010.
- [81] R. J. Young and I. A. Kinloch, "Graphene and graphene-based nanocomposites, NanoScience Vol 1," The Royal Society of Chemistry, Manchester, 2013.
- [82] E. C. Mattson, H. Pu, S. Cui, M. A. Schofield, S. Rhim, G. Lu, M. J. Nasse, R. S. Ruoff, M. Weinert, M. Gajdardziska-Josifovska, J. Chen and C. J. Hirschmugl, "Evidence of Nanocrystalline Semiconducting Graphene Monoxide during Thermal Reduction of Graphene Oxide in Vacuum," *ACS Nano*, pp. 9710-9717, 2011.
- [83] H. H. Pu, S. H. Rhim, C. J. Hirschmugl, M. Gajdardziska-Josifovska, M. Weinert and J. Chen, "Strain-induced band-gap engineering of graphene monoxide and its effect on graphene," *Physical Review B*, p. 085417, 2013.
- [84] J. Woo, K.-H. Yun and Y.-C. Chung, "Graphene monoxide bilayer as a high performance on/off switching media for nanoelectronics," *ACS Applied Materials and Interfaces*, 2016.
- [85] J. Ilavsky, "Nika-software for 2D data reduction," *J. Appl. Cryst.*, vol. 45, pp. 324-328, 2012.
- [86] B. Ravel, "Athena, Artemis, Hephaestus: data analysis for x-ray absorption spectroscopy using IFEFFIT," *J. Synchrotron Radiat*, vol. 12, pp. 537-541, 2005.

- [87] J. A. Wharton, D. H. Ross, G. M. Treacy, G. D. Wilcox and K. R. Baldwin, "An EXAFS investigation of molybdate-based conversion coatings," *Journal of applied electrochemistry*, pp. 553-561, 2003.
- [88] T. Ressler, J. Wienold, R. E. Jentoft and T. Neisius, "Bulk Structural Investigation of the Reduction of MoO<sub>3</sub> with Propene and the Oxidation of MoO<sub>2</sub> with Oxygen," *Journal of Catalysis*, vol. 210, pp. 67-83, 2002.
- [89] M. Yi and Z. Shen, "A review on mechanical exfoliation for the scalable production of graphene," *J. Mater. Chem. A*, vol. 3, p. 11700–11715, 2015.
- [90] Y. Huang, E. Sutter, N. N. Shi, J. Zheng, T. Yang, D. Englund and H.-J. Gao, "Reliable Exfoliation of Large-Area High-Quality Flakes of Graphene and Other Two-Dimensional Materials," *ACS nano*, vol. 9, no. 11, p. 10612–10620, 2015.
- [91] K. S. Kim, Y. Zhao, S. Y. Lee, J. M. Kim, K. S. Kim, J.-H. Ahn, P. Kim, J.-Y. Choi and B. H. Hong, "Large-scale pattern growth of graphene films for stretchable transparent electrodes," *Nature*, vol. 457, pp. 706-710, 2009.
- [92] A. J. Strudwick, N. E. Weber, M. G. Schwab, M. Kettner, R. T. Weitz, J. R. Wunsch, K. Müller and H. Sachdev, "Chemical Vapor Deposition of High Quality Graphene Films from Carbon Dioxide Atmospheres," *ACS nano*, vol. 9, no. 1, pp. 31-42, 2015.
- [93] Y. ZHANG, L. ZHANG and C. ZHOU, "Review of Chemical Vapor Deposition of Graphene and Related Applications," *ACCOUNTS OF CHEMICAL RESEARCH*, vol. 46, no. 10, p. 2329–2339, 2013.

- [94] X. Chen, L. Zhang and S. Chen, "Large area CVD growth of graphene," *Synthetic Metals*, vol. 210, pp. 95-108, 2015.
- [95] T. Ohta, A. Bostwick, T. Seyller, K. Horn and E. Rotenberg, "Controlling the Electronic Structure of Bilayer Graphene," *SCIENCE*, vol. 313, pp. 951-954, 2006.
- [96] C. Berger, Z. Song, X. Li, X. Wu, N. Brown, C. c. Naud, D. Mayou, T. Li, J. Hass, A. N. Marchenkov, E. H. Conrad, P. N. First and W. A. de Heer, "Electronic Confinement and Coherence in Patterned Epitaxial Graphene," *SCIENCE*, vol. 312, pp. 1191-1196, 2006.
- [97] P. W. SUTTER, J.-I. FLEGE and E. A. SUTTER, "Epitaxial graphene on ruthenium," *Nature*, vol. 7, pp. 406-410, 2008.
- [98] Phan, D.-T. Phan and G.-S. Chung, "Effects of Oxygen-Functional Groups on Humidity Sensor Based Graphene Oxide Thin Films," *Sensors, 2012 IEEE*, pp. 1-4, 2012.
- [99] S. Pei and H.-M. Cheng, "The reduction of graphene oxide," *Carbon*, pp. 3210-3228, 2012.
- [100] R. Tokarz-Sobieraj, R. Grybo's and M. Witko, "Electronic structure of MoO<sub>2</sub>. DFT periodic and cluster model studies," *Applied Catalysis A: General*, vol. 391, pp. 137-143, 2010.
- [101] Y. Shi, B. Guo, S. A. Corr, Q. Shi, Y.-S. Hu, K. R. Heier, L. Chen, R. Seshadri and G. D. Stucky, "Ordered Mesoporous Metallic MoO<sub>2</sub> Materials with Highly Reversible Lithium Storage Capacity," *Nano Letters*, 2009.

- [102] Y. Liu, H. Zhang, P. Ouyang and Z. Li, "One-pot hydrothermal synthesized MoO<sub>2</sub> with high reversible capacity for anode application in lithium ion battery," *Electrochimica Acta*, pp. 429-435, 2013.
- [103] Cabana, J. Cabana, L. Monconduit, D. Larcher and M. R. Palacin, "Beyond intercalation-based Li-ion batteries: The state of the art and challenges of electrode materials reacting through conversion reactions," *Advanced energy materials*, pp. E170-E192, 2010.
- [104] J. Ni, Y. Zhao, L. Li and L. Mai, "Ultrathin MoO<sub>2</sub> nanosheets for superior lithium storage," *Nano energy*, pp. 129-135, 2015.
- [105] P. Han, W. Ma, S. Pang, Q. Kong, J. Yao, C. Bi and G. Cui, "Graphene decorated with molybdenum dioxide nanoparticles for use in high energy lithium ion capacitors with an organic electrolyte," *Journal of Materials chemistry A*, pp. 5949-5954, 2013.
- [106] X. Xie, L. Lin, R.-Y. Liu, Y.-F. Jiang, Q. Zhu and A.-W. Xu, "The synergistic effect of metallic molybdenum dioxide nanoparticle decorated graphene as an active electrocatalyst for an enhanced hydrogen evolution reaction," *Journal materials Chemistry A*, pp. 8055-8061, 2015.
- [107] Q. Liu, C. Sun, Q. He, D. Liu, A. Khalil, T. Xiang, Z. Wu, J. Wang and L. Song, "Ultrathin carbon layer coated MoO<sub>2</sub> nanoparticles for high-performance near-infrared photothermal cancer therapy," *Royal society of chemistry*, pp. 10054-10057, 2015.
- [108] C. A. Ellefson, O. Marin-Flores, S. Ha and M. G. Norton, Synthesis and applications of molybdenum (IV) oxide, *Journal of material science*, 2012.

- [109] Marin-F, O. Iores, T. Turba, C. Ellefson, K. Wang, J. Breit, J. Ahn, M. G. Norton and S. Ha, "Nanoparticle molybdenum dioxide: A highly active catalyst for partial oxidation of aviation fuels," pp. 186-192, 2010.
- [110] L. Zhuang, Q. Li and S. Chen, In-situ preparation of porous carbon-supported molybdenum dioxide and its performance in the oxidative desulfurization of thiophene, *Journal of Material Science*, 2014.
- [111] Z. Wang, J. S. Chen, T. Zhu, S. Madhavi and X. W. Lou, "On-pot synthesis of uniform carbon-coated MoO<sub>2</sub> nanospheres for high-rate reversible lithium storage," *The Royal society of chemistry*, pp. 6906-6908, 2010.
- [112] K. H. Seng, G. D. Du, Z. X. Chen, H. K. Liu and Z. P. Guo, "Facile synthesis of graphene-molybdenum dioxide and its lithium storage properties," *Journal of materials chemistry*, pp. 16072-16077, 2012.
- [113] E. C. Mattson, H. Pu, S. Cui, M. A. Schofield, S. Rhim, G. Lu, M. J. Nasse, R. S. Ruoff, M. Weinert, M. Gajdardziska-Josifovska, J. Chen and C. J. Hirschmugl, "Evidence of Nanocrystalline Semiconducting Graphene Monoxide during Thermal Reduction of Graphene Oxide in Vacuum," *American Chemical Society*, p. 9710-9717, 2011.
- [114] H. Yang, C. Shan, F. Li, D. Han, Q. Zhang and L. Niu, "Covalent functionalization of polydisperse chemically-converted graphene sheets with amine-terminated ionic liquid," *RSC/Chem. Commun*, p. 3880-3882, 2009.
- [115] S. Stankovich, D. A. Dikin, R. D. Piner, K. A. Kohlhaas, A. Kleinhammes, Y. Jia, Y. Wu, S. T. Nguyen and R. S. Ruoff, "Synthesis of graphene-based nanosheets via chemical reduction of exfoliated graphite oxide," *Carbon*, vol. 45, pp. 1558-1565, 2007.

[118] S. R. Bare, "X-ray Absorption Spectroscopy," Des Plaines, IL 60026 USA, 2006.

[119] "Graphene," in *Scientific Background on the Nobel Prize in Physics 2010*, Stockholm, Royal Swedish Academy of Sciences, 2010, pp. 1-10.

## CURRICULUM VITAE

Binod Manandhar

**Tribhuvan University (TU)** Kathmandu, Nepal 2002-2004

Masters of Science, Physics

**Amrit Science Campus (TU)** Kathmandu, Nepal 1999-2002

Bachelor of Science (Physics, Chemistry, Mathematics)

**Dissertation title:** Synthesis and analysis of carbon-transition metal oxide composites

### Publication:

E C Mattson, M Unger, B Manandhar, Z Alavi, C J Hirschmugl” Multi-beam Synchrotron FPA Chemical Imaging: Impact of Schwarzschild Objective on Spatial Resolution,” Journal of Physics, Conference Series. (2013), 425:142001 DOI 10.1088/1742-6596/425/14/142001

### Teaching Experience:

- Physics 214 (Lab Physics I (Calculus treatment))
- **Physics 123 (General Physics Laboratory II (Non-Calculus Treatment))**
- **Physics 108 (Laboratory for Physics in Everyday life)**

### Awards:

Chancellor’s Graduate Student Award (10x) 2010-2016

UWM Scholarship (7x) 2010-2015

David Lichtman Memorial Scholarship 2012(Spring)

Physics Research Excellence award 2015(Fall)